Journal of International Modern Engineering
ISSN: 1930-6628
www.ijme.us

INTERNATIONAL JOURNAL OF MODERN ENGINEERING

Spring / Summer 2012
Volume 12, Number 2

The Leading Journal of Engineering, Applied Science and Technology

Industrial Electronics

Biomedical Civil Aerospace

Computer

Electrical

Chemical

Mechanical

ENGINEERING

THE LEADING JOURNAL OF ENGINEERING, APPLIED SCIENCE, AND TECHNOLOGY

www.ijme.us

www.iajc.org

INTERNATIONAL JOURNAL OF MODERN ENGINEERING

ABOUT IJME:

- IJME was established in 2000, and it is the first and official flagship journal of the International Association of Journal and Conferences (IAJC).
- IJME is a high-quality, independent journal steered by a distinguished board of directors and supported by an international review board representing many well-known universities, colleges, and corporations in the U.S. and abroad.
- IJME generally publishes research related to all areas of engineering, applied science, and related technology.

OTHER IAJC JOURNALS:

- The International Journal of Engineering Research and Innovation (IJERI)
  For more information visit www.ijeri.org
- The Technology Interface International Journal (TIIJ).
  For more information visit www.tiij.org

IJME SUBMISSIONS:

- Manuscripts should be sent electronically to the manuscript editor, Dr. Philip Weinsier, at philipw@bgsu.edu.

  For submission guidelines visit www.ijme.us/submissions

TO JOIN THE REVIEW BOARD:

- Contact the chair of the International Review Board, Dr. Philip Weinsier, at philipw@bgsu.edu.

  For more information visit www.ijme.us/ijme_editorial.htm

www.tiij.org

www.ijeri.org

Contact us:

Mark Rajai, Ph.D.

Editor-in-Chief
California State University-Northridge
College of Engineering and Computer Science
Room: JD 4510
Northridge, CA 91330
Office: (818) 677-5003
Email: mrajai@csun.edu

INTERNATIONAL JOURNAL OF MODERN ENGINEERING

The INTERNATIONAL JOURNAL OF MODERN ENGINEERING (IJME) is an independent, not-for-profit publication, which aims to provide the engineering community with a resource and forum for scholarly expression and reflection.

IJME is published twice annually (Fall and Spring issues) and includes peer-reviewed articles, book and software reviews, editorials, and commentary that contribute to our understanding of the issues, problems, and research associated with engineering and related fields. The journal encourages the submission of manuscripts from private, public, and academic sectors. The views expressed are those of the authors and do not necessarily reflect the opinions of IJME or its editors.

EDITORIAL OFFICE:

Mark Rajai, Ph.D.
Editor-in-Chief
Office: (818) 677-2167
Email: ijmeeditor@iajc.org
Dept. of Manufacturing Systems Engineering & Management
California State University-Northridge
18111Nordhoff Street
Northridge, CA 91330-8332

THE INTERNATIONAL JOURNAL OF MODERN ENGINEERING EDITORS

Editor-in-Chief:

Mark Rajai
California State University-Northridge

Associate Editors:

Alok Verma
Old Dominion University

Li Tan
Purdue University North Central

Production Editor:

Philip Weinsier
Bowling Green State University-Firelands

Subscription Editor:

Morteza Sadat-Hossieny
Northern Kentucky University

Financial Editor:

Li Tan
Purdue University North Central

Executive Editor:

Sohail Anwar
Penn State University

Manuscript Editor:

Philip Weinsier
Bowling Green State University-Firelands

Copy Editor:

Li Tan
Purdue University North Central

Publisher:

International Association of Journals and Conferences

Web Administrator:

Saeed Namyar
Namyar Computer Solutions

TABLE OF CONTENTS

Editor's Note: IJME Now Indexed by EBSCO 3
Philip Weinsier, IJME Manuscript Editor

Artificial Neural Networks for Realization and Verification of Digital Logic Circuits 5
Reza Raeisi & Amanpreet Kaur, California State University—Fresno

Performance Evaluation of a Variable-Speed Induction Motor Drive System with Active Input Power Factor Correction Circuit 10
Shiyoung Lee, The Pennsylvania State University Berks Campus

High-Speed Two-Phase SRM for an Air-Blower Drive 21
Dong-Hee Lee, Kyungsung University; Hyunh Khac Minh Khoi, TOSY Robotics JSC; Jin-Woo Ahn, Kyungsung University

Designing Sustainable Hybrid High-Brightness LED Illumination Systems 29
Akram A. Abu-aisheh, University of Hartford

Experimental Evaluation of a Bio-Based Cutting Fluid Using Multiple Machining Characteristics 35
Julie Z. Zhang, P.N. Rao, & Mary Eckman, University of Northern Iowa

Analysis of Solar Panel Efficiency through Computation and Simulation 45
Hongyu Guo, University of Houston-Victoria; Mehrube Mehrubeoglu, Texas A&M University-Corpus Christi

Mechanical Design of a Standardized Ground Mobile Platform 53
Nina P. Robson, J. Morgan, & H. Baumgartner, Texas A&M University

Centralized Vision-Based Controller for Unmanned Guided Vehicle Detection 58
Ravindra Thamma, Leela Mohan Kesireddy, & Haoyu Wang, Central Connecticut State University

Modeling Lead Vehicle Dynamics through Traffic Simulation and Field Data 66
Fang Clara Fang, University of Hartford; Fei Xue, University of Hartford

Instructions for Authors: Manuscript Submission Guidelines and Requirements 74

EDITOR'S NOTE: IJME NOW INDEXED BY EBSCO

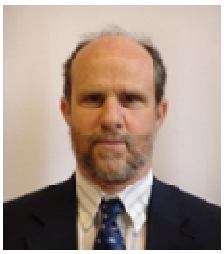

Philip Weinsier, IJME Manuscript Editor

EBSCO

IJME is proud to be part of EBSCO Subscription Services and EBSCO Publishing, which is a subsidiary of EBSCO Industries, Inc., ranked by Forbes as the 168th largest privately-owned company in the U.S. EBSCO Subscription Services has served library and research communities for more than 60 years. EBSCO Publishing is the most prolific aggregator of full text materials, offering a growing suite of more than 300 bibliographic and full-text databases available worldwide. EBSCO currently licenses over 77,000 full-text content sources, from over 5,100 publishers, for inclusion in its databases.

Established in 1944, EBSCO is recognized as the world's leading information agent providing consultative services and cutting-edge technology for managing and accessing quality content, including print and e-journals, e-packages, research databases, e-books and more, making it the leader in the database marketplace. Not only does EBSCO supply its databases to thousands of universities, biomedical institutions, schools, and other libraries in the United States and Canada, but the company is the leading database provider for libraries outside of North America. At present, EBSCO provides nationwide access to its databases in more than 70 countries, including developing nations with emerging economies.

Thomson Reuters ISI

IJME is currently under consideration for inclusion in the Thomson Reuters and DOAJ databases. With the breadth and scope of EBSCO's services, one might rightly ask why anyone would want or need to pursue indexing by yet other organizations. As it turns out, different organizations provide different kinds of services to aid readers and researchers alike in the pursuit of finding and quantitatively evaluating authors and journals.

Researchers, faculty, information scientists and librarians have been evaluating journals for the better part of the last 100 years. But, arguably, it wasn't until Thomson Reuters developed its citation indexes that it became possible to do computer-compiled statistical reports on the output of journals and the frequency of their citations. Then, in the 1960s, they invented the journal "impact factor", often abbreviated as IF, for use in their in-house analyses as part of their *Science Citation Index®*. Around 1975, they began publishing the information in their *Journal Citation Reports®* (*JCR*).

The *JCR®* provides quantitative tools for ranking, evaluating, categorizing, and comparing journals, of which impact factor is but one. Basically, impact factor is a measure of the frequency with which the average journal article has been cited, generally over a period of three years, and is calculated by dividing the number of current-year citations to the source items published in that journal during the previous two years. IF is frequently used to describe the relative importance of a journal within its field and is useful in clarifying the significance of total citation frequencies. What's more, it tends to level the playing field by eliminating biases related to a journal being large or small, and whether issues are published more or less often.

The Directory of Open Access Journals (DOAJ)

In their own words, the aim of the DOAJ is to increase the visibility and ease of use of open-access scientific and scholarly journals, thereby promoting their increased usage and impact; a one-stop shop to open-access journals. So while it is important for authors to publish their work, it is also important that readers be able to find and gain access to these published studies. The DOAJ helps to provide an overview of subject-specific collections and freely accessible online journals and integrate the information into a user-friendly library.

Editorial Review Board Members

Listed here are the members of the IAJC International Review Board, who devoted countless hours to the review of the many manuscripts that were submitted for publication. Manuscript reviews require insight into the content, technical expertise related to the subject matter, and a professional background in statistical tools and measures. Furthermore, revised manuscripts typically are returned to the same reviewers for a second review, as they already have an intimate knowledge of the work. So I would like to take this opportunity to thank all of the members of the review board.

As we continually strive to improve upon our conferences, we are seeking dedicated individuals to join us on the planning committee for the next conference—tentatively scheduled for 2013. Please watch for updates on our website (**www.IAJC.org**) and contact us anytime with comments, concerns or suggestions. Again, on behalf of the 2011 IAJC-ASEE conference committee and IAJC Board of Directors, we thank all of you who participated in this great conference and hope you will consider submitting papers in one or more areas of engineering and related technologies for future IAJC conferences.

If you are interested in becoming a member of the IAJC International Review Board, send me (Philip Weinsier, IAJC/IRB Chair, philipw@bgsu.edu) an email to that effect. Review Board members review manuscripts in their areas of expertise for all three of our IAJC journals—IJME (the International Journal of Modern Engineering), IJERI (the International Journal of Engineering Research and Innovation) and TIIJ (the Technology Interface International Journal)—as well as papers submitted to the IAJC conferences.

Kevin Berisso	Ohio University (OH)
Shaobiao Cai	Penn State University (PA)
Hans Chapman	Morehead State University (KY)
Michael Coffman	Southern Illinois U-Carbondale (IL)
Z. T. Deng	Alabama A&M University (AL)
David Domermuth	Appalachian State University (NC)
Mehran Elahi	Elizabeth City State University NC)
Ahmed Elsawy	Tennessee Tech University (TN)
Richard Freeman	US Coast Guard Academy (CT)
Nitish Gupta	Bhagwan Parshuram (INDIA)
Youcef Himri	Safety Eng. Sonelgaz (ALGERIA)
Xiaobing Hou	Central Connecticut State U. (CT)
Luke Huang	University of Southern Maine (ME)
Pete Hylton	Indiana University Purdue (IN)
Ghassan Ibrahim	Bloomsburg University (PA)
John Irwin	Michigan Technological Univ. (MI)
Fawwaz Jibri	
Sudershan Jetley	Bowling Green State U. (OH)
Khurram Kazi	Acadiaoptronics (MD)
Ognjen Kuljaca	Brodarski Institute (Croatia)
Zaki Kuruppalil	Ohio University (OH)
Ronald Land	Penn State University (PA)
Jay Lee	Purdue University Calumet (IN)
Shiyoung Lee	Penn State University Berks (PA)
Soo-Yen Lee	Central Michigan University (MI)
Chao Li	Florida A&M University (FL)
Dale Litwhiler	Penn State University (PA)
Thomas McDonald	University of Southern Indiana (IN)
David Melton	Eastern Illinois University (IL)
Sam Mryyan	Excelsior College (NY)
Arun Nambiar	California State U. Fresno (CA)
Ramesh Narang	Indiana U-Purdue University (IN)
Argie Nichols	Univ. of Arkansas Fort Smith (AR)
Basile Panoutsopoulous	Central Connecticut State U. (CT)
Karl Perusich	Purdue University (IN)
Thongchai Phairoh	Virginia State University (VA)
Patty Polastri	Indiana State University (IN)
Huyu Qu	Honeywell International, Inc.
John Rajadas	Arizona State University (AZ)
Sangram Redkar	Arizona State University-Poly (AZ)
Michael Reynolds	Univ. of Arkansas Fort Smith (AR)
Marla Rogers	Wireless Systems Engineer
Anca Sala	Baker College (MI)
Carl Spezia	Southern Illinois University (IL)
Li Tan	Purdue Univ. North Central (IN)
Li-Shiang Tsay	North Carolina A&T State U. (NC)
Liangmo Wang	Nanjing U. Science&Tech (CHINA)
Tom Warms	Penn State University (PA)
Jonathan Williams	Bowling Green State Univ. (OH)
Baijian (Justin) Yang	Ball State University (ILN)
Faruk Yildiz	Sam Houston State University (TX)
Biao Zhang	US Corp. Research Center ABB Inc
Chongming Zhang	Shanghai Normal Univ. (CHINA)
Jinwen Zhu	Missouri Western State Uni. (MO)

ARTIFICIAL NEURAL NETWORKS FOR REALIZATION AND VERIFICATION OF DIGITAL LOGIC CIRCUITS

Reza Raeisi & Amanpreet Kaur, California State University—Fresno

Abstract

Most of the time the processing capability and efficiency of computers are compared to that of a human brain. This comparison lays the basic foundation for Artificial Neural Networks (ANN). In today's technological age, neural networks are finding applications in almost every field. In this paper, an application of an ANN approach is presented to implement digital circuits. This approach provides an easier structural method for verification of digital logic circuits. Additionally, information about various neural network modeling tools is given. Also, a software tool is used to design a 5-bit Arithmetic Logical Unit (ALU).

Introduction

An Artificial Neural Network (ANN) is a network of several processing units known as neurons, where the information about the inputs and outputs is stored in the network in the form of interneuron connections known as weights. Each neuron has a fixed threshold value. Knowledge is acquired by the system through a learning process and is stored in the form of synaptic weights. When an input is given to the neuron, via an interneuron connection, the summation of the product of the synaptic input weights forms the weighted input. Then, it is subtracted from the threshold value to generate the activation of the neuron. Eventually, the activation is passed through the activation function to produce the output. The important part of ANN modeling is training, during which the value for the synaptic weight is computed by correlating the input with the output. This training procedure is similar to the learning process of the human brain. According to our experiences and knowledge, the strength of interneuron connections, or synapses, is altered in our brain [1].

The most significant characteristic of ANN is its use in applications where the user does not know the exact relationship between input and output. In this study, this advantage of ANN was explored by designing combinational digital circuits. Even though the relationship between input and output is known in combinational digital circuits, it is sometimes very complex and requires a lot of computing. Therefore, in this study, only the inputs and outputs were used for training and designing ANN models equivalent to the combinational digital circuit. The benefit of doing so is that this kind of modeling can be used for digital circuit functional verification and testing.

A discrete neuron model element can assume one of two possible states, 0 or 1. Figure 1 shows a neural architecture, referred to as a perceptron, which serves as a building block for primitive digital logic gates. Each perceptron can have multiple inputs and one output.

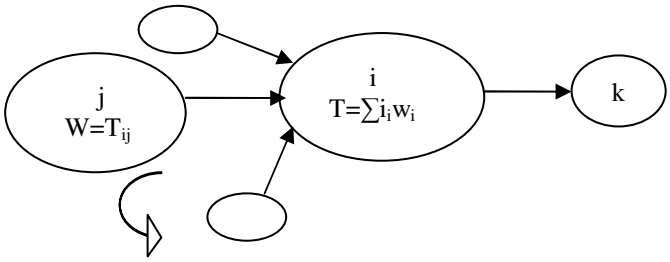

Figure 1. A Typical Neural Perceptron

A perceptron is connected to its neighbors through nets or signals similar to logic circuits and associated with a real number, T_{ij} , which connect perceptron *j* to *i*. A perceptron receives inputs from its neighbors and processes the inputs to produce its output function. A neural representation of digital logic gate primitives is shown in Figure 2 as a weighted graph, with the perceptrons represented as vertices and signals or nets as weighted edges. Each perceptron is also assigned a threshold. As an example, consider the neural network representation of a two-input AND gate shown in Figure 2. The AND gate neural element has three perceptrons labeled a, b, and c and whose thresholds are 0.5, 0.5 and 0.8, respectively.

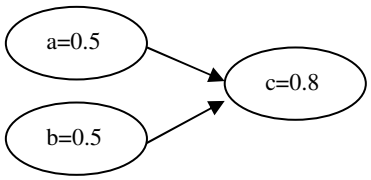

Figure 2. AND Neural Representation

A digital logic circuit with N gates can be realized with a neural network with N perceptrons, where the interconnections between the perceptron elements represent a specific Boolean logic expression. As an illustration, consider a neu-

ral network realization of an AND gate, with positive or negative weights for edges in the range of -1 and 1, and the threshold to be assumed in the range of -1 to 1. In an AND operation, both of the inputs need to be adequately high in order to produce an output. Assuming a threshold value of 0.8 for perceptron c, and setting the weights of the two edges at 0.5, then if both inputs of the AND gate are 1, the perceptron will have an activation output function of (1 * 0.5 + 1 * 0.5), which is greater than the output perceptron threshold and causes the perceptron to fire.

Modeling Digital Gates using ANN

The input and output signal states of a logic gate can be expressed in terms of minimum-energy function states, defined for an ANN. Similarly, a digital circuit can be expressed by a single energy function. In the development of an ANN model for digital circuits, it is important to determine if it is going to be a single layer or multiple layer ANN model. The decision variable for deciding the number of layers in ANN modeling is Decision Hyperplane. A hyperplane associated with neuron i can be expressed by Equation (1) [2]:

$$I_i + \sum_{j=1}^{n} T_{ji} V_j = 0 \qquad (1)$$

where I represents the threshold of the neuron; T represents the interconnection weight between neuron i and neuron j; and, V_i is the activation value of neuron i.

A hyperplane associated with neuron i is termed as decision hyperplane if the ON(1) and OFF(0) states of the system lie on the opposite sides of hyperplane and all other points lie on it. In such a case, ANN will form a single layer network. Otherwise, a multilayer ANN is formed. For instance, consider the case of a logical AND gate, the truth table for which is shown in Figure 3(a). In this case, the ON and OFF states of the AND gate can be separated by using a hyperplane, as shown in Figure 3(b). So, a single layer neural network is formed, as represented by Figure 3(c). This is also true for OR, NAND, NOR, and NOT gates.

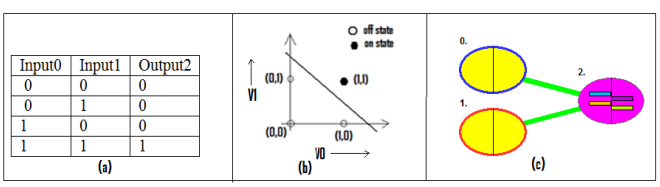

Figure 3. Neural Modeling of an AND Gate

In the case of an XOR gate, however, the ON and OFF states cannot be separated using a single hyperplane, as shown in Figure 4(b). So it forms a double layer network. An XNOR would represent a similar case.

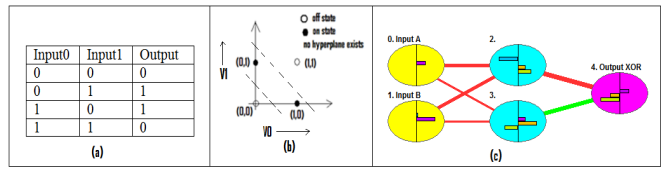

Figure 4. Neural Modeling of an XOR Gate

Designing an ANN Model

Once there is a basic understanding of the concept, there are various ways to design neural networks. Users can design and train neural networks using programming languages such as C++ , C# , Python, and Java. Beyond programming there are various software tools available which can be used to design neural networks. Some of them are listed here:

1. Matlab-Neural Network Toolbox
2. EasyNN-plus
3. Java Object Oriented Neural Engine
4. NNDef-Toolkit
5. Sharky Neural Network
6. A.I.Solver Studio
7. C# Neural network library

Amongst all these tools, EasyNN-plus was selected because it is particularly user friendly, and multilayer neural networks can be designed; the details of the neural network can subsequently be imported as text files. The only drawback with this tool is that it designs only feed-forward ANN models. In this study, 1-bit and 5-bit ALUs were designed using this tool.

Designing a 1-Bit ALU using EasyNN-plus

To design a 1-bit ALU using EasyNN-plus, the only thing required is ALU realization and then training the data for a functional 1-bit ALU and then just setting the required parameters. Once the parameters are set, the neural network can be designed and, eventually, verified by adding the query data to the training data. The opcodes used for designing this 1-bit ALU have been tabulated in Table 1. Using these opcodes, the data used for training, validating, and querying the neural network model are shown in Table 2.

Table 1. Opcode for a 1-Bit ALU

OPCODE	OPERATION
0	ADD
1	SUB
2	AND
3	OR
4	NOT
5	NAND
6	NOR
7	XOR

In Table 2, columns I:0 and I:1 represent the 1-bit inputs to the ALU; I:2 represents the opcodes; O:3 is the output; and O:4 represents the carry-over flag. In addition, the rows labeled T:n, where n is the row number, are the training examples. Examples used to validate the neural network are labeled V:n, where n is again the row number.

Table 2. Training for a 1-Bit ALU

	I:0	I:1	I:2	O:3	O:4
T:0	false	false	0	false	false
V:1	false	true	0	true	false
T:2	true	false	0	true	false
T:3	true	true	0	false	true
T:4	false	false	1	false	false
T:5	false	true	1	true	false
T:6	true	false	1	true	false
T:7	true	true	1	false	false
T:8	false	false	2	false	false
V:9	false	true	2	false	false
T:10	true	false	2	false	false
T:11	false	false	3	false	false
V:12	false	true	3	true	false
T:13	true	true	3	true	false
T:14	false	false	4	true	false
V:15	true	false	4	false	false
T:16	false	true	5	true	false
V:17	true	false	5	true	false
T:18	true	true	5	false	false
V:19	false	false	6	true	false
T:20	false	true	6	false	false
T:21	true	false	6	false	false
T:22	false	false	7	false	false
T:23	true	false	0	false	false
T:24	true	true	7	false	false
Q:25	false	false	0	false	false
Q:26	false	true	1	true	false
Q:27	true	false	2	false	false
Q:28	true	true	3	true	false
Q:29	false	false	4	true	false
Q:30	false	true	5	true	false
Q:31	true	false	6	false	false
Q:32	false	true	7	true	false

Finally, the query data are given by the user to verify the neural network model. In case of a query, the neural network model tries to predict the output for the given set of inputs. In this case, by giving a query and then verifying its output, the user can determine whether the neural network meets minimum error conditions or not. The other important factor is setting up the control values like average training error, number of layers, and learning rate. The dialog box for setting the controls is shown in Figure 5.

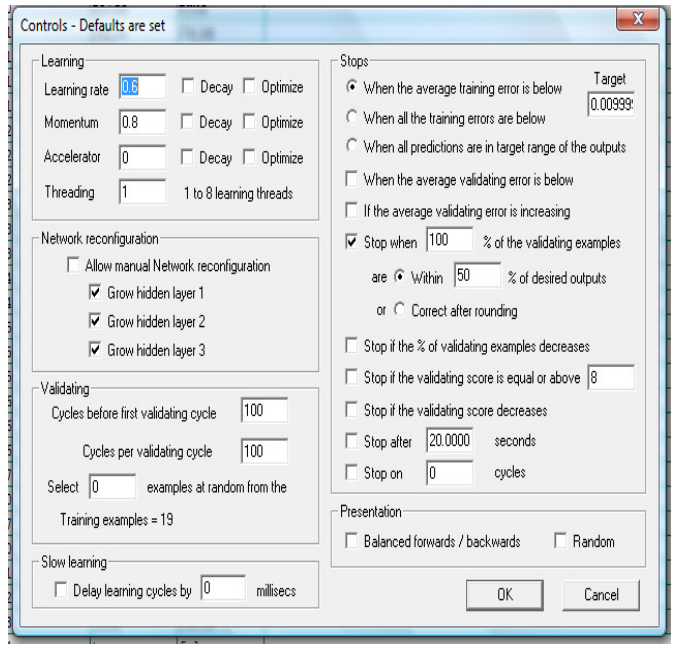

Figure 5. ANN Controls for Designing a 1-Bit ALU

After setting up the controls, the designer would press the "Start learning" button in the main panel window and the software will start designing the neural network and stop when the minimum validating error time is below the set value. The ANN model realization of a 1-bit ALU is shown in Figure 6. The details of this model are shown in Figure 7. The average training error was 0.13.

Designing a 5-Bit ALU

The design of a 5-bit ALU is similar to that of a 1-bit. Figure 8 shows the opcode table and control values for a 5-bit ALU. For this case, 11 input columns were used—ten columns for input data and one for the opcode. Using a procedure similar to the one described earlier, a neural network was designed and is shown in Figure 9. The average training error was 0.141056 for the training process of this 5-bit ALU neural network.

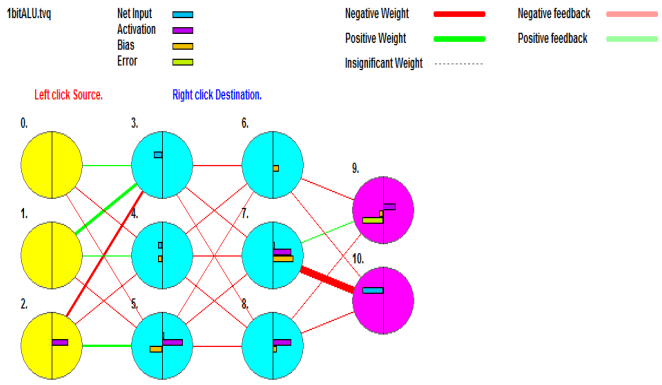

Figure 6. Neural Network Model for a 1-Bit ALU

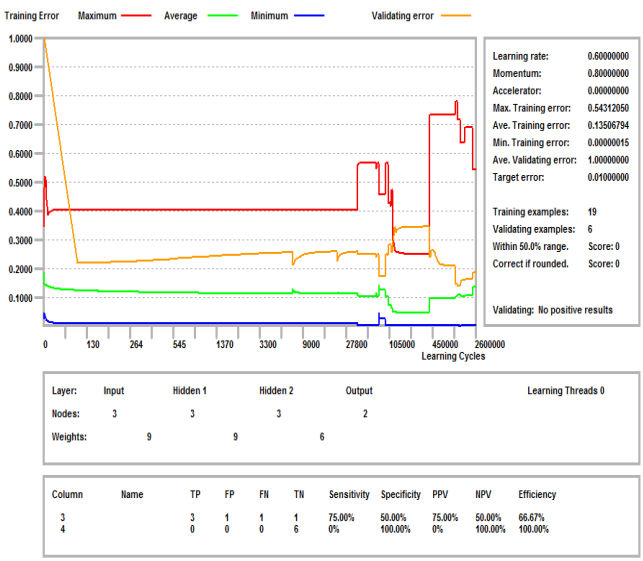

Figure 7. A 1-Bit ALU ANN Model

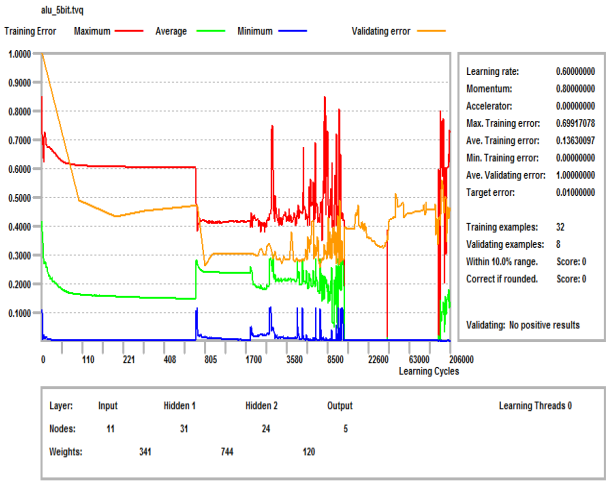

Figure 8. Details of a 5-Bit ALU

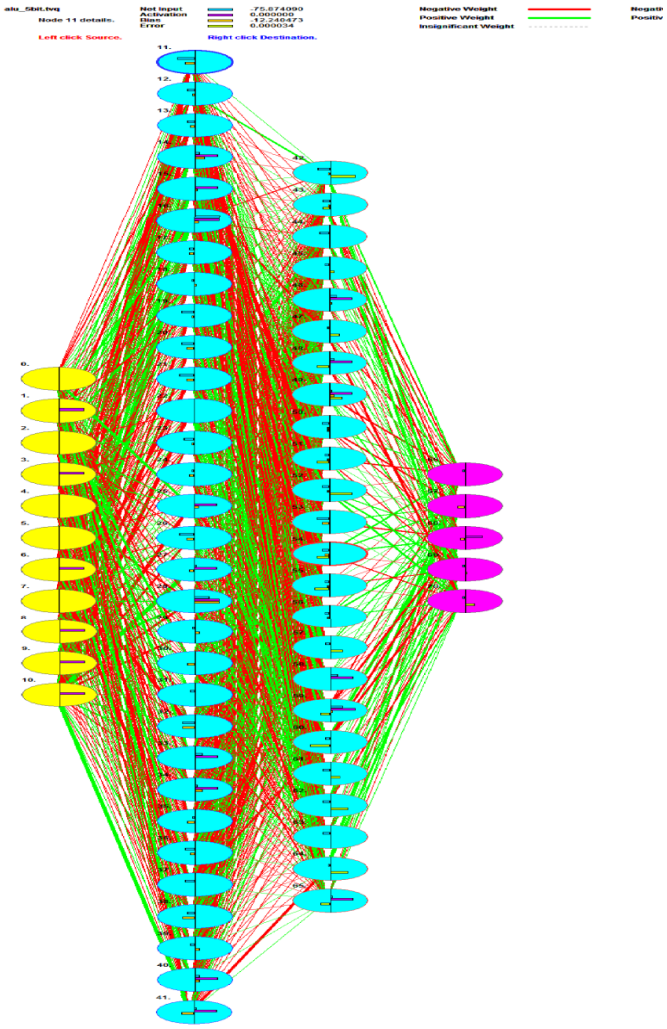

Figure 9. Neural Network Model of a 5-Bit ALU

Future Work

The Boolean Difference concept [3] was evaluated along with the proposed ANN digital logic realization technique for the testing of combinational circuits. The basic principle of the concept is to drive two Boolean expressions—one of which represents normal, fault-free behavior of the circuit, while the other represents logical behavior under an assumed single stuck-at-1 or stuck-at-0 fault condition. These two expressions are then realized using the ANN methodology for verification and Automatic Test Pattern Generation (ATPG) based on energy optimization of a Hopfield Neural Network [4], [5]. The block diagram for the proposed ATPG structure is shown in Figure 10 and consists of the following major components:

1. Circuit description containing a hard-coded form of the complete description of the circuit.

2. Energy surface generator to generate the energy surface for the circuit based on the Hopfield energy equation.
3. Test circuit is the circuit under test to be checked for faults.
4. Test circuit state table contains the functional state of the test circuit for the given inputs.
5. Fault Processing Unit takes the data from the energy surface and test circuit state table and processes them to determine if faults exist.

The implementation of the ATPG phase of this research work is currently under exploration.

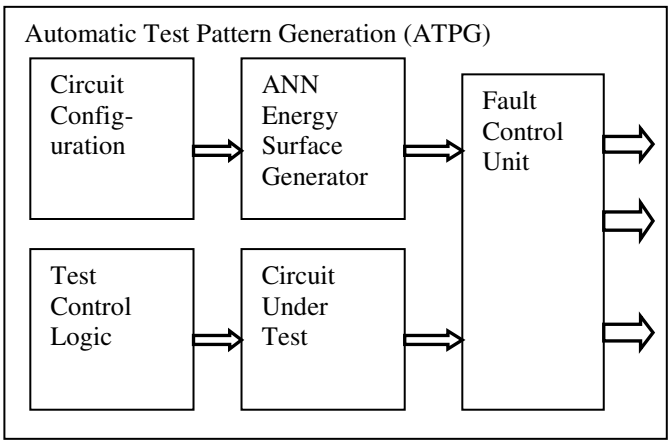

Figure 10. Block Diagram of ATPG

Conclusion

This paper presents a methodology for realization and functional verification of digital logic circuits using ANN as the building block to model digital logic circuits in a hierarchical method. Using ANN logical blocks, various combinational circuits were successfully modeled. An example of designing a 5-bit ALU with its functional verification was successfully implemented. The next phase of this research project is underway to use the ANN-modeling of digital circuits to test for faults and delays and generate automatic test patterns for a given circuit.

References

[1] Russel, S., & Norvig, P. (2003). *Artificial Intelligence: A Modern Approach*. Prentice Hall.

[2] Chakradhar, S. T., Agrawal, V. D., & Bushnell, M. L. (1991). *Neural Models and Algorithms for Digital Testing*. Kluver Academic Publishers.

[3] Lala, P. K. (1985). *Fault Tolerant & Fault Testable Hardware Design*. Prentice Hall International.

[4] Agrawal, V. D., & Seth, S. C. (1988). *Test Generation for VLSI Chips*. IEEE Computer Society Press.

[5] Hopfield, J. (1985). Neural computation of decisions in optimization problems. *Biological Cybernetics*, 52, 141-152.

Biographies

REZA RAEISI is currently an Associate Professor of Electrical and Computer Engineering Department at California State University, Fresno. He has been also serving as the Graduate Program Coordinator for the ECE department since 2008. He received his Ph.D. in 1990 and MS degree in 1985 both in computer engineering from University of Cincinnati. His research interests include integrated circuits, embedded systems, Application of Artificial Neural Networks in VLSI testing, and VLSI-CAD technology. He serves as Pacific Southwest regional director of American Society of Engineering Education. He is a Coleman Fellow and entrepreneur with over 20 years of domestic an international experience and professional skills in both industry and academia. Dr. Raeisi may be reached at rraeisi@csufresno.ed

AMANPREET KAUR is currently a Ph.D. student at University of California, San Diego. She received her MS in electrical engineering from California State University, Fresno in 2010. Her present research interest are application of Artificial Neural Networks and Genetic Algorithms for load forecasting and methods for reliable integration of variable resources like solar energy to the present grid. Ms. Kaur may be reached at a3kaur@ucsd.ed

PERFORMANCE EVALUATION OF A VARIABLE-SPEED INDUCTION MOTOR DRIVE SYSTEM WITH ACTIVE INPUT POWER FACTOR CORRECTION CIRCUIT

Shiyoung Lee, The Pennsylvania State University Berks Campus

Abstract

By employing an active input power factor correction (IPFC) circuit as a front-end converter for a variable-speed induction motor drive system, the author was able to demonstrate improvement of the system's power quality, which involved a high power factor (PF) and low total harmonic distortion (THD). This variable-speed motor drive (VSMD) can save more electrical energy than a fixed-speed motor drive, given that both operate on the same load factor. Few of the small VSMDs have IPFC circuits to save on their production costs. A three-phase, inverter-fed induction motor drive (IMD) with a single-phase source and an active IPFC circuit was developed in order to study the impact of an experimental IPFC circuit. The focus of this study of an input PF-corrected VSMD was on the effects of the circuit on overall system efficiency and input PF. Empirical comparisons between the conventional bridge rectifier circuit and IPFC circuit, in terms of PF and efficiency as they relate to motor speed, were made. A steady-state model of the IMD, including a three-phase inverter and an active IPFC circuit, was developed to predict system performance. The analytical results were correlated to the experimental results obtained from a prototype, one-horsepower IMD using a constant volts-per-hertz (V/Hz) control strategy. The overall system performance of the IPFC circuit was better than without it in terms of harmonic contents and PF. The system efficiency, however, showed marginal inferiority over the IPFC circuit as the front-end IPFC circuit and the three-phase inverter were connected serially. It should be emphasized that the IMD, with the IPFC circuit, was desirable in order to utilize the generated electrical energy effectively, while minimizing the harmonic contamination.

Introduction

Emerging applications of fractional-horsepower IMDs—such as compressors, appliances, blowers, hand tools, and heating, ventilating, and air-conditioning (HVAC)—invoke the urgency of studying the effects of the IPFC on the VSMDs [1-5]. The necessity for efficient utilization of generated electrical energy is growing in significance in order to optimize the usage of utility power plant capacity. Moreover, awareness of minimizing harmonic contamination in the electric power line is rising due to the increased use of electronic equipment powered by an ac-to-dc bridge rectifier with large filter capacitors and/or a switch-mode power supply (SMPS).

One of the most active research and development areas in the power electronics field is VSMD [6-14]. As power semiconductor devices become cheaper, faster and more reliable, the use of energy-saving VSMDs in industry and residential applications has been increasing. VSMDs utilizing induction and dc motors make up the majority of industrial and domestic drives. Although these VSMDs require an initial investment and generate current harmonics, they provide significant improvements in performance such as better control, wider speed ranges, soft start, and enormous energy savings in various kinds of applications. The selection of VSMDs is an application-specific matter. There are many factors to be considered when selecting VSMD systems, including cost, output torque, speed ranges, performance, and power ratings.

The emerging requirement in VSMD applications for drawing near sinusoidal current from the utility and fewer harmonics being injected into the utility lines is the motivation for investigation of the PF-corrected motor drive system. The impact of IPFC on system efficiency and power converter ratings is to be studied for the high-volume but low-cost applications such as washers, dryers, refrigerators, freezers, hand tools, and process drives. The power ratings for most of these high-volume applications are less than one -horsepower.

All off-line VSMDs have rectifiers and storage capacitors in their front-ends to get dc voltage from an ac power source. This input circuitry lowers the PF of the VSMD systems and pollutes ac power systems. The PF is the ratio of real power in watts (W) to apparent power in volt-amperes (VA). The PF becomes unity when the input ac current and voltage are sinusoidal and in phase. In an off-line VSMD system, the input current is distorted and even out of phase with the input voltage, the power factor is less than unity, and less real power is transmitted to the load. However, the rms input current is increased due to the har-

monic currents, plus the current required by the load must still be carried, thus requiring the wiring of the ac power system to be heavier and more expensive than necessary.

The most common problem with ac power systems is caused by electric motors operating in industries. The inductive component of the motors causes the ac current to lag the ac voltage. This results in a low power factor. Assuming the loads are linear, the power factor can be corrected to near unity by connecting a bank of capacitors across the ac power line. The low PF gives rise to a number of serious problems in VSMD systems. The size of the input fuses and circuit breakers of the input circuitry must be increased. The distorted input current waveform, which causes interference with other equipment, must be filtered to reduce the magnitude of the harmonic frequencies. Consequently, to increase the output power from ac power systems, it is necessary to correct the PF. This substantially reduces peak and rms input current and makes it possible to achieve higher output power.

With the proliferation of nonlinear loads such as SMPSs, standards agencies around the world are developing requirements for harmonic contents of the electronic power conversion systems to reduce the overall distortion on the main supply line. One of these standards is the IEC 1000-3-2 (same as EN 61000-3-2 published in 1995 and the latest version of IEC 555-2 published in 1982) [15] from the International Electrotechnical Commission (IEC) to set the limits for input harmonic currents in the electrical equipment. The standard describes general requirements for testing equipment as well as the limits and the practical implementations of the test. For the purpose of harmonic current limitation, the standard divides electrical equipment into four classes, as shown in Figure 1. Each class has different harmonic current limits. Any balanced, three-phase equipment or other electronic apparatus which do not fall into either Class B, C, or D will automatically be moved to Class A. To apply a Class D limit, the following two requirements should be satisfied:

- Input power should be less than 600W.
- The input current waveshape of each half cycle should be within the envelope shown in Figure 2 for at least 95% of the duration of each half period.

The center line in Figure 2 coincides with the peak value of the input current. The second requirement implies that the waveform, having a small peak outside the envelope, is considered to fall within the envelope. In Class D limits, for equipment with input power greater than 75W, relative limits (mA/W) should be applied; otherwise, absolute limits will be applied. The specified limits of the IEC 1000-3-2 standards are applicable to electrical equipment having an input current up to 16A per phase with nominal voltages of 230V with single-phase frequencies of 50 or 60Hz, and the harmonic currents of interest are from the 2nd to 40th harmonic.

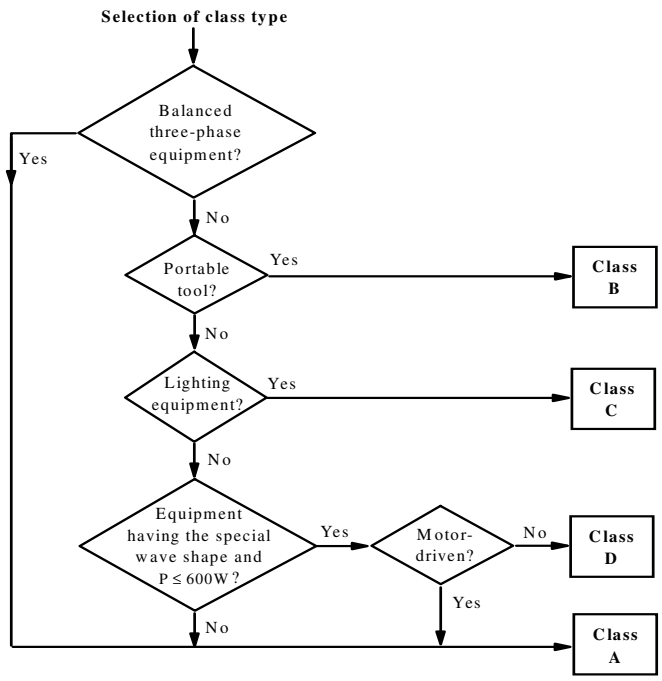

Note. Motor-driven: Phase Angle Controlled

Figure 1. Flowchart for Class Determination of Electrical Equipment by IEC 1000-3-2 Standards

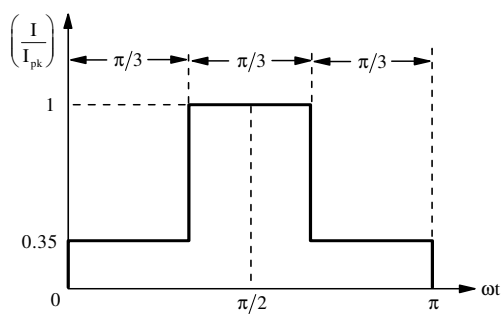

Figure 2. Class D Waveform Envelope

The appliance VSMDs fall into the Class A or D categories, depending on whether they use a phase-angle controlled VSMD, and their input power range is less than or greater than 600W. The VSMDs, which were investigated in this study, have front-end rectifier circuits to convert ac voltage into dc voltage. The ac input current of the VSMD has a pulse-type waveform, which falls into the Class D

envelope regardless of the magnitude of its input power because the pulse current is normalized based on its peak value. If the input power of a VSMD is over 600W, a Class A limit should be applied. Otherwise, the Class D limit will be applied. Therefore, in this study, only the Class A and D limits were employed to verify the effects of IPFC and IEC 1000-3-2 standards.

Single-Phase IPFC Topologies

The study of IPFC topologies is limited here to the single-phase version because most of the appliance VSMDs are powered by a single-phase utility source. The classification of single-phase, off-line IPFC topologies for VSMDs [16-19] is shown in Figure 3. Among these IPFC topologies, low frequency active, resonant and isolated types were not considered in this study. A passive IPFC [18] is more reliable than an active IPFC because no active devices are utilized. However, it has bulky capacitors and inductors operating at line frequency, and it is sensitive to the line frequency, line voltage, and load. Therefore, this method is not suitable for appliance drives. The most popular active IPFC method is the boost topology [16]. This topology is a universal solution for SMPS to small-motor drive applications. It has a smooth input current because an inductor is connected in series with the power source, showing a low level of conducted electromagnetic interference (EMI) noise. This topology has a high output voltage which is greater than the peak input voltage. The overload and start-up currents cannot be controlled in this topology because there is no series switch between the input and output path. Also, isolation between the input and output cannot be easily implemented.

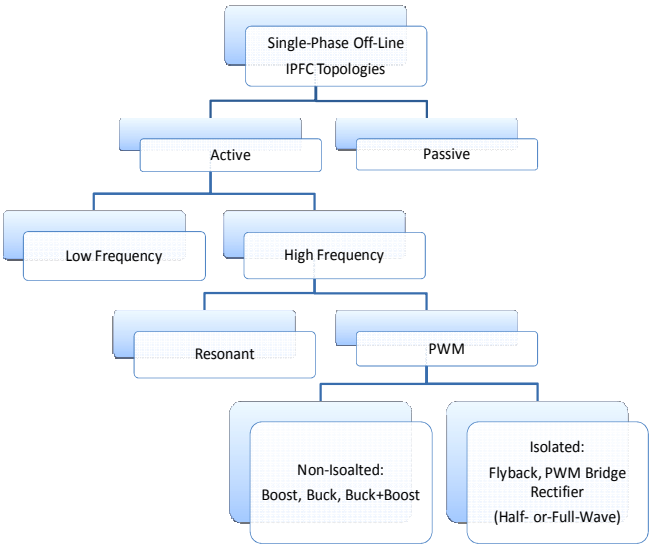

Figure 3. Classification of Single-Phase IPFC Topologies for Small VSMD Systems

The buck-type IPFC has lower output voltage than input voltage and it has a pulsating input current, which generates high harmonics in the power line. This circuit is not practical for low-line inputs because it does not draw the input current when input voltage is lower than output voltage. Therefore, it has a relatively low power factor compared to the boost IPFC circuit. The buck-type IPFC is suitable for charger applications due to its voltage step-down nature [17].

The SEPIC (single-ended primary inductor converter) IPFC circuit has a single power switch driven at high frequency, as with the boost IPFC topology, but it needs extra inductive and capacitive passive components for energy storage and transfer. The input current of SEPIC is smoothed by employing an inductor in series with the power source. This circuit can be easily modified to the isolated version. A cascaded converter, which has a buck circuit in the front and boost circuit in the second stage, is introduced by Singh & Singh [6]. The buck switch is turned on when the input voltage is below the output voltage. This causes the circuit to operate as a boost converter. When the input voltage is higher than the output voltage, the boost circuit is stopped and the buck circuit restarts. This converter can supply step-up or step-down outputs; thus, it can operate over a wide range of inputs. There is no inrush current due to the buck switch, which is in series with the power source, but it has a pulsating input current which requires more filtering.

Another non-isolated IPFC topology is the pulse width modulation (PWM) bridge rectifier. This topology can also supply step-up or step-down outputs, similar to the buck-boost circuit. The PWM bridge rectifier circuit needs two or four power switches to yield a unity power factor because it employs a half- or full-bridge configuration. It also needs a more complicated control circuit than the boost topology, but for high-power applications, it may be a good candidate.

Proposed IPFC-IMD System

The proposed IPFC-IMD system for this study is shown in Figure 4. Note that the IPFC circuit can be replaced with a single-phase diode rectifier bridge circuit for a comparative study. IPFC has both input current and voltage feedbacks in order to obtain the sinusoidal input current. The output voltage sensing circuit rejects the adverse effect of load variation on the dc link voltage. The inverter power circuit is made up of MOSFET devices and operates at 2.78kHz with PWM control. The control strategy is a constant V/Hz with the offset adjustment. In this study, the offset was fixed at a value equal to the rated stator resistive voltage drop. The drive had an inner rotor speed feedback

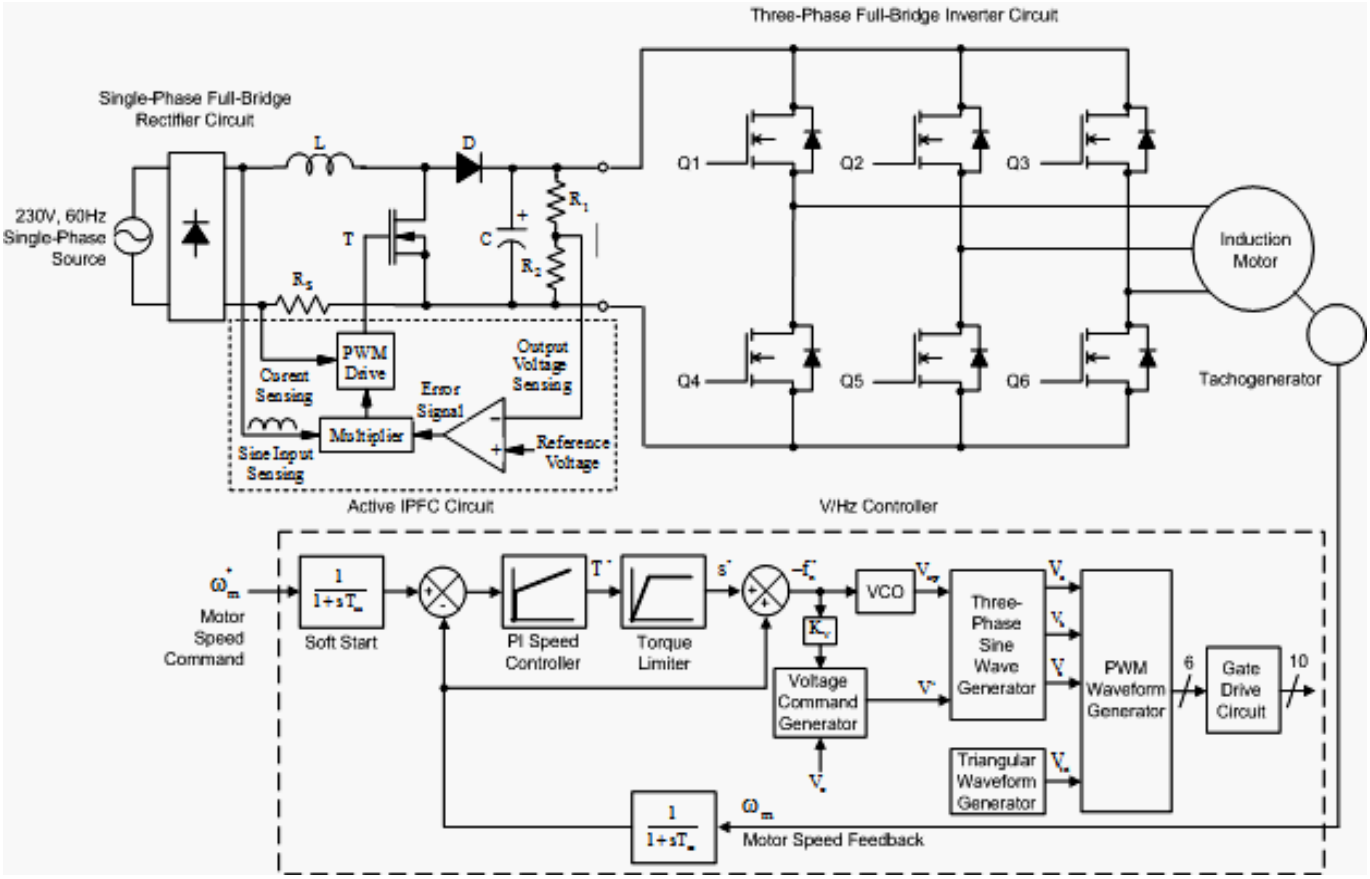

Figure 4. Proposed IPFC-IMD System

loop to control the slip speed. This limited the stator current effectively over the range of speed variation.

Principle of Operation of the Boost IPFC Circuit

The principle of operation of the boost IPFC circuit, which was selected for the VSMD system, is explained in this section. The predicted efficiency of the boost PFC pre-regulator was obtained with derived analytical equations and compared with experimental results. The harmonic contents in the input current of the boost PFC circuit were compared with the IEC 1000-3-2 standards [15], [20]. In a VSMD, the ac utility input voltage must be converted to dc with a rectifier circuit, as shown in Figure 4. This circuit has the advantages of simplicity, low cost, high reliability, and no need of control. However, it has the disadvantages of low PF due to the presence of rich harmonics in its current and a high peak-current magnitude, as shown in Figures 5 (a), (b), and (c). This relationship was obtained from the PSpice simulation of a single-phase diode bridge rectifier circuit and was normalized to the peak value.

The input circuitry of an off-line VSMD consisted of rectifier diodes to convert ac into pulsating dc, and filter capacitors to smooth the pulsating dc voltage, as shown in Figure 4. This input circuitry presents rich harmonic currents to ac power systems that are quite different from motor loads because it appears as a nonlinear load to ac power systems. In the input circuitry, ac current pulses occur because the filter capacitor remains charged to nearly the peak value of the ac input voltage.

During most of each half cycle of the input voltage, the rectifier diodes remain reverse biased; thus, no current flows. Because the filter capacitors partly discharge during each half-cycle, the input voltage exceeds the capacitor voltage for a short time near the peak value of the input voltage. As the input voltage surpasses the capacitor voltage, the input current begins to flow abruptly into the capacitor. After the capacitor is charged almost to the peak value of the

input voltage and the input voltage begins to decrease, the input current falls to zero. Also, it causes overheating of the power lines and distribution transformers. Under extreme conditions, other sensitive electronic equipment connected to the same power line can be affected by noise related to electromagnetic interference (EMI).

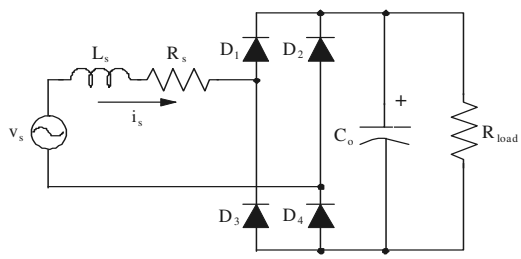

a) A Single-Phase Diode Rectifier Circuit with Capacitor

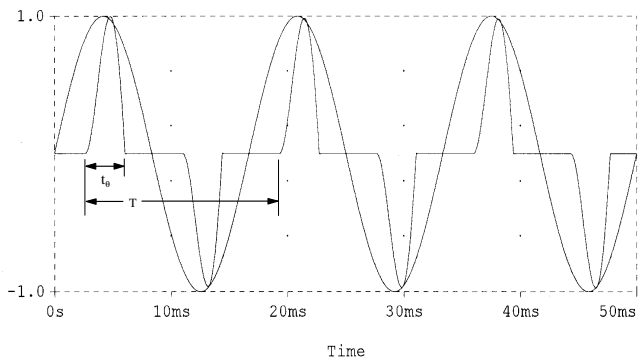

b) Normalized Input ac Voltage, v_s and Current, i_s

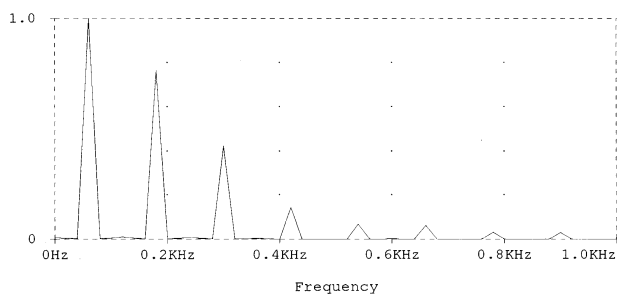

c) Normalized Harmonic Spectrum of Current i_s

Figure 5. Analysis of Current Harmonic Contents in the Diode Bridge Rectifier Circuit with Capacitor by Simulation

As required by various standards, the line harmonics produced by a VSMD must be below certain limits, which increase the input PF. The high PF is desirable to both the user and the utility company because it is possible to get maximum power from an ac service outlet and to utilize the generated power efficiently and cleanly. It is also possible to reduce the wiring and power transformer losses in the utility network with high PF. With increasing demand for more power and better power quality from a standard power line, the IPFC circuit will become an integral part of VSMDs in the near future.

The boost IPFC circuit is an economical solution to the need for complying with the regulations. It can be implemented with a dedicated single-chip controller; therefore, the circuit becomes relatively simple with a minimum number of components. The boost inductor in the boost IPFC circuit is in series with the ac power line; thus, the input current does not pulsate and the conducted EMI at the line is minimized. This allows the size of the EMI filter and the conductors in the input circuit to be reduced. This topology inherently accepts the wide input voltage range without an input voltage selector switch. For example, the UC3854 PF controller chip from Texas Instruments [21] accepts an input voltage of 75 – 275VAC and a frequency of 50–400Hz. It cannot limit overcurrent at start-up or fault conditions because there is no switch between the line and the output.

The output voltage of a boost IPFC circuit should be higher than the peak value of the maximum input voltage. Even though this is a simple topology, it must be designed to handle the same power as the main power converter. Only the single-phase boost IPFC circuit operating in the continuous-inductor-current mode was addressed in this study. The simplified block diagram of the boost IPFC circuit is shown in Figure 4. This circuit has two control loops. One is the fast-acting internal current loop, which defines the input current shape to be sinusoidal and places it in phase with the input voltage. The other is the external voltage loop, which regulates the output dc voltage. The voltage loop should not react to the 120Hz rectified mains variations, so its bandwidth was lowered to 10 to 20Hz. The current loop usually has a bandwidth frequency of less than one tenth of the switching frequency.

The principle of operation of the boost IPFC is as follows: the rectified sinusoidal input voltage goes to a multiplier circuit, providing a current reference to the multiplier and a feedforward signal proportional to the rms value of the line voltage. The filtered dc output voltage of the boost IPFC is compared to a reference voltage and amplified. The error amplifier senses the variations between the output voltage and the fixed dc reference voltage. The error signal is then applied to the multiplier. The multiplier's output follows the shape of the input ac voltage, with an average value inversely proportional to the rms value of the ac input voltage. This signal is compared to the sensed current signal in a PWM circuit. The inductor current waveform follows the shape of

the rectified ac line voltage. The gate drive signal controls the inductor current amplitude and maintains the constant output voltage.

Derivation of the Steady-State IPFC-IMD System Model for Analysis

Steady-state loss models of the induction motor, load, inverter, IPFC circuit, and bridge rectifier were developed and a procedure to compute various subsystem variables is presented in this section.

The load and its requirements are known and, hence, they constitute the starting point for the steady-state performance computation. Using the rotor speed and the load power with the inverter output voltage equation, induction motor equations, and load equations, the overall system equations were assembled. What follows is the solution of the system equation iteratively for the slip, stator frequency and all other variables for each speed with a specific load.

As the stator phase current was given, the inverter losses could be computed with switching and conduction loss equations. The input power to the inverter could be calculated with the inverter losses combined with the induction motor input power. The sum of inverter input power and the IPFC circuit losses yields the input power from the ac mains supply. The solution of the input power leads to a complete solution of the steady-state performance of the IPFC-IMD system.

Bridge Rectifier

Only the diode conduction losses were considered. The conduction losses in a single-phase rectifier bridge, P_{br} , are given by Equation (1),

$$P_{br} = 2V_d I_{in} = 2V_d \cdot \frac{P_{in}}{V_{in}} \tag{1}$$

where V_d is the forward diode voltage drop, I_{in} is the ac input current, V_{in} is the ac input voltage, and P_{in} is the ac input power from the ac mains supply.

IPFC Circuit

The IPFC circuit has a single power device with a forward diode in the boost configuration. The peak current in the boost inductor in terms of the ac input current, I_{in}, is

$$I_p = \sqrt{2} I_{in} = \frac{\sqrt{2} P_{in}}{V_{in}} \tag{2}$$

The IPFC circuit is designed to operate with 10% ripple current in the boost inductor. The current in the power switching device is,

$$I_{sw} = \sqrt{\frac{I_p^2}{2} - I_d^2} \tag{3}$$

where I_d is the boost diode current given by,

$$I_d = I_p \sqrt{\frac{4V_o}{3\pi V_{pk}}} \tag{4}$$

and where V_o is the dc output voltage of the IPFC circuit and V_{pk} is the peak rectified ac line voltage.

The losses in the boost switch are modeled as

$$P_{sw} = I_{sw}\left[\frac{1}{2} V_{pk} f_c \left(t_{rp} + t_{fp}\right) + I_{SW} R_{ds}(on)\right] \tag{5}$$

where t_{rp} and t_{fp} are the rise and fall times of the boost power switch, respectively.

$R_{ds}(on)$ is the on-state drain-to-source resistance of the MOSFET power device and f_c is the carrier frequency of the IPFC circuit.

The losses in the boost diode are

$$P_d = I_d\left(\frac{1}{2} V_{dc} f_c t_{rrd} + V_d\right) \tag{6}$$

where t_{rrd} is the reverse recovery time of the boost diode in the IPFC circuit.

The losses in the boost inductor are

$$P_{ind} = R_{dc} I_{in}^2 \tag{7}$$

where R_{dc} is the dc resistance of the inductor.

The losses, P_{bripfc}, in the diode bridge rectifier when the IPFC circuit is used are given by

$$P_{bripfc} = 2 I_{ave} V_d = \frac{2}{\pi} I_{pk} V_d \tag{8}$$

where I_{ave} is the average current in the single-phase bridge rectifier and V_d is the forward conduction voltage drop in the diodes.

The total losses in the IPFC circuit, including the controller power supply losses, P_{ps}, is obtained as

$$P_{ipfc} = P_{bripfc} + P_{sw} + P_d + P_{ind} + P_{ps} \quad (9)$$

Inverter

The inverter output phase voltage is designed as a function of stator frequency command of the induction motor and given as

$$V_i = V_{as} = V_{of} + k_{vf} \cdot f_s \quad (10)$$

where V_{of} is the offset voltage given by

$$V_{of} = I_b R_s \quad (11)$$

The constant, k_{vf}, is given by

$$k_{vf} = \frac{V_b - V_{of}}{f_b} \quad (12)$$

where I_b is the base stator phase current, V_b is the base stator phase voltage, and f_b is the base stator frequency.

The inverter switching loss, P_{isw}, and conduction loss, P_{icon} , are modeled as

$$P_{isw} = m\left[\frac{1}{2} V_{dc} I_s f_{sw} \left(t_r + t_f + t_{rr}\right)\right] \quad (13)$$

$$P_{icon} = m I_s^2 R_{ds}(on) \quad (14)$$

where t_r and t_f are the rise and fall times of the power devices, respectively, and t_{rr} is the reverse recovery time of the freewheeling diodes. And, f_{sw} is the inverter switching frequency, $R_{ds}(on)$ is the on-state resistance of the MOSFET power device, and V_{dc} is the dc link voltage input to the inverter.

Induction Motor

A single-phase equivalent circuit of the three-phase induction motor is shown in Figure 6 [22], [23]. The loop voltage equations from the equivalent circuit are

$$V_{as} = (R_s + j\omega_s L_{ls}) I_s + Z_o I_o \quad (15)$$

$$0 = \left(\frac{R_r}{s} + j\omega_s L_{lr}\right) I_r + Z_o I_o \quad (16)$$

where

$$I_s = I_r + I_o \quad (17)$$

$$Z_o = j\frac{\omega_s L_m R_c}{(R_c + j\omega_s L_m)} \quad (18)$$

and where I_s, I_r, and I_o are the stator, rotor, and magnetizing branch currents, respectively. V_{as} is the stator phase voltage, w_s is the stator angular speed, R_s is the stator phase resistance, and R_r is the stator referred rotor phase resistance. L_m, L_{ls}, and L_{lr} are the magnetizing, stator leakage, and stator referred rotor leakage inductances per phase, respectively, and s is the slip given by

$$s = \frac{\omega_s - \omega_r}{\omega_s} = 1 - \frac{\omega_r}{\omega_s} = 1 - \frac{P}{2} \cdot \frac{\omega_m}{\omega_s} = 1 - \frac{nP}{120 f_s} \quad (19)$$

where w_m and w_r are rotor mechanical and electrical angular speed, respectively, N is the rotor speed in r/min, P is the number of poles, and f_s is the supply stator frequency.

The mechanical power developed in the rotor, P_m, for the m-phase machine is given by

$$P_m = m I_r^2 R_r \cdot \frac{(1-s)}{s} \quad (20)$$

where m is the number of phases (three) in this study.

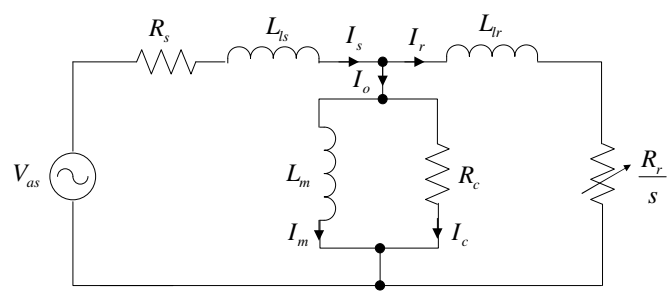

Figure 6. Single-Phase Equivalent Circuit of the Three-Phase Induction Motor

Load

The load power, P_o, is related to the induction motor output in steady-state by

$$P_o = P_m - P_{fw} \quad (21)$$

where P_{fw} is the friction and windage losses.

In general, the output of any load is given as

$$P_o = P_b\left(\frac{n}{n_b}\right)^k \quad (22)$$

where P_b is the base power, n_b is the base speed in r/min and k is 1, 2, and 3 for constant, frictional, and fan-type loads, respectively. Note that P_{fw} is the function of motor speed, n.

Discussion of Experimental Results

From the experimental data containing the friction and windage losses, the parameters of the induction and dc machines were calculated and, in conjunction with other measurements, the induction motor output was determined for each operating point. Then, the system and induction motor efficiencies, system input PF, system line current, motor currents, and IPFC circuit efficiencies were calculated from the empirical data.

The speed of the induction motor was varied from 500 r/min to 3,000 r/min (0.87 p.u.), and the output power at the base speed (3,450 r/min) was 1 hp. The empirical data were obtained for the system with and without the IPFC circuit, and by keeping the input system voltage at 230V.

Input Current Harmonics in the Boost IPFC Preregulator

The sample input current waveform and its harmonic contents of the prototype 2kW IPFC preregulator with a 1400W load are shown in Figure 7. The steady-state harmonics were measured by Fast Fourier Transformation (FFT) with the rectangular windowing function. The input ac current closely followed the sinusoidal voltage waveform, as designed. The PF of this operating point was calculated as 99% using the following equations:

$$Power\ \ Factor = \frac{Real\ Power}{Apparent\ Power} = \frac{V_{rms} \cdot I_1 \cdot cos\,\phi}{V_{rms} \cdot I_{rms}} = \frac{I_1}{I_{rms}} \cdot cos\,\phi \tag{23}$$

$$I_{rms} = \sqrt{I_1^2 + I_3^2 + \cdots + I_n^2} \tag{24}$$

where V_{rms} is the ac input rms voltage, I_{rms} is the input ac current, I_1 is the fundamental component of I_{rms} and $cosf$ is the phase angle between input ac voltage and the fundamental current. The harmonic spectra of the input current with the IPFC circuit are shown in Figure 7. The input ac current closely follows the sinusoidal voltage waveform as designed. The comparison of the measured input current harmonic spectra magnitude with the modified IEC 1000-3-2 Class A limit is shown in Figure 8. The harmonic spectra of the input current with the IPFC circuit are vastly improved compared with one in the bridge rectifier circuit with a capacitor. This validates the effectiveness of the IPFC.

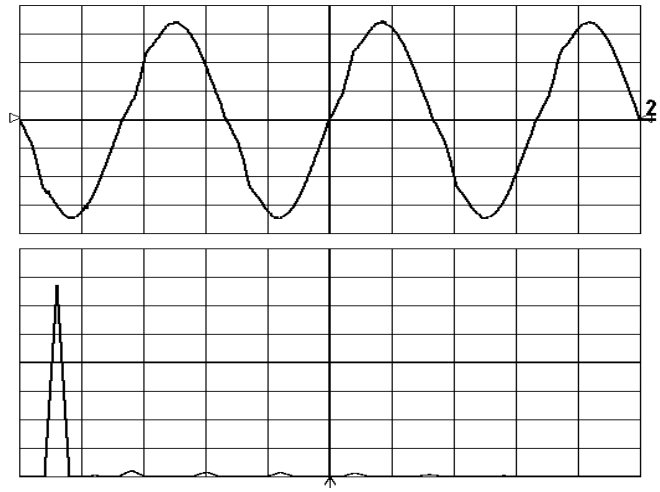

Figure 7. Experimental Waveforms of the 2kW PFC Preregulator with 1.4kW Load (top) Input Current (5A/div, 5ms/div) (bottom) Input Current Harmonic Spectra (2.5A/div, 0.1kHz/div)

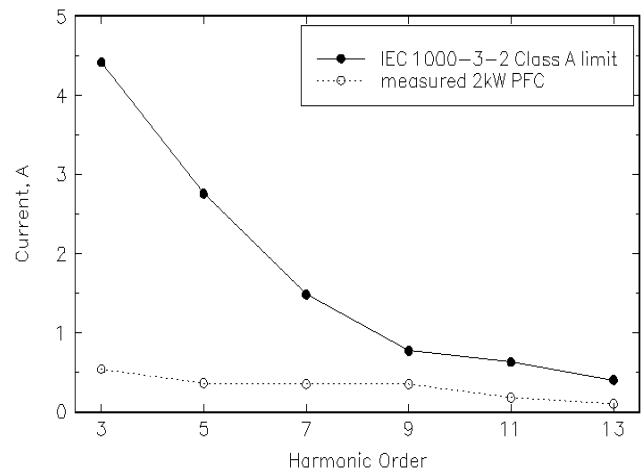

Figure 8. Comparison of Measured Input Current Harmonic Spectra from Figure 7 with Modified IEC 1000-3-2 Class A Harmonic Current Limit

Experimental waveforms of the system input current and induction motor stator current at 1 p.u. speed and load torque are shown in Figures 9 and 10, for both the bridge rectifier- and IPFC-based VSMD systems along with their frequency spectra. The IPFC-IMD system was free of harmonics in the system input current. The induction motor stator currents were practically the same with minor variations in their frequency spectra. The speed variation hardly affected these waveforms.

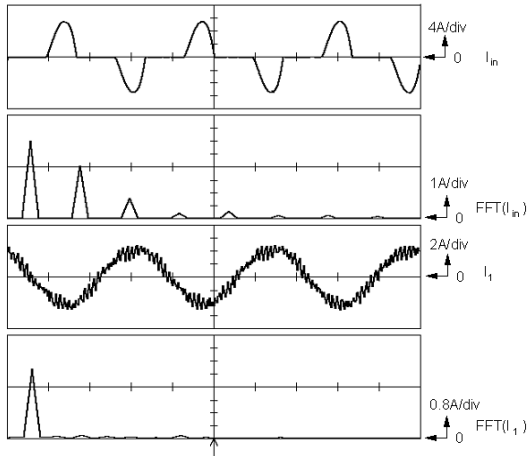

Figure 9. System ac Input Current (top) and Motor Stator Current (bottom) and their FFT with Diode Bridge Rectifier Front-end (Horizontal/div: Currents = 5ms, FFT = 100Hz)

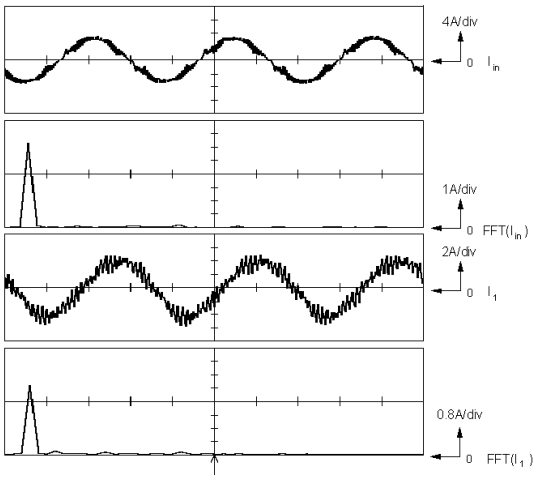

Figure 10. System ac Input Current (top) and Motor Stator Current (bottom) and their FFT with IPFC Circuit (Horizontal/div: Currents = 5ms, FFT = 100Hz)

Efficiencies of the IPFC Circuit and the IMD System

In Figure 11, the efficiency of the 2kW IPFC circuit employed in this study remained level above 95% over the entire output power range. The predicted efficiency matched closely with the measured one over the entire power range. This validation of the derived loss models has practical usefulness in estimating losses in the boost IPFC preregulator.

The system input PF, input current, and overall IMD system efficiency versus motor speed for systems either with or without the IPFC preregulator are shown in Figures 12(a), (b), and (c) for the friction load. The IPFC-based IMD showed a higher input PF over the entire speed range than one with a non-IPFC system. Hence, the IPFC-IMD system required lower input current to generate the same output compared with a non-IPFC system. The benefit of requiring less input current was noticeable over 0.4 p.u. speed. The non-IPFC system showed higher system efficiency up to 0.75 p.u. speed, but the IPFC-based system showed higher system efficiency beyond that speed with a friction load. This is attributed to the fact that the stator current decreases with the decreasing stator voltage of the non-IPFC system. The non-IPFC system efficiency was approximately 2 to 4% higher than that of the IPFC-based system.

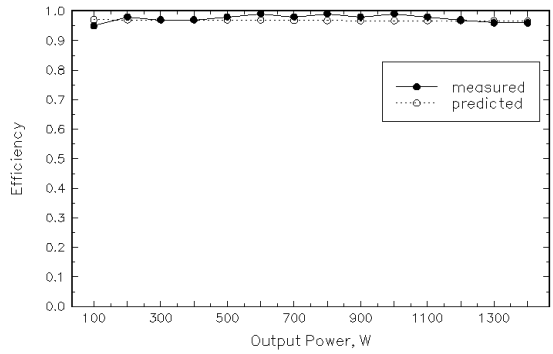

Figure 11. Measured and Predicted Efficiencies for the Developed 2kW Boost IPFC Preregulator

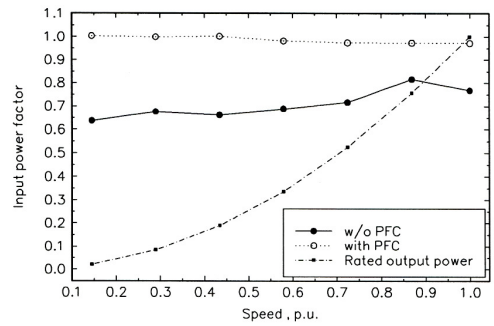

a) System Input PF

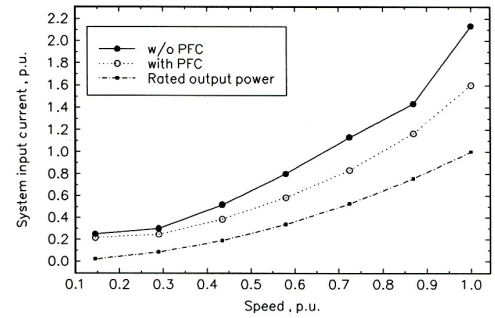

b) System Input Current

Figure 12. Input PF, Current, and System Efficiency with and without IPFC with Friction Load (continued on next page)

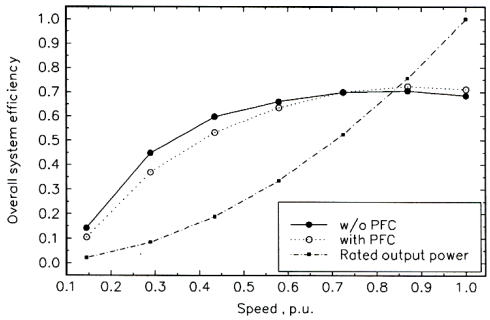

c) Overall system efficiency

Figure 12 (continued). Input PF, Current, and System Efficiency with and without IPFC with Friction Load

The effect of IPFC to the three-phase inverter performance in terms of output voltage and current are shown in Figures 13(a) and (b). The IPFC-IMD system showed higher output voltage than the one with the non-IPFC system because of the tight output voltage regulation of the IPFC control circuit. The inverter needed less current output to drive the IMD to the same speed.

However, the IPFC benefits from the efficiency of the induction motor slightly over 0.6 p.u. speed. The system and motor efficiencies were very poor for speeds lower than 0.3 p.u., as the output was very small in this region and the losses were many times that of the output in that speed range. The usual variation of speed range was 0.4 to 1 p.u. for the friction load; hence, the low-speed operation with low efficiency may not be of immense importance.

Conclusions

The system steady-state model for both the bridge rectifier- and IPFC-based IMD were formulated, and a steady-state computational procedure was developed. The model was experimentally verified with a 1-hp laboratory prototype IPFC-IMD system and was found to be fairly accurate.

A comparison between the non-IPFC- and IPFC-based systems was made for the friction type load. The non-IPFC system was preferable in terms of system efficiency; the IPFC-IMD system may not be quite as attractive due to additional cost, however, the IPFC-based system was highly preferable for the minimum input harmonics and maximum PF.

Acknowledgements

This work was supported by the Faculty Project Fund (260-01BK) from The Pennsylvania State University Berks Campus.

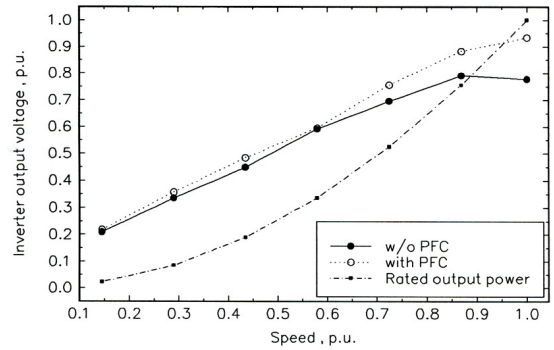

a) Inverter Output Voltage

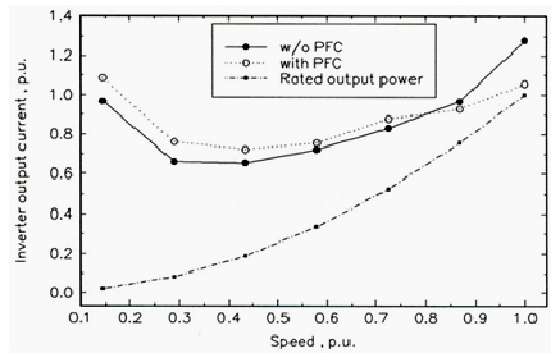

b) Inverter Output Current

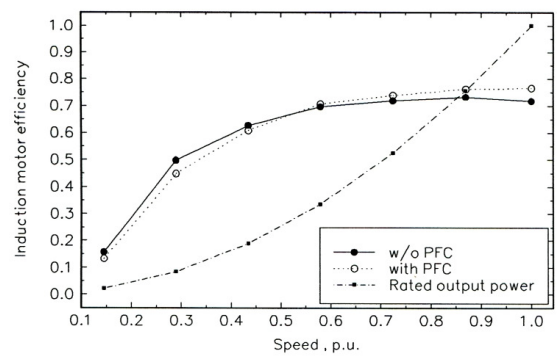

c) Induction Motor Efficiency

Figure 13. Inverter Output Voltage, Current, and Induction Motor Efficiency with and without IPFC for the IMD System with Friction Load

References

[1] Consoli, A., Gennaro, F., Scarcella, G., & Testa A. (2001). A Simple Unity Power Factor Motor Drive for Home Appliances. *Electric Power Components and Systems*, 29(4), 335-348.

[2] Basu, S., & Bollen, M. (2005, July). A Novel Common Power Factor Correction Scheme for Homes and

Offices. *IEEE Transactions on Power Delivery*, 20 (3), 2257-2263.

[3] Rynone, W. (2007, May). Is Power Factor Correction Justified in the Home? *Power Electronics Technology Magazine*, 36-41.

[4] Basu, S., & Bollen, M., (2005, July). A Novel Common Power Factor Correction Scheme for Homes and Offices. *IEEE Transactions on Power Delivery*, 20 (3), 2257-2263.

[5] Park, G., Kwon, K., & Kim, T. (2010, May). PFC Dual Boost Converter Based on Input Voltage Estimation for DC Inverter Air Conditioner. *Journal of Power Electronics*, 10(3), 293-299.

[6] Singh, B., & Singh S. (2010). Single-Phase Power Factor Controller Topologies for Permanent Magnet Brushless DC Motor Drives, *The Institution of Engineering and Technology (IET) Power Electronics*, 3 (2), 147-175.

[7] Gopalarathnam, T., & Toliyat, H. (2003, November). A New Topology for Unipolar Brushless DC Motor Drive with High Power Factor, *IEEE Transactions on Power Electronics*, 18(6), 1397-1404.

[8] Pellegrino, G., Armando, E., & Guglielmi, P. (2010, March). An Integral Battery Charger With Power Factor Correction for Electric Scooter, *IEEE Transactions on Power Electronics*, 25(3), 751-759.

[9] Cacciato, M., Consoli, A., Caro, S., & Testa, A. (2005, July/August). Using the DC-Bus Current to Improve the Power Factor in Low-cost Electric Drives, *IEEE Transactions on Industry Applications*, 41(4), 1084-1090.

[10] Aware, M., Tarnekar, S., & Kothari, A. (2000, September). Unity power factor and efficiency control of a voltage source inverter-fed variable –speed induction motor drive*, IEE Proceedings Electrical Power Application*, 147(5). 422-430.

[11] Chai, J., & Liaw C., (2009, March). Development of a Switched-Reluctance Motor Drive with PFC Front End, *IEEE Transactions on Energy Conversion*, 24 (1), 30-42.

[12] Chang, H., & Liaw C. (2009, September). Development of a Compact Switched-Reluctance Motor Drive for EV Propulsion with Voltage-Boosting and PFC Charging Capabilities, *IEEE Transactions on Vehicular Technology*, 58(7), 3198-3215.

[13] Suryawanshi, H., Kulwal, A., Chaudhari, M., & Borghate, V. (2008, April). High Power Factor Operation of a Three-Phase Rectifier for an Adjustable-Speed Drive, *IEEE Transactions on Industrial Electronics*, 55(4), 1637-1646.

[14] Reinert, J., & Schröder, S. (2002, February). Power-Factor Correction for Switched Reluctance Drives, *IEEE Transactions on Industrial Electronics*, 49(1), 54-57.

[15] Agilent Technologies. (2000). Compliance Testing to the IEC 1000-3-2 (EN 61000-3-2) and IEC 1000-3-3 (EN 61000-3-3), AN1273.

[16] Garcia, O., Jose A., Cobos, Prieto R., Alou P., & Uceda, J. (2003, May). Sinle Phase Power Factor Correction: A Survey, *IEEE Transactions on Power Electronics*, 18(3), 749-755.

[17] Singh, B., Singh, B., Chandra A., Al-Haddad K., Pandey A., & Kothari D. (2003, October) A Review of Single-Phase Improved Power Quality AC-DC Converters, *IEEE Transactions on Industrial Electronics*, 50(5), 962-981.

[18] Jovanović, M., & Jang, Y. (2005, June). State-of-the-Art, Single-Phase, Active Power-Factor-Correction Techniques for High-Power Applications – An Overview, *IEEE Transactions on Industrial Electronics*, 52(3), 701-708.

[19] Zhang, W., Feng G., Liu, Y., & Wu, B. (2004, November). A Digital Power Factor Correction (PFC) Control Strategy Optimized for DSP, *IEEE Transactions on Power Electronics*, 19(6), 1474-1485.

[20] Freescale. (2009, November). 3-Phase AC Induction Motor Control with PFC Using MC9S08MP16, *Design Reference Manual*, *DRM115, Rev. 0*.

[21] Todd, P. (1999). UC3854 Controlled Power Factor Correction Circuit Design, *U-134*, *Texas Instruments Incorporated*.

[22] Krishnan, R. (2001). *Electric Motor Drives – Modeling, Analysis, and Control*, Prentice Hall.

[23] Mohan, N. (2003). *Electric Drives an Integrative Approach*, MNPERE.

Biographies

DR. SHIYOUNG LEE is an Assistant Professor of Electrical Engineering Technology at The Pennsylvania State University, Berks Campus, Reading, PA. His primary research interest is the development of software configurable and full digital controllers for the three-phase permanent magnet brushless motor drives. Other research interests include, but are not limited to the following topics: efficient power converter topologies, wireless power transmission, input power factor correction, switched reluctance motor drives, LED lighting, alternative energy production, such as solar and wind power generation, and digital power processing for numerous industrial, medical and defense applications. He has published numerous papers through ASEE, IJAC, IEEE, and EMCW in the Power Electronics area. He is a Senior Member of IEEE and member of ASEE and IAJC. He can be reached at sul28@psu.edu.

HIGH-SPEED TWO-PHASE SRM FOR AN AIR-BLOWER DRIVE

Dong-Hee Lee, Kyungsung University; Hyunh Khac Minh Khoi, TOSY Robotics JSC; Jin-Woo Ahn, Kyungsung University

Abstract

In this study, the authors designed a high-speed, two-phase Switched Reluctance Motor (SRM) for an air blower. Considering high core loss at a maximum speed of 30,000 rpm for the proposed machine, a four-stator-pole two-rotor-pole (4/2) structure was chosen in order to reduce switching loss. Rotor pole shaping was employed because of a non-uniform air gap. Also, the rotor surface was optimally contoured in order to obtain constant torque and low torque ripple. The rotor pole arc had to be wide in such a way that torque ripple could be minimized during commutation. Iterative optimization using Finite Element Method (FEM) allowed the air gap to be designed for flat-top positive torque in phase excitation and small torque fluctuation during commutation. This SRM was designed with an asymmetric inductance profile where the positive region was wider than the negative one. The feasibility of the machine was verified by FEM and a prototype was built and installed in an air blower for experimental tests.

Introduction

Recently, there has been much interest in high-speed motor drives for practical applications to reduce system size while increasing efficiency. In particular, blowers, compressors, pumps, and spindle drives are suitable applications for the high-speed motor drives, and the demand for the high-speed motor system has greatly increased in the industrial market [1-4]. For practical systems, various electric machines, such as induction, permanent magnet, and switched reluctance motors, have been researched for application in high-speed systems [4-9].

SRM has a simple structure and inherent mechanical strength without rotor windings or permanent magnet. These mechanical structures are suitable for harsh environments and high-temperature and high-speed applications [4-12]. Raminosoa et al. [4] investigated a 6.5kW, 6/4 SRM with a speed rating of 14,000 rpm for a fuel-cell compressor. Also, an ultra-high-speed 6/4 SRM was introduced [5], where the practical results showed attainment of a speed of 150,000 rpm with a simple control scheme. That study used a 3-phase symmetric structure. An asymmetric staggered-gap type 4/2 SRM, with speeds up to 26,000 rpm, was also introduced [8-9]. In many speed drive systems, the number of poles is very important due to the electrical frequency and core losses. So, many high-speed drives use a two-pole system to reduce the electrical frequency. And, the number of phases is proportional to the drive cost [13-15]. Although the power losses are proportional to the switching frequency, the advance angle can introduce additional conduction and switching loss due to the excitation current building up without torque production; this advance area is proportional to the motor speed and phase numbers.

In this study, a 2-phase high-speed SRM was designed with continuous torque and self-starting characteristics. In order to reduce torque ripple, various types of rotor structure were analyzed. Additional non-linear air-gap structures were proposed based on the staggered-gap rotor type. The rotor pole shape provides a variable air gap according to rotor position, and it can produce a flat-top torque in a wide-torque region without torque dead-zone. In order to optimize torque ripple, the stator pole should have a cylindrical shape, but the shape of the rotor pole was designed by an iterative optimization process with FEM. The torque ripple, according to rotor position and air gap, was used as the optimal objective function. The final SRM had to have a non-uniform air gap and asymmetric inductance characteristic, which would yield wide positive and short negative torque regions. Such an SRM would be suitable for one-directional rotation due to its asymmetric inductance characteristic. The extended positive torque region can develop continuous torque with a torque overlap region and self-starting characteristics at any rotor position without torque dead-zone. And by optimizing the variable-air-gap structure, torque ripple can be reduced. In order to verify the performance of the proposed high-speed 4/2 SRM, computer simulations and experimental tests were employed.

Design of the Two-Phase 4/2 SRM

Conventional 4/2 SRM

The output torque, T_e , can be derived from the inductance, L , and phase current, i , as follows [1]:

$$T_e = \frac{1}{2} i^2 \frac{dL(\theta, i)}{d\theta} \tag{1}$$

where $L(\theta,i)$ is inductance and depends on both rotor position, θ , and phase current.

Figure 1 shows conventional and modified 4/2 SRMs. The modified types include a staggered-gap rotor pole surface type, air-teeth type, and air-hole rotor pole type [4], [13 -15]. Static torque profiles for those SRMs are compared in Figure 2, where the torque ripple is high, a zero-torque region is not avoidable, and torque for a motoring region is not enough in the conventional type.

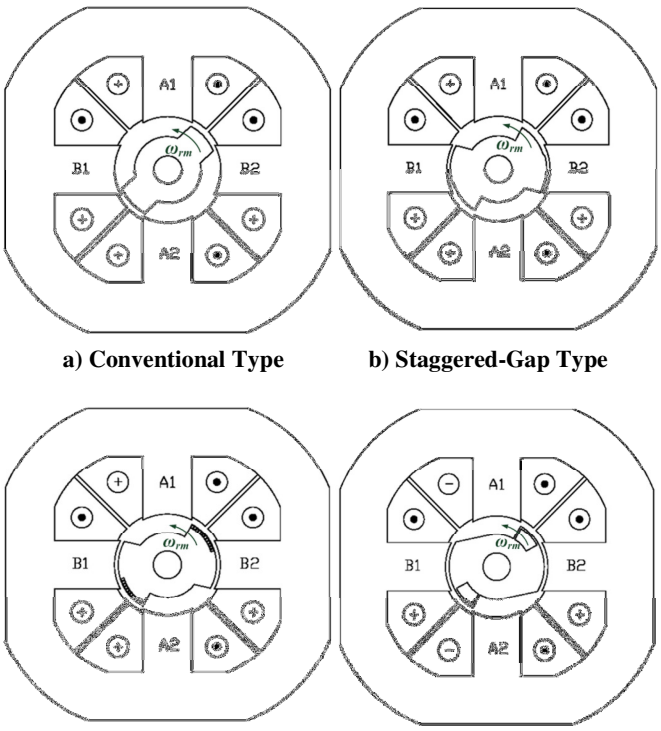

a) Conventional Type **b) Staggered-Gap Type**

c) Air-Teeth Type **d) Air-Hole Type**

Figure 1. Various 4/2 SRMs

On the other hand, the modified designs are suitable for self-starting at any rotor position, due to a wide positive torque region. However, even with the modifications of the rotor poles, the SRMs still experience a sudden rise in positive torque region. The reason for this is an air-gap change on the rotor pole surface. The torque ripple causes high vibration and acoustic noise. An elaborate rotor pole shaping has to be incorporated with the design process instead of using one step on the rotor pole contour in order to obtain as small a torque fluctuation as possible. Among the modified types, the air-teeth and air-hole types are not easy to manufacture and to optimize. So, the design process is based on the staggered-gap rotor type. And, the rotor pole contour is determined to reduce torque ripple.

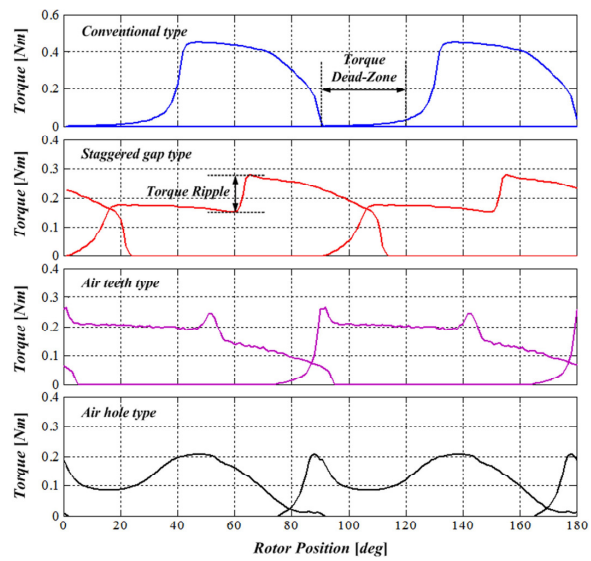

Figure 2. Static Torque Characteristics of Conventional, Staggered-Gap, Air-Teeth, and Air-Hole Types

Proposed 4/2 SRM

In order to obtain a wide positive torque region for stable self-starting, the rotor pole arc needs to be bigger than the stator pole pitch. Given this condition, the rotor pole surface must be optimally shaped, with respect to the rotor position, for mitigating torque ripple by means of an iterative method with FEM analysis.

Figure 3 illustrates the key design parameters in the determination of the rotor shape. The stator inner diameter (r_s) is determined to be constant. It can be seen that the rotor pole arc is wider than one stator pole pitch. One rotor pole is segmented into *n* nodes, with each segment having its own radius (r_k) and angular position (φ_k) in polar coordinates. Angle increment ($D\varphi$) is determined by two node numbers and the rotor pole arc. The length of the air gap at the *k*-th node is equal to the difference between r_s and r_k. Radius r_k changes within a limited boundary to achieve less torque oscillation. At the *k*-th node, radius r_k needs to be decreased in case the calculated torque is bigger than the desired one. Conversely, if the calculated torque is too small, the radius r_k is increased until the calculated torque reaches the target. It should be noted that the maximum possible value for radius r_k is limited by a critical dimension, which is the minimum air gap.

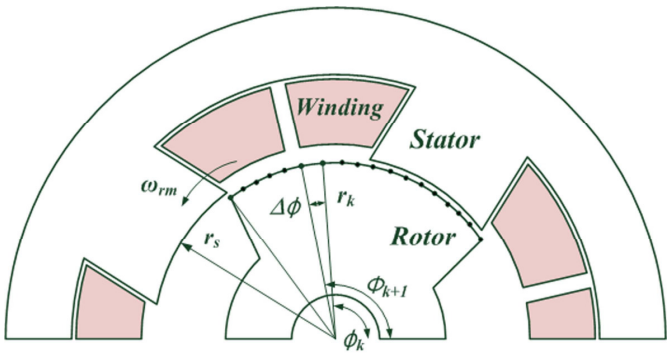

a) Initial Condition

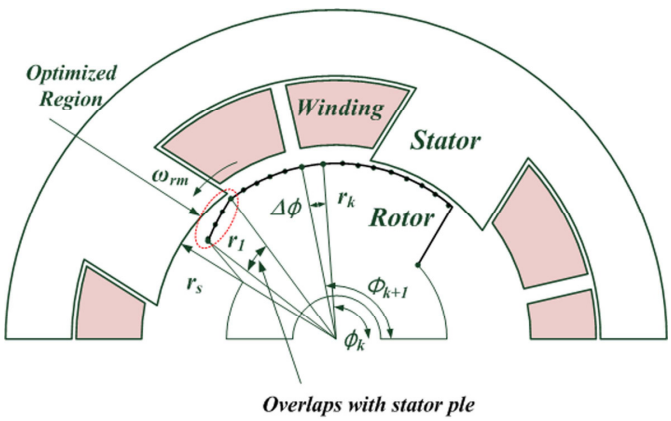

b) Optimization Process

Figure 3. Key Parameters in Rotor Shape Optimization

Figure 4 shows the step-by-step design algorithm of rotor pole shaping. The initial set of conditions is: minimum air gap, acceptable torque error T_{err} [%] as a percentage of average torque T_{avg}, a node number, and angle increment Dφ. In this study, the angle increment was one degree and the acceptable torque error was set to 2%. Rated torque was set at 0.2Nm for a 600W, 30,000 rpm high-speed air-blower system.

Figure 5 shows the flux distribution and density during optimization. The output torque was affected by both air-gap and fringing flux. In general, the amount of fringing flux—when the rotor was optimized at the *k*-th node—will change when the (*k*+1)-th node is being optimized. This means that optimization of subsequent nodes will change torques at previous nodes which were calculated in previous steps. However, air-gap flux dominates fringing flux. The fringing effect can be ignored. So, the nodes were considered to be independent of each other during the optimization process.

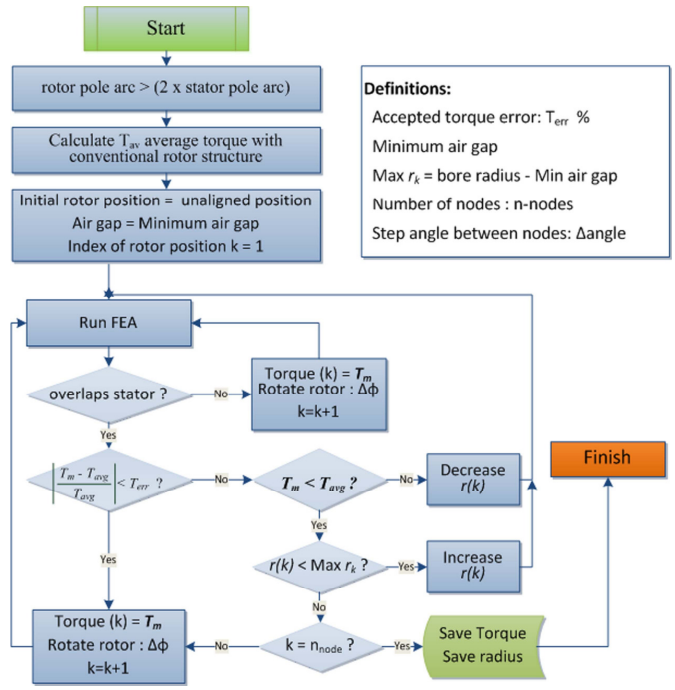

Figure 4. Flow Chart for Rotor Pole Optimization

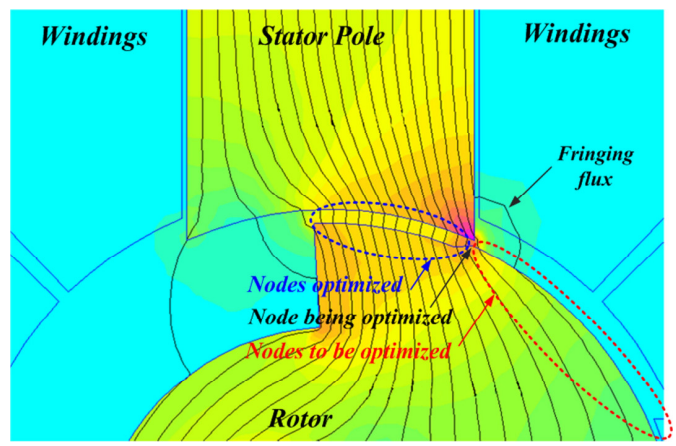

Figure 5. Flux Distribution During Optimization

Figure 6 shows the results of rotor pole shaping through the optimization procedure for the high-speed 4/2 SRM, and Table 1 shows the specifications of the motor.

Table 1. Specifications of the Proposed 4/2 SRM

Parameters	Value	Parameters	Value
Output power	600W	Average Torque	0.2Nm
Stator Poles	4	Rotor Poles	2
Bore Diameter	30mm	Stator Outer Dia	80mm
Stack Length	30mm	Air-gap	0.25mm
Stator Pole Arc	46°	Rotor Pole Arc	102°

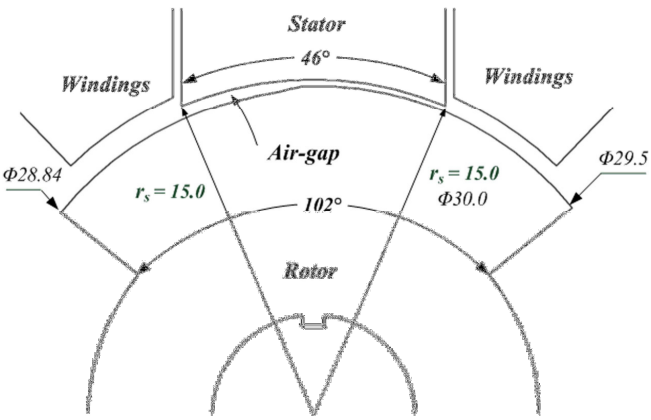

Figure 6. Optimized Rotor Pole Shape

Figure 7 shows the inductance and torque profiles of the prototype SRM analyzed by FEM. Table 1 shows the design sheet and specifications of the motor. The inductance is asymmetric and, hence, the machine can produce a wide positive torque region for continuous torque generation. In order to include the saturation effect of the steel, the design procedure was conducted at a current of 7A. As shown in Figure 7, the inductance profiles are almost linear in the low -current region, and the corresponding torque can be considered to be constant. However, in the high-current region, the torque is decreased at the middle of the rotor poles due to the steel saturation.

As seen in Figure 7b, FEM results show higher torque ripple than the target value in the middle position of the rotor. In the design process, the maximum torque ripple was set to 2% of the rated value. However, the analyzed maximum torque ripple was about 10%.

In Figure 8, static torque profiles of three 4/2 SRMs are compared. The structure of the conventional 4/2 SRM is shown in Figure 1a, with the modified type shown in Figure 1b. The motors being compared were redesigned with the same size and output power for the proposed application. The proposed SRM has lower torque ripple than conventional and modified 4/2 SRMs. In the proposed design, torque during commutation secures stable self-starting at any rotor position without torque dead-zone. The analyzed torque ripple was under 10% at the rated conditions. Due to the limit of the minimum air gap around the mid-point of the rotor pole, the analyzed torque ripple was higher than the desired one. As shown in Figure 6, the variable air gap converges to the minimum air gap to improve the output torque. So, the torque ripple around the mid-point of the rotor pole arc would be higher than the expected value. However, the proposed prototype SRM had much lower torque ripple than the modified SRM, which had more than 60% torque ripple at the rated conditions.

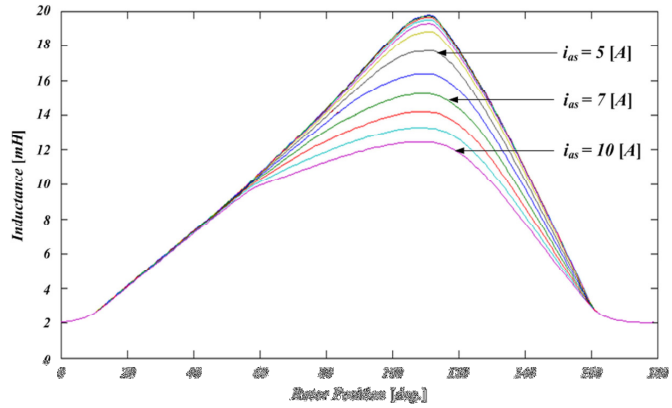

a) Inductance Profile of the Proposed SRM

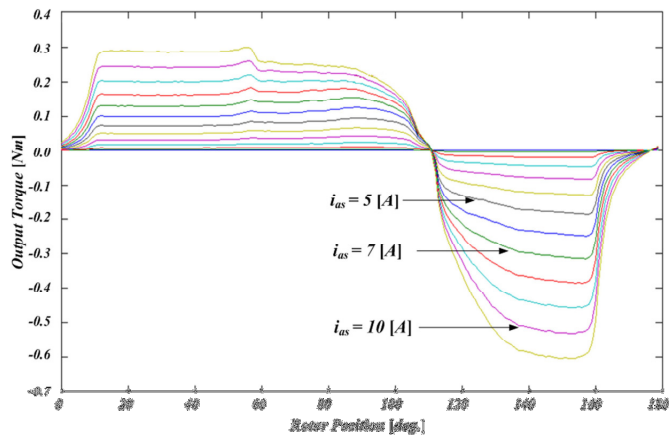

b) Torque Profile of the Proposed SRM

Figure 7. Inductance and Torque Characteristics of the Proposed 4/2 SRM

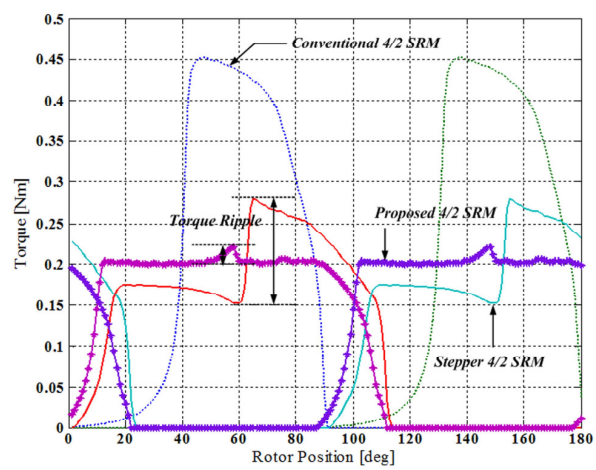

Figure 8. Torque Characteristics Comparison

Simulation and Experimental Results

In order to verify the performance of the proposed motor, dynamic simulation using Matlab was performed on the practical air-blower system. Figure 9 shows simulation results at the rated speed. In the simulation results, the proposed motor can operate well in the range of 15,000 to 30,000 rpm. Torque ripple during single-phase excitation was significantly small, but the ripple becomes high during commutation due to constant current control.

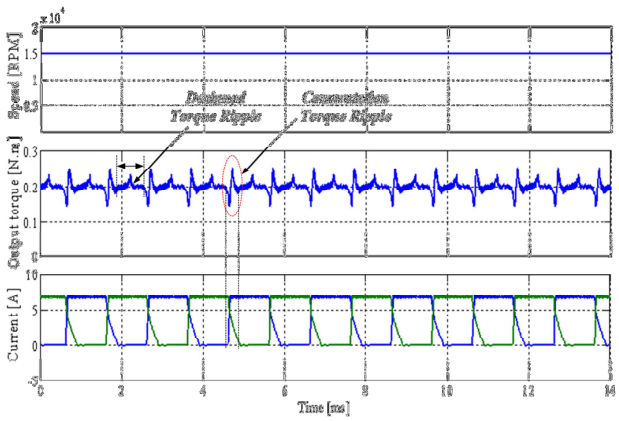

a) 15,000 rpm

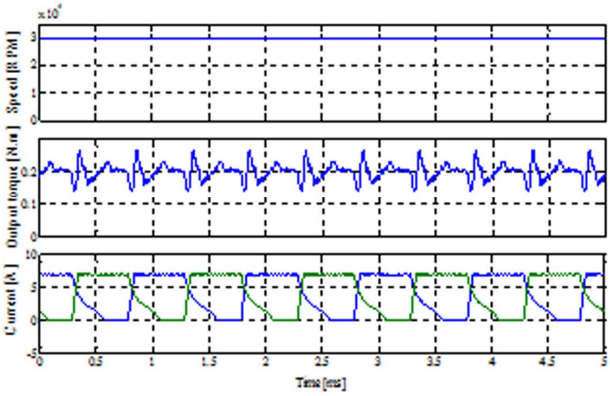

b) 30,000 rpm

Figure 9. Simulation Results at Rated Torque

Figure 10 shows a prototype motor including the rotor, stator, and motor assembly. Figure 11 shows the experimental configuration, including the motor assembly. A two-phase asymmetric converter and DSP (TMS320F-2811) were used for motor control. The asymmetric converter was designed with MOSFETs and power diodes that have 600V, 50A ratings. Current was detected by a mounted-chip type current sensor (ACS712) and embedded 12-bit ADC of the DSP.

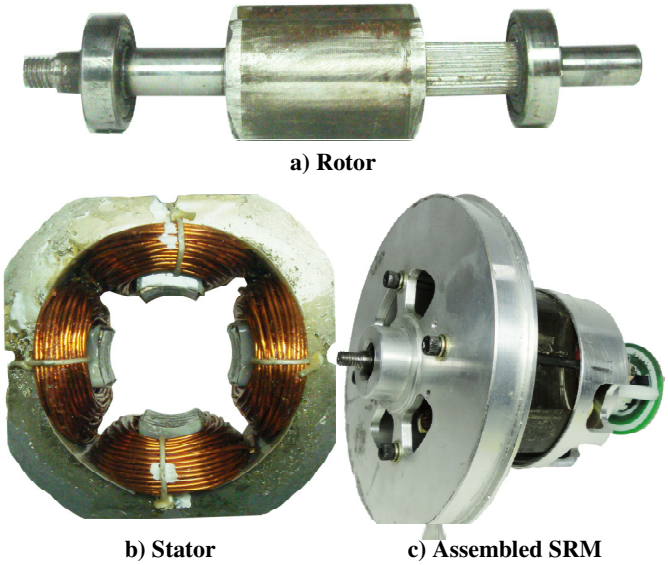

a) Rotor

b) Stator **c) Assembled SRM**

Figure 10. Prototype of 4/2 SRM

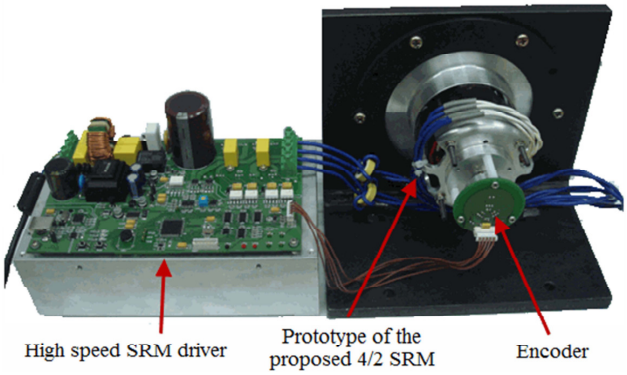

Figure 11. Experimental Configuration

Balanced, soft-chopping technology was used for the switching of the asymmetric converter to reduce the current ripple in the phase winding. There were 16 pulses per revolution from an ultra-fast photo-interrupter, and the signal was connected to the QEP module of the DSP. The motor controller can count 64 pulses per revolution with a phase detecting signal.

Figure 12 shows the measured torque characteristics of the proposed high-speed 4/2 SRM. The desired torque was the theoretically analyzed value. The SRM had higher torque ripple than expected. The reason for this was manufacturing error in the rotor and stator. From the practical measurements, the rotor diameter had 1% error. Furthermore, the assembly of the stator and bracket had distortion in the rotational direction. This distortion introduced a concentricity error between the stator and rotor assembly. For these reasons, the measured torque had some errors.

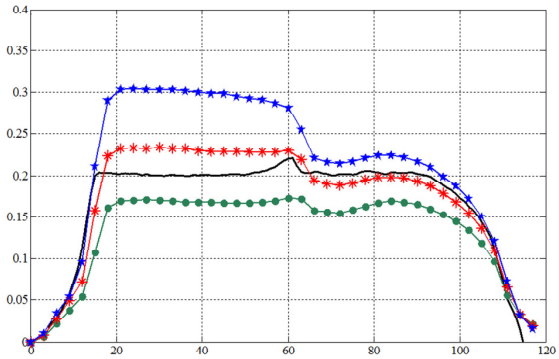

Figure 12. Measured Torque Characteristics

Figures 13 through 15 show the experimental results using the dynamometer. Figure 13 shows a no-load operation at 10,000 and 30,000 rpm. The proposed motor does a good job of tracking the reference speed. Radial vibration increased greatly in the high-speed region.

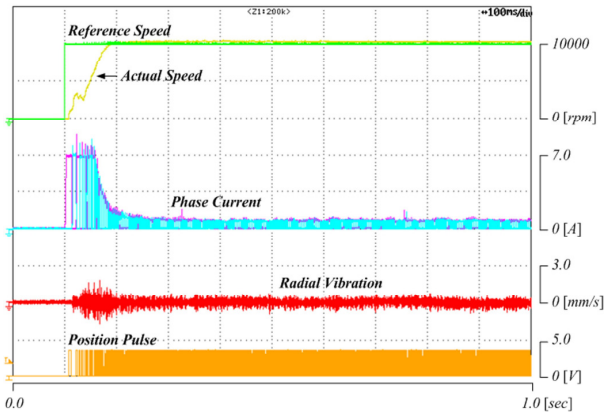

a) 10,000 rpm

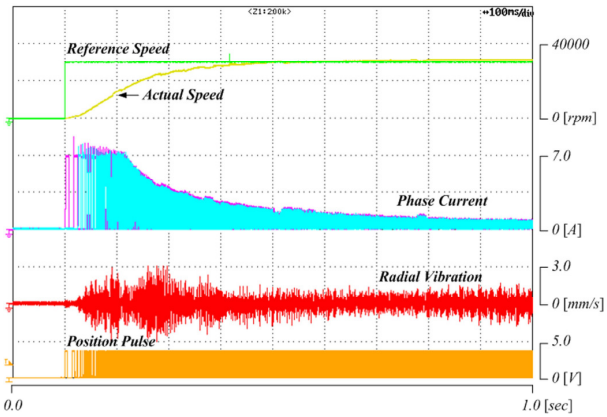

b) 30,000 rpm

Figure 13. Experimental Results under No-Load Operation

Figure 14 shows the experimental results according to the load variation at 10,000 and 30,000 rpm. As shown in the experimental results, the designed motor can operate quite well over a wide speed range.

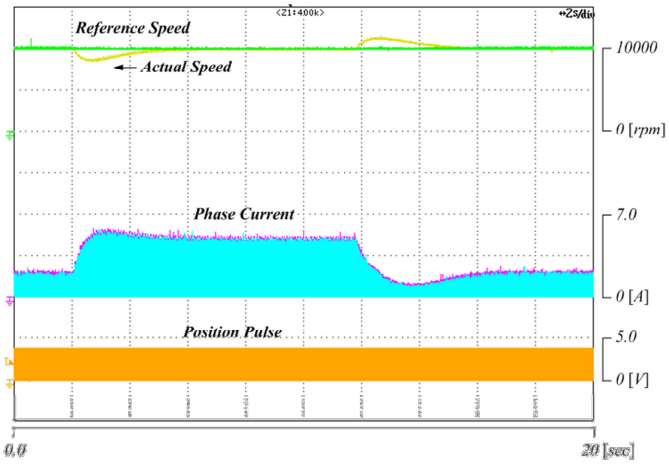

a) 10,000 rpm

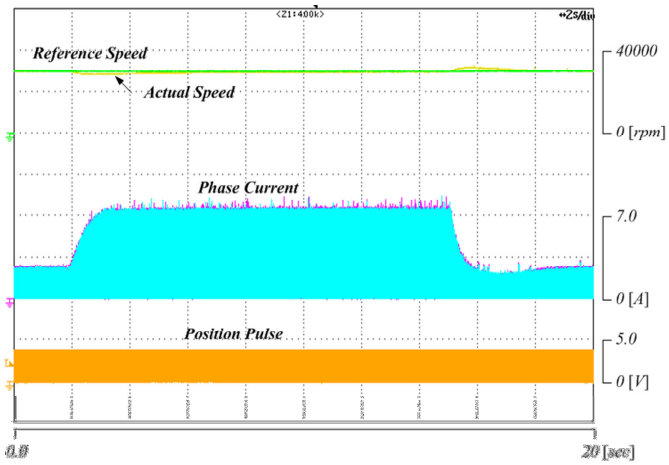

b) 30,000 rpm

Figure 14. Experimental Results with Load Variation

Figure 15 shows the experimental results of the designed motor used to drive a practical air blower. Impeller type 1 was used in the conventional design. The output air pressure was almost the same as that of a conventional air blower in which a universal motor would be installed, and the mechanical vibration and acoustic noise were lower than that of the conventional air blower.

Figure 16 shows the operating characteristics of an air-blower with the proposed SRM and impellers. As shown here, the Impeller Type 1 is for low-speed motors with high air pressure, while Impeller Type 2 is for high-speed motors with low air pressure.

Conclusion

This paper presents a study of a high-speed 4/2 SRM, where rotor pole shape was optimized for torque ripple reduction. The outer dimensions were the same as those of a conventional air-blower motor. In order to guarantee continuous torque at any rotor position, the positive torque region had to be extended by an asymmetric inductance profile of the motor. That is possible because the blower rotates in one direction. The rotor pole shaping was carried out by an iterative optimization procedure using FEM. The proposed motor was verified in terms of the capability of wide speed operation by air-blower tests in which it demonstrated high-efficiency and low-vibration characteristics.

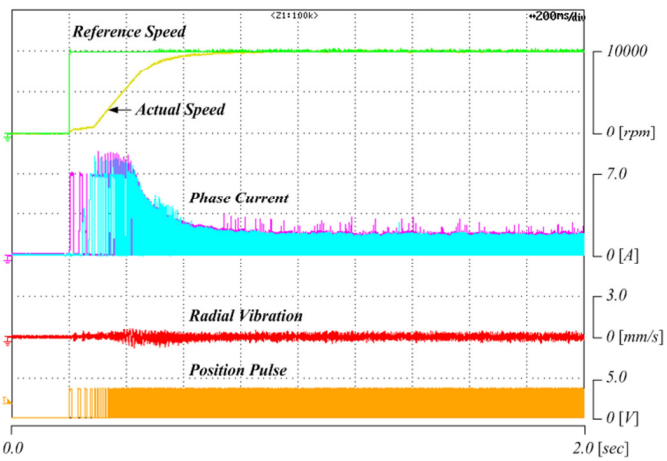

a) 10,000 rpm

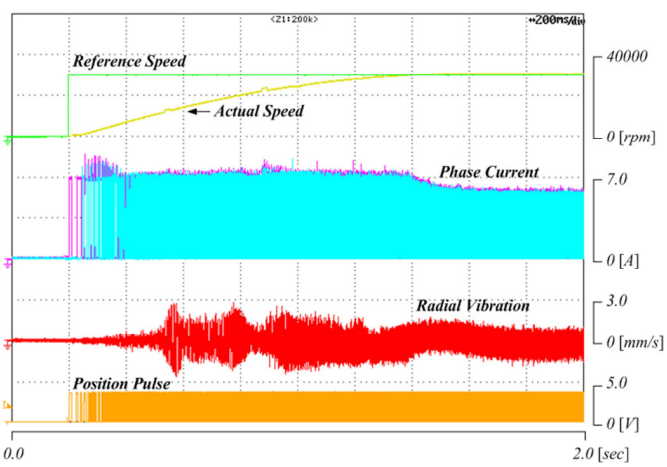

b) 30,000 rpm

Figure 15. Experimental Results with a Practical Air-Blower

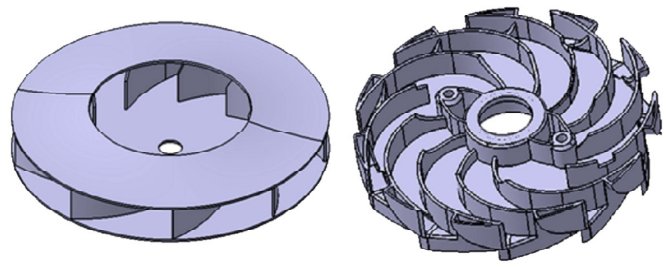

a) Impeller Type 1

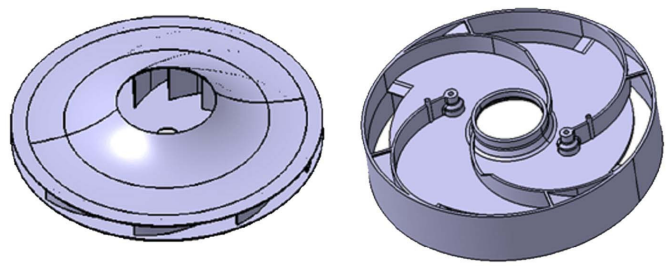

b) Impeller Type 2

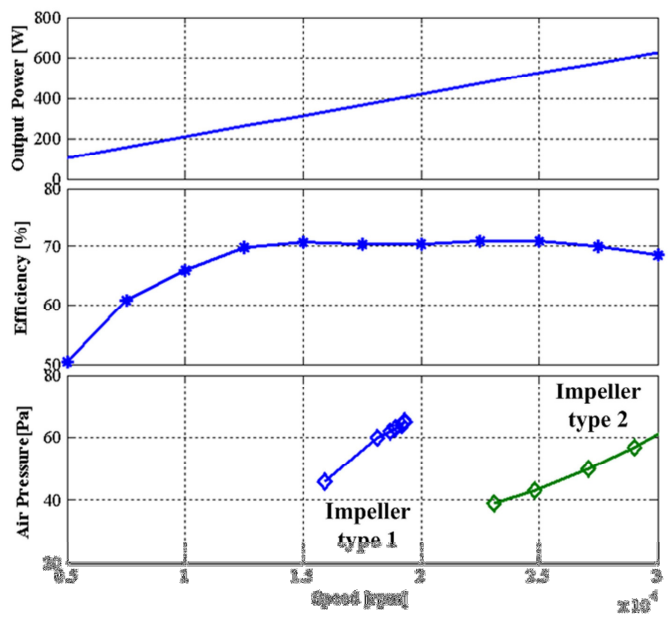

c) Measured Power, Efficiency, and Air Pressure

Figure 16. Operating Characteristics of Air-Blower with Proposed SRM

Acknowledgements

This work was supported by Energy Resource R&D program (2009T100100654) under the Ministry of Knowledge Economy, Republic of Korea.

References

[1] Krishnan, R. (2001). *Switched Reluctance Motor Drives: Modeling, Simulation, Analysis, Design, and Application*. CRC Press.

[2] Bianchi, N., Bolognani, S., & Luise, F. (2006) High speed drive using a slotless PM motor. *IEEE Transaction on Power Electronics*, 21(4), 1083-1090.

[3] Hanoun, H., Hilairet, M., & Marchand, C. (2010). Design of an SRM Speed Control Strategy for a Wide Range of Operating Speeds. *IEEE Transaction on Industrial Electronics*, 57(9), 2911-2921.

[4] Raminosoa, T., Blunier, B., Fodorean, D., & Miraoui, A. (2010). Design and Optimization of a Switched Reluctance Motor Driving a Compressor for a PEM Fuel-Cell System for Automotive Applications. *IEEE Transaction on Industrial Electronics,* 57(9), 2988-2997.

[5] Kozuka, S., Tanabe, N., Asama, J., & Chiba, A. (2008). *Basic characteristics of 150,000r/min switched reluctance motor drive*. Power and Energy Society General Meeting - Conversion and Delivery of Electrical Energy in the 21st Century, (pp. 1-4).

[6] Mademlis, C., & Kioskeridis, I. (2010). Gain-Scheduling Regulator for High-Performance Position Control of Switched Reluctance Motor Drives. *IEEE Transaction on Industrial Electronics*, 57(9), 2932-2938.

[7] Kajiwara, K., Kim, Y. J., & Dohmeki, H. (2007). Analysis of the maximizing start torque of Switched Reluctance Motor for super high speed drive. *Proceedings of the ICEMS 2007,* (pp. 1428-1432).

[8] Genda, T., & Dohmeki, H. (2009). Characteristics of 4/2 Switched Reluctance Motor for a high speed drive by the excitation angle. *Proceedings of the ICEMS 2009*, (pp. 1-6).

[9] Kartono, I. R., Kajiwara, K., & Dohmeki, H. (2008). Dynamic simulation of maximizing the starting torque for super-high-speed drive of a 4/2 Switched Reluctance Motor. *Proceedings of ICEM 2008,* (pp. 1 -6).

[10] Ahn, J. W., Kim, T. H., & Lee, D. H. (2005). Performance of SRM for LSEV. *Journal of Power Electronics*, 5(1), 45-54.

[11] Lee, D. H., Lee, Z. G., Liang, J., & Ahn, J. W. (2007). Single-Phase SRM Drive With Torque Ripple Reduction and Power Factor Correction. *IEEE Transaction on Industry Applications*, 43(6), 1578-1587.

[12] Ohyama, K., Naguib, M., Nashed, F., Fujii, K., & Uehara, H. (2006). Design using finite element analysis of a switched reluctance motor for electric vehicle. *Journal of Power Electronics*, 6(2), 163-171.

[13] Faiz, J., Finch, J. W., & Metwally, H. M. B. (1995). A novel switched reluctance motor with multiple teeth per stator pole and comparison of such motors. *Electric Power Systems Research*, 34, 197-203.

[14] Kano, Y., Kosaka, T., & Matsui, N. (2010). Optimum Design Approach for a Two-Phase Switched Reluctance Compressor Drive. *IEEE Transaction on Industry Applications*, 46(3), 955-964.

[15] Oh, S. G., & Krishnan, R. (2006). Two Phase SRM with Flux Reversal Free Stator: Concept, Analysis, Design and Experimental Verification. *Conference Record of The 2006 IEEE Industry Applications Conference 41st IAS Annual Meeting,* (pp. 1155-1162).

Biographies

DONG-HEE LEE received his B.S., M.S. and Ph.D. in Electrical Engineering from Pusan National University, Pusan, Korea, in 1996, 1998 and 2001, respectively. He worked as a Senior Researcher in the Servo R&D Team at OTIS-LG, from 2002 to 2005. He has been with Kyungsung University, Busan, Korea, as an Associate Professor in the Department of Mechatronics Engineering since 2005. He is visiting professor of University of Wisconsin (WEMPEC) in 2012. His current research interests include Power Electronics and motor control systems. His email address is leedh@ks.ac.kr

HUYNH KHAC MINH KHOI received his B.S. in Electrical Engineering from the University of Technology, Ho Chi Minh City, Vietnam, in 2007 and his M.S. in Electrical Engineering from Kyungsung University, Busan, Korea, in 2010. Since 2010, he has been with the Electronics Department, TOSY Robotics JSC., Hanoi, Vietnam where he is currently a R&D Engineer. His current research interests include the design and advanced control of electrical machines, and power electronics.

JIN-WOO AHN received his B.S., M.S. and Ph.D. in Electrical Engineering from Pusan National University, Busan, Korea, in 1984, 1986, and 1992, respectively. He has been with Kyungsung University, Busan, Korea, as a Professor in the Department of Mechatronics Engineering since 1992. He was a Visiting Researcher in the Speed Lab at Glasgow University, U.K., a Visiting Professor in the Dept. of ECE and WEMPEC at the University of Wisconsin-Madison, USA, and a Visiting Professor in the Dept. of ECE at Virginia Tech, from 2006 to 2007. He is the author of five books including SRM, the author of more than 120 papers and has several patents. His current research interests include advanced motor drive systems and electric vehicle drives.

DESIGNING SUSTAINABLE HYBRID HIGH-BRIGHTNESS LED ILLUMINATION SYSTEMS

Akram A. Abu-aisheh, University of Hartford, West Harford

Abstract

In this paper, the author presents a road map for the design and development of sustainable hybrid High-Brightness Light Emitting Diode (HB LED) illumination systems controlled by a Field Programmable Gate Array (FPGA). The proposed hybrid system design represents the foundation for future sustainable high-efficiency illumination systems. The system design presented here individually controls an array of HB LEDs. Each HB LED operates in a different mode defined by the user. Photovoltaic (PV) panels were used as the primary source of energy in this hybrid system, while the electric grid was used as a backup source to supply power to the HB LEDs only when the PV system could not sufficiently power all of the system HB LEDs, and when the PV system batteries would be depleted below the minimum level set in the system design.

The hybrid illumination system design presented here is an important link between the current AC-based illumination systems and future sustainable DC-based solar illumination systems. Since computer simulation is an important tool for future illumination system design and analysis, it was used here to assist designers in analyzing different designs and in optimizing the one to be implemented.

Introduction

The demands for utilizing alternative power sources have increased due to rising oil prices and more stringent environmental regulations. Alternative energy and its applications have been heavily studied for the last decade, and solar energy is the preferred choice in many applications. Among solar energy applications [1], photovoltaic (PV) technology has received much attention and is being used in many applications [2], [3].

Presented here is a plan for the design of a sustainable hybrid FPGA-controlled high-brightness LED illumination system that can be used to replace current illumination systems in order to improve system efficiency and reliability. In the proposed system, a single-ended primary-inductor converter (SEPIC) DC-DC converter is used to deliver solar energy via PV-cell modules to a battery bank in charging mode during the daytime. At night, it drives an LED lighting system. An FPGA is used to individually control an array of LEDs. The main reason for choosing HB LEDs as the illumination source in this system is due to their high efficiency as compared with incandescent and fluorescent lamps.

Hybrid HB LED Illumination

The principal motivation for this hybrid system is the clear shift to DC systems with more use of alternative energy sources. The AC vs. DC battle raged when Edison promoted DC power while George Westinghouse felt that AC was the way to go. AC won the battle, since it was so much easier to step the voltage up and down using transformers, and higher voltages greatly reduce resistive loss. This study explored the continued growth of DC power distribution in buildings, for which LED-based illumination has been a major driver.

Since photovoltaic panels are used to power the illumination system, there is a need for a second source of power for the system when the sun is out for a period of time beyond the capability of the batteries to serve as a backup source. Some products that are appearing on the market use HB LEDs with built-in converter that can be connected directly to the AC line. Those products take advantage of the high efficiency of HB LEDs, but they do not use a sustainable source as the main supply for those LEDs.

The hybrid HB LED-based illumination system design presented here incorporates an automatic transfer switch, as shown in Figure 1. Through the use of this switch, the hybrid system uses solar as the primary source of energy, and it switches to the AC line only for the time when the primary source cannot supply the required power to the illumination system.

In the system of Figure 1, LEDs are powered by the solar panel during the daytime as the primary source, with the battery in charge mode, and by the battery at night. If the battery is fully discharged, the HB LED system operates from the AC line as the secondary source. The design of DC -DC converters, DC-AC rectifiers, and DC-AC inverters are well understood and can be followed using senior-level or graduate power electronics textbooks [4-7].

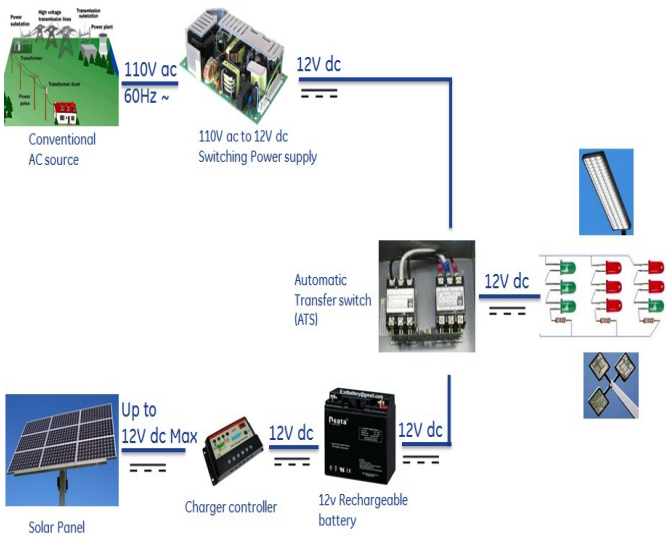

Figure 1. Hybrid High Brightness LED Illumination System

Since LEDs can handle voltage fluctuations, the system can be simplified by using a full-wave bridge rectifier instead of the AC-DC converter. The simplified system is shown in Figure 2, where the DC distribution to power HID LED lamps consists of a solar panel, DC supply distribution, DC supply switching module, battery charger controller, battery bank, DC–DC Converter (Buck-Boost converter), and HID LED lamps. The operation of this buck-boost converter has two operation modes: the first is the buck mode for daytime battery charging operation, and the second is the boost mode for nighttime lighting usage.

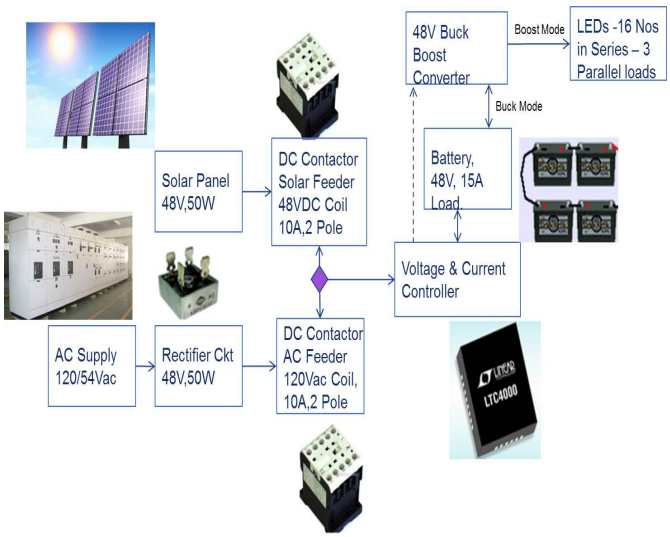

Figure 2. Simplified Hybrid LED Illumination System

The hybrid illumination system presented in Figure 2 is sustainable for many applications that are emerging due to the continued growth of DC power distribution in buildings. The principal force behind this growth is LED-based illumination which was cited as one major driver. The main challenges in building such a system include: the analysis of switching circuits that deal with switching of power between AC and DC distribution; being fed from solar panels; and, switching between the two sources. Figure 3 presents one solution for this problem, where an AC contactor and a DC contactor with mechanical interlock are used; and Figure 4 which presents the relay control for the mechanically interlocked contactors.

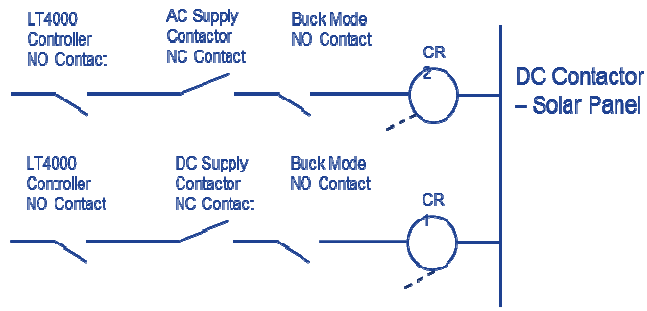

Figure 3. AC and DC Contactors Design to Control the LED Illumination System Switching

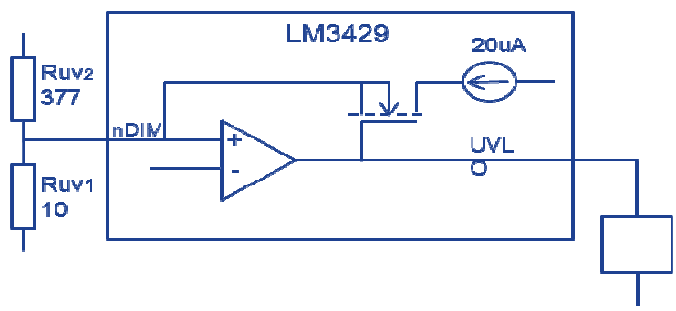

Figure 4. Relay Design to Control the Hybrid Illumination System Switching

The illumination system is designed to be used to individually control an array of HB LEDs. Each HB LED operates in a different mode that is independently defined by the user. The defined sequence of LED illumination is controlled using a controller circuit, i.e. an FPGA. Figure 5 presents the basic control system layout used for this DC illumination control strategy that gives the user more flexibility and control than the flexibility and control level available for standard AC-powered illumination used in incandescent or fluorescent lamps.

In this LED control strategy, an FPGA is used to individually control the LEDs. The FPGA is programmed using Hardware Description Language (HDL). In this case, VHDL is used. [VHDL is a hardware description language

used in electronic design automation to describe digital and mixed systems and integrated circuits.] The pattern of the LEDs defined by the user can be modified using this hardware description language. A Basys Spartan 2 FPGA was chosen for this application due to its flexibility, low cost, and ease of use.

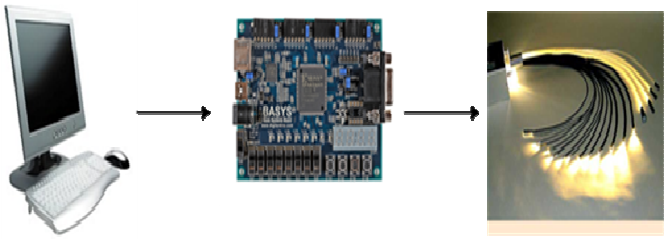

Figure 5. FPGA-Controlled Illumination

The application software used in this study was Adept, which is a powerful program that allows configuration and data transfer with Xilinx logic devices, and can be used as an interface between Xilinx and the Spartan 2 FPGA board. For maximum intensity from the LEDs, the typical forward voltage of 3.9V, with a forward current 700mA, is supplied to the FPGA. A personal computer provided with Xilinx software was used for programming the sequence of the LEDs defined by the user. The programming was done using VHDL. The developed software was tested using a Digilent FPGA board.

High brightness LEDs [8], [9] can be driven at currents from hundreds of mA to more than an ampere, compared with the tens of mA for other LEDs; however, few of the HB LEDs can produce over a thousand lumens. Since overheating is destructive, the HB LEDs may need to be mounted on a heat sink to allow for heat dissipation. If the heat from an HB LED is not removed using a heat sink, the device will burn out in seconds.

A single HB LED can often replace an incandescent bulb in a torch, or be set in an array to form a powerful HB LED system. LEDs can operate on AC power without the need for a DC converter. Each half-cycle part of the LED emits light, while the other part is dark, a pattern that is reversed during the next half cycle. The efficacy of this type of HB LED is typically around 40 LM/W. A large number of LED elements in series may be able to operate directly from line voltage. In 2009, Seoul Semiconductor released a high-DC-voltage LED capable of being driven from AC power with a simple controlling circuit. The low power dissipation of these LEDs gives them more flexibility than the original AC LED design. In this project, the HB LEDs were powered from a DC source.

To control the LED from the FPGA, a circuit driver was needed to boost the power of the FPGA output. An LED driver circuit is an electric power circuit used to power a light-emitting diode or LED. The circuit consists of a voltage source powering a current-limiting resistor and an LED connected in series. The HB LEDs used in this project design had a constant current of 700mA and a supply voltage of +3V. As the current has to be amplified to 700mA for each LED, two transistors were connected together so that the current amplified by the first is amplified further by the second transistor. The overall current gain is equal to the two individual gains multiplied together, i.e., $h_{FE} = h_{FE1} \times h_{FE2}$, where h_{FE1} and h_{FE2} are the gains of the individual transistors. An LED driver circuit for each individually controlled LED is given in Figure 6.

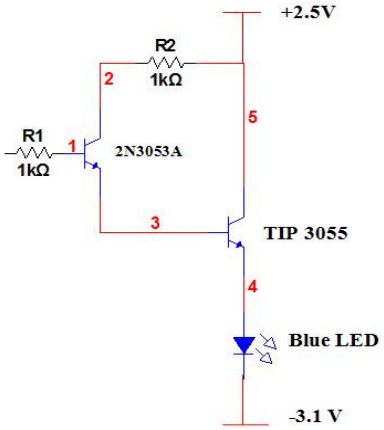

Figure 6. LED Driver circuit

Sustainable PV-Powered Illumination

Since photovoltaic panels are used to power the HB LED illumination systems, there is a need for the development of the DC converter system to power the LEDs. To satisfy this requirement, a forward converter with PV-based LED applied in lighting systems was used. In the proposed DC supply system, SEPIC was used to deliver solar energy via PV-cell modules to a battery bank in the charging mode during the daytime. During the nighttime, the converter (see Figure 7) drives an LED lighting system.

Figure 7 illustrates the principle PV-SEPIC-LED circuit applied in street illumination, where the produced PV voltage is stored in a battery bank throughout the charging unit during the daytime; at night, the discharger activates and the LEDs are energized with appropriate voltage through a step-up transformer and full bridge rectifier.

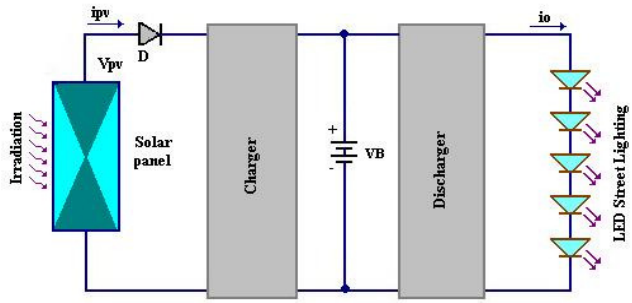

Figure 7. PV-based Sustainable Illumination

SEPIC circuits find widespread application when the input voltage fluctuates above and below an average value, while the output voltage must be kept at a constant value with minimum tolerances. One of the most applications of a SEPIC circuit is in integration with the photovoltaic system (PV system) and illumination load of series- and parallel-connected LEDs.

The SEPIC converter is a DC/DC converter topology that provides a positive regulated output voltage from an input voltage that varies above and below the output voltage. This type of topology is needed when the voltage from an unregulated input power source—such as solar, where the sun irradiation, temperature and weather change—directly affects the generated output voltage. Standard SEPIC topology [10], [11] requires two inductors in additional to a step-up transformer, making the power-supply footprint quite large. Photovoltaic (PV) cells are used to convert sunlight into electrical energy. On the other hand, it is also an important issue to save the energy demand and increase the energy efficiency [12-14]. High-brightness light-emitting diodes (LEDs) [15], [16] are becoming more widespread for lighting applications such as automobile safety and signal lights, traffic signals, street lighting, and so on.

In lighting applications with solar energy, the charger is adopted to convert solar irradiation for storage in the battery during the daytime. In the nighttime, a discharger is used to release energy from the battery and drive the LED lighting system. Low-power DC-DC converters can be used for the charger and discharger modes. So, since the PV voltage from the solar panel is unstable, the buck-boost converter is more suitable for charger circuits. This converter can also be used in the discharger circuit.

DC-DC Converter Control Design and Analysis using Computer Simulation

Computer simulation is an important tool for future illumination systems design. The HB LED-based illumination system was simulated using a circuit simulation program. In this section, the DC-DC converter control loop simulation results are presented. The most common control method, shown in Figure 8, is pulse-width modulation (PWM). This method takes a sample of the output voltage and subtracts it from a reference voltage to establish a small error signal (V_{ERROR}). This error signal is compared to an oscillator ramp signal. The comparator is used to generate a digital output (PWM) that controls the power switch.

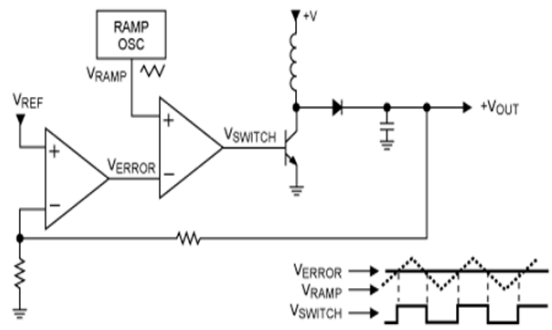

Figure 8. PWM controller for Switching Buck Controller

When the circuit output voltage changes, V_{ERROR} also changes causing the comparator threshold to change. Consequently, the PWM also changes. This duty cycle change then moves the output voltage to reduce the error signal to zero, thus completing the control loop.

The output voltage of the solar panels is stepped down using a buck, step-down converter. The closed-loop control circuitry for the buck converter consists of an Error Amplifier (ERR), oscillator, and PWM circuits. The ERR and oscillator outputs drive the PWM circuit. The EER circuitry is given in Figure 9, where the automatic control measures how close V_{OUT} is to V_{REF}.

The measurement of error is the Error Voltage, which is the difference between V_{OUT} and V_{REF}, Error Voltage = (V_{REF} - V_{OUT}). Since $\mathbf{V_{OUT} \sim V_{REF}}$, Error Voltage is close to zero, which means that this circuit maintains the Error Voltage and the PWM duty cycle, regardless of variations in the input voltage. If $\mathbf{V_{OUT} > V_{REF}}$, then the Error Voltage is negative, thereby decreasing the Error Voltage and the PWM duty cycle. If $\mathbf{V_{OUT} < V_{REF}}$, then the Error Voltage is

positive, which increases the Error Voltage and the PWM duty cycle. The oscillator circuit, given in Figure 10, is used to generate the ramp signal used as an input to the PWM circuit.

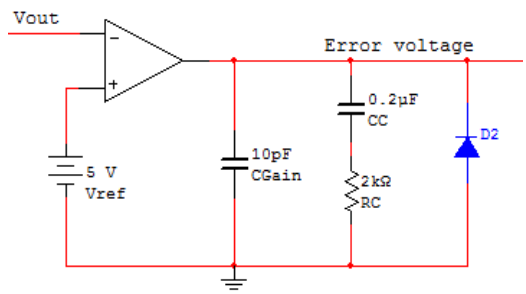

Figure 9. Error Amplifier Circuit

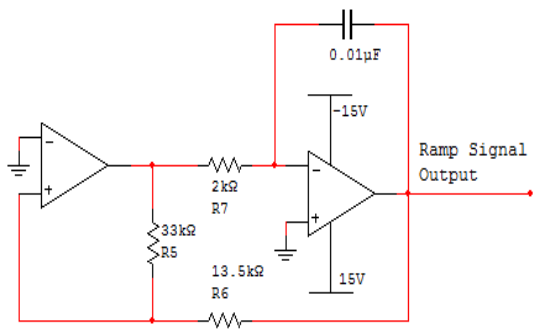

Figure 10. Oscillator Circuit

The PWM comparator circuit, given in Figure 11, compares the Error Voltage, generated by the ERR amplifier circuit, to an oscillator ramp signal which in turn is generated by the oscillator circuit. This comparator produces a digital output (PWM OUT) that drives the MOSFET.

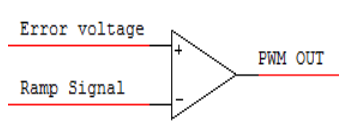

Figure 11. PWM Comparator Circuit

When a DC-DC converter circuit output voltage, Vout, changes, the Error Voltage also changes, thereby causing the comparator threshold to change. Consequently, the PWM OUT also changes.

Conclusion

A sustainable hybrid FPGA-controlled HB LED-based illumination system was developed and tested. This illumination system can be used for many lighting applications since it is more efficient and more reliable than existing traditional lighting systems based on incandescent or fluorescent lamps. The initial cost of the system due to the high cost of solar panels is the main disadvantage in the new design when compared with current illumination systems. While the use of the solar panels and HB LEDs adds to the initial cost of the system, the use of the solar panel will result in energy savings, and the use of HB LEDSs will be paid off in the long term due to their higher reliability, flexible control, and long life time.

References

[1] Steeby, D. L. (2012). *Alternative Energy Sources and Systems*. Delmar Cengage Learning.

[2] Kessell, T. (2011). *Introduction to Solar Principles*. Pearson Education, Inc.

[3] Gevorkian, P. (2011). *Large-Scale Solar Power System Design*. Mc Graw Hill Higher Education.

[4] Batarseh, I. (2004). *Power Electronic Circuits*. John Wiley and Sons, Inc.

[5] Rashid, M. H. (2004). *Power Electronics Circuits Devices and Applications*. Pearson Education, Inc.

[6] Hart, D. W. (2010). *Power Electronics*. McGraw Hill Higher Education.

[7] Mohan, N., Undeland, T. M., & Robbins, W. P. (2003). *Power Electronics Converters Applications and Design*. John Wiley and Sons, Inc.

[8] Kingbright. Retrieved October 28, 2011, from http://www.kingbrightusa.com/default.as

[9] Lumex. Retrieved October 30, 2011, from http://www.lumex.com/marketingdownload

[10] Fallin, J. (2008). Designing DC/DC converters based on SEPIC topology. *Analog Applications Journal*, 4Q, 18-23. Texas Instruments, Inc.

[11] Lin, B. R., & Huang, C. L. (2009). Analysis and implementation of an integrated SEPIC-forward converter for photovoltaic-based light emitting diode lighting. *IET Power Electronics*, 2(6), 635-645.

[12] Hodge, B. K. (2010). *Alternative Energy Systems & applications*. John Willey & Sons, Inc.

[13] Chuang, Y. C., & Ke, Y. L. (2008). *High efficiency battery charger with a Buck zero-current switching pulse width modulated converter*. Industrial and Commercial Power Systems Technical Conference, (pp. 433-444).

[14] Jovcic, D. (2009). Step-up DC-DC converter for megawatt size applications. *IET Power Electronics*, 2 (6), 675-685.

[15] Redley, R. (2006, November). Analyzying the Sepic converters. *Power System Design Europe*, (pp.14-18).

[16] Bisogno, F. E., Nittayarumphong, S., Radecker, M., & Doprado, R.N. (2006). A line power-supply for LED lighting using piezoelectric transformers in class-E topology. *Proceedings of the Power Electronics and Motion Control Conference IEEE IPEMC'06*, 2, 1-5.

Biography

AKRAM ABU-AISHEH is an Associate Professor of Electrical and Computer Engineering at the University of Hartford where he has served as the assistant chair of the Electrical and Computer Engineering Department and director of the electronic and computer engineering technology program for two years. Dr. Abu-aisheh has a doctorate in Optical Communications from the Florida Institute of Technology and Master of Science and Bachelor of Science degrees in Electrical Engineering from the University of Florida. His research interests include Fiber Optic Communications, Solar Energy, Power Electronics, and Engineering Education. He has published a book, a book chapter, and several international journals and conference papers. Dr. Abu-aisheh may be contacted at abuaisheh@hartford.edu

EXPERIMENTAL EVALUATION OF A BIO-BASED CUTTING FLUID USING MULTIPLE MACHINING CHARACTERISTICS

Julie Z. Zhang, P.N. Rao, & Mary Eckman, University of Northern Iowa

Abstract

In this paper, the authors present a study that was conducted in an undergraduate research program using experimental tests to evaluate the effectiveness of a soybean-based cutting fluid applied in CNC turning operations. Using two machining performance characteristics, namely surface roughness and tool wear, the study tested the effects of a soybean-based cutting fluid on improving surface finish and reducing tool wear compared to a petroleum-based cutting fluid when high-carbon alloy steel was machined. A statistical analysis of the data indicated that the bio-based cutting fluid performed as well as the petroleum product in terms of surface finish, and significantly better than the petroleum-based cutting fluid in terms of controlling tool wear. These positive test results may provide supporting evidence to manufacturing professionals for making strategic machining decisions regarding the choice of cutting fluids.

Introduction and Literature Review

Cutting fluids are used extensively in metal machining processes to remove and reduce heat during machining operations. On one hand, the use of cutting fluids greatly enhances machining quality while simultaneously reducing the cost of machining by extending tool life [1]. The use of petroleum-based cutting fluids, however, has been found to affect operators, causing medical problems such as dermatitis, while the disposal of the fluids needs to follow special provisions to take care of the environmental impact. With pressure from global climate change, environmental protection, natural resource limitation and governmental regulations, green manufacturing is gradually becoming a philosophy [2], [3]. The cost of machining, environmental impact, and operators' health concerns have driven researchers to find equivalent dry-cutting conditions that could satisfy machining requirements without the use of cutting fluids [4], [5]. Because of the very nature of machining processes, studies conducted by Diniz & Oliveira [4] and Khan & Dhar [5] concluded that machining under wet conditions was still better for tool life, and dry cutting would be of limited use in cases where the depth of cut is shallow.

There are a large number of cutting fluids that have been developed and formulated from organic and inorganic materials. Although cutting fluids are generally useful, their effectiveness in a given application may vary due to workpiece material and tool material properties, along with different machining conditions and whether a cooling or lubricating mechanism is predominant. The majority of the existing cutting fluids are petroleum-based products, which are hazardous for storage and disposal [6]. Particularly, the petroleum-based cutting fluids are environmentally more difficult to handle compared with bio-based emulsions. Before disposal, special physical or chemical treatment techniques may be needed to remove hazardous components from the used cutting fluids by an EPA-permitted hazardous waste management agency. Studies have shown that statistically significant increases in several types of cancer as well as an increased risk of respiratory irritation or illness are due to prolonged exposure to cutting fluid mists [7], [8]. Thus, it would be beneficial for manufacturing applications to use lesser amounts of petroleum-based cutting fluids.

In recent times, alternative cutting fluids based on vegetable oils have been explored for machining operations [9], [10]. Due to their relatively low flash point (about 420°F), when petroleum-based cutting fluids are used, the heat at the workpiece-cutter interface often generates a mist, which is harmful to machine operators [11]. Flash point is the lowest temperature at which a liquid can form an ignitable mixture in air near the surface of the liquid. The lower the flash point, the easier it is to ignite the material. Having a high molecular weight (flash point of around 600°F), the soybean-based cutting fluids greatly reduce the chance of mist generation in machining processes. In addition, it has been reported that these soy-based cutting fluids have a very high film strength, which helps to lubricate the cutting-tool/work-piece interface, thereby reducing heat generated and tool wear [12], [13].

Though the bio-based cutting fluids have been available on the market for some time, there is not widespread use of them in industry. A limited number of studies on bio-based cutting fluids have been reported in the literature, which focused on specific cutting-fluid products [14-17]. For example, the studies by Belluco & DeChiffre's [14], [15] fo-

cused specifically on the performance of formulated oils blended with rapeseed oil, ester oil, and sulfur and phosphor additives used in drilling AISI 316L austenitic stainless steel. Their experimental data indicated that the bio-based fluids performed better than the mineral-oil-based products in terms of prolonged tool life, better chip breaking, lower tool wear, and lower cutting forces. Because bio-based cutting fluids can be formulated from different agricultural products, it is hard to make a general conclusion due to the bio-product diversity.

In this study, the cutting fluid was a soybean-based oil uniquely formulated through an engineered approach to increase oxidative stability of the soybean oil [18]. An improved understanding of the soybean-based cutting fluid through scientific evaluation will help manufacturing professionals recognize the benefits of this cutting fluid, and will better prepare them for making strategic machining decisions regarding the choice of cutting fluid.

Research Questions

The goal of this study, then, was to compare the effectiveness of a soybean-based cutting fluid with its petroleum alternate when used in CNC turning operations in order to evaluate their impact on the quality characteristics of the parts being turned. Different turning characteristics, namely surface roughness, tool life/tool wear, material removal rate, cutting force, machining vibration, etc., have been used in other studies to evaluate machining performance. Surface roughness is an important quality measurement of machined parts, and tool wear plays a critical role in determining the part quality and the machining cost. These two characteristics can be relatively easily measured in a machine shop without involving additional sensing hardware, thus they were selected in this study as machining quality characteristics in order to evaluate cutting-fluid effectiveness. The questions that this study addressed are:

- How will the surface roughness of the turned parts be impacted by the soybean-based cutting fluid compared with the petroleum-based cutting fluid?
- How will the wear of the cutting tool be impacted by the soybean-based cutting fluid compared with the petroleum-based cutting fluid?

The procedures used in the evaluation of the soybean-based cutting fluid are given in Figure 1.

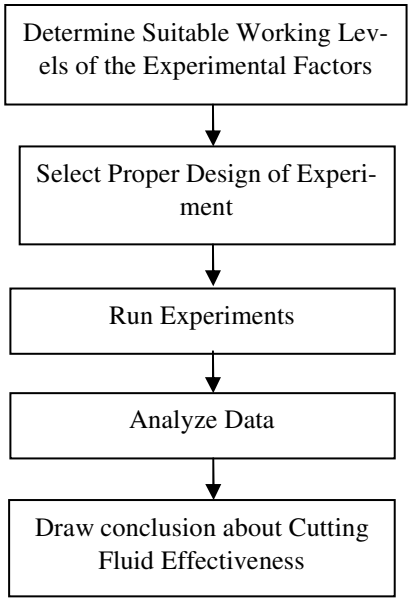

Figure 1. Study Procedures used in the Evaluation of the Soybean-Based Cutting Fluid

Experimental Study

Selection of Experimental Factors

Experimental factors were selected based on the literature review about machining theory and machining practice. Out of the three parameters—cutting speed, feed rate, and depth of cut—feed rate was found to play an important role in determining surface roughness and cutting speed was a significant factor impacting cutting-tool life [19]. In practice, all three machining parameters need to be applied at the same time and each can vary across a wide range of values. As with many other experimental studies on machining operations [14], [20-22], these three parameters were considered as independent variables in this study. Another control factor is cutting fluid condition: soybean-based, petroleum-based, and dry.

The cutting speeds and feed rates were selected with reference to the Machinery's Handbook (27th edition) and the catalog of the carbide insert for turning high carbon alloy steel. The levels of depth of cut were selected to emulate machine shop practice in consideration of both machining productivity and safety. The selected parameters along with their applicable codes and values are listed in Table 1.

Table 1. Parameters, Codes, and Level Values used for the Taguchi Design

Parameter	Code	Level 1	Level 2	Level 3
Control Factors				
Cutting Speed, ft/min (m/min)	A	300 (91.44)	340(103.632)	380 (115.824)
Feed Rate, ipr (mmpr)	B	0.008 (0.2032)	0.012 (0.3048)	0.016 (0.4064)
Depth of Cut, in (mm)	C	0.04 (1.016)	0.05 (1.27)	0.06 (1.524)
Cutting-fluid condition	X	dry cutting	soy fluid	petroleum fluid
Response Variable				
Surface Roughness Ra, µm				
Tool wear W*, mm				

* Tool flank wear will be measured after the cutting has completed a 7-inch long pass of the workpiece.

Design of Experiments

If a full factorial design were applied, at least 27 experimental runs must be conducted for each of the cutting-fluid conditions, even with single replication. For the three cutting-fluid conditions, the experimental study would be not only very time consuming but also costly because at least 81 tool inserts would be tested. Therefore, a Taguchi $L_9(3^4)$ orthogonal array shown in Table 2 was employed in the study which required 27 runs to cover the three machining parameters and the three cutting-fluid conditions. This table was used for recording the test results of surface roughness and tool wear data.

Experimental Materials and Supplies

- The workpiece material used in this study was E52100, a high-carbon, chromium-alloy steel. The chemical composition and major properties for workpiece material are listed in Appendix I. Because E52100 has great hardness and high wear resistance, the application of cutting fluids is a must when E52100 components are produced from machining processes due to its poor machinability (refer to Appendix I). The steel material was purchased as billets with a 7-inch diameter and was pre-cut into 9-inch lengths.

Table 2. Modified L_9 (3^4) Orthogonal Array Including Experimental Factors

L9 - orthogonal array					Cutting-fluid condition		
Run	**A (Cutting speed)**	**B (Feed rate)**	**C (Depth of cut)**	**D (Empty)**	**X1 (Dry)**	**X2 (Soy)**	**X3 (Petroleum)**
1	1	1	1				
2	1	2	2				
3	1	3	3				
4	2	1	2				
5	2	2	3				
6	2	3	1				
7	3	1	3				
8	3	2	1				
9	3	3	2				

- The cutting tool used was a carbide insert CNMG432 EGE AC700G (Sumitomo Electric Carbide, Inc.), which is coated with multi-phase Al_2O_3. The coating, along with a tough carbide substrate, makes it suitable for rough turning carbon steels and alloy steels.
- The soybean-based cutting fluid that was used—SoyEasy™ Cool-GHP Plus—is an environmentally friendly product produced by Environmental Lubricants Manufacturing, Inc. [18]. This cutting fluid was maintained at 5% concentration (by volume) through the entire experiment.
- The petroleum-based cutting fluid used was Castrol Clearedge 6510, produced by Castrol Industrial Americas. It is a semi-synthetic cutting and grinding fluid for ferrous metals. This cutting fluid was maintained at 5% concentration (by volume) through the entire experiment.

Experimental Hardware and Software Set-up

This experiment was conducted using the following hardware and software:

- CNC Turning Center: Haas SL-20 (Haas Automation, Inc).
- Surface Roughness Digital Measurement Device: Surtronic 25 Roughness Checker (Taylor Hobson, Inc). The setup for surface roughness measurement is shown in Figure 2.

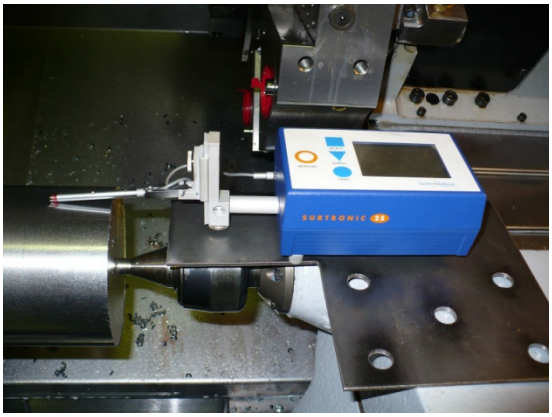

Figure 2. Setup of Surtronic 25 Roughness Checker

- Mitutoyo Toolmaker's Microscope with a magnification of 15 was used for measuring flank wear that occurred on the flank face of an insert resulting from abrasive wear of the cutting edge against the machined surface. The wear can be read as small as 0.001mm. The microscope and a picture of a worn insert taken under the microscope are shown in Figures 3 and 4.
- Microsoft Excel and JMP software packages for charting data and statistical analysis.

Figure 3. Microscope used for Tool Wear Measurement

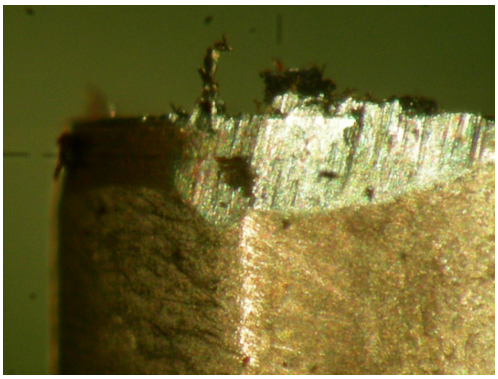

Figure 4. Flank Wear Example under Microscope

Data Collection

In the experiment, the workpiece material E52100 was prepared as 7" × 9" metal billets. It was chucked between the spindle chuck and the tailstock center in the Haas turning center, as shown in Figure 5. One specific tool insert was used to turn and clean off the billet surface to make sure that all tested inserts would cut the clean workpiece surface without any interference from rust or dirt. In Figure 6, a copper tube connected to the cutting-fluid orifice was directed to the insert and workpiece to flood the interface of the workpiece and the insert.

Each experimental combination was conducted only once across 27 experimental runs for all of the experimental combinations listed in Table 2. A complete randomization of the

27 cuts was not done since switching from one cutting fluid to another for each experimental run involved a thorough cleaning of the sump and flushing of all the fluid in the system. Therefore, the experimental runs were conducted in batches—turning at the soybean-fluid and petroleum–fluid, and dry conditions in sequence. The fluid tank and pipes were totally cleaned when the cutting fluids were switched. The sequence of the nine runs under each cutting-fluid condition was randomized in order to minimize other unforeseen factors that might bias the experimental results.

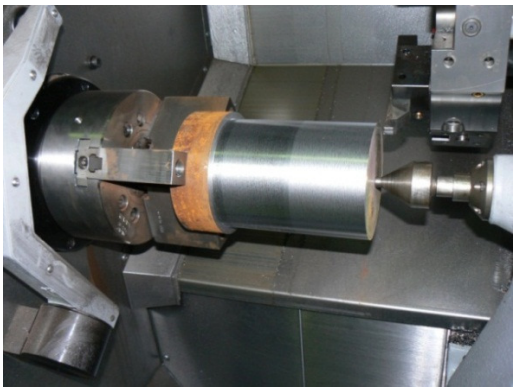

Figure 5. Workpiece after One Turning Path

An NC part program was written with different cutting parameters specified to let the Haas CNC turning center cut the work piece 7" long starting from the right end face. After the cutting pass, the surface roughness was measured at four spots evenly around the periphery of the billet. One picture of the measurements is shown in Figure 2. The average of the four measurements was recorded into Table 3.

After each cutting pass, the tool insert was removed from the tool holder and the flank wear was measured under the microscope. After the tool wear was measured, the tool was documented and stored, and a new tool insert was mounted into the tool holder for the next experimental run. The results of the surface roughness and insert flank wear measurements are shown in Table 3.

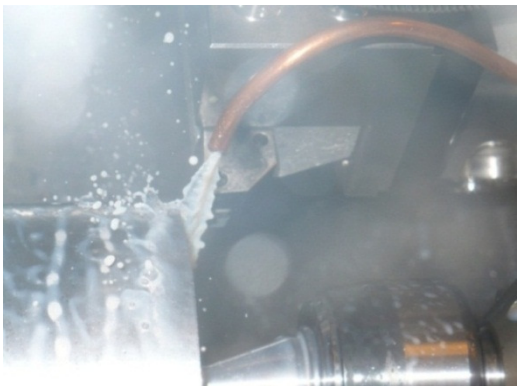

Figure 6. Cutting Fluid Applied to Insert and Workpiece

Data Analysis

Data Analysis on Surface Roughness

A visual examination of the data in Table 3 found that surface roughness, Ra, values for the soybean-based fluid condition (column X2) were consistently lower than for the dry condition (column X1) except that during run #2, the surface roughness was slightly larger (3.98 vs. 3.54). A sim-

Table 3. Surface Roughness and Tool Wear Data Collected in Experiment Runs

L9 - Inner Control Factor Array					Surface Roughness, Ra (mm)			Tool Wear, W (mm)		
Run	**A (speed)**	**B (feed)**	**C (depth)**	**D**	**X1 (Dry)**	**X2 (Soy)**	**X3 (Petro.)**	**X1 (Dry)**	**X2 (Soy)**	**X3 (Petro.)**
2	1	2	2		3.54	**3.98**	**6.32**	0.126	0.072	**0.157**
3	1	3	3		4.54	3.92	1.92	0.203	0.055	0.107
4	2	1	2		6.66	1.62	1.84	0.156	0.088	0.154
5	2	2	3		3.32	1.46	1.72	0.162	0.099	0.105
6	2	3	1		5.02	1.64	**5.78**	0.267	0.107	0.113
7	3	1	3		7.42	1.44	1.80	0.202	0.110	0.087
8	3	2	1		9.00	1.86	1.90	0.173	0.093	0.166
9	3	3	2		4.42	2.26	1.72	0.188	0.138	0.143

ilar result can be seen when comparing columns X3 and X1, which is the roughness comparison between the petroleum fluid and the dry conditions. However, for run #2, the Ra value for the petroleum condition was almost twice that for the dry condition (6.32 vs. 3.54); and, for run #6, the Ra value for the petroleum condition was slightly larger than the dry condition (5.78 vs. 5.02). Both of the comparisons indicated abnormal results because the surface roughness would normally be better when cutting fluids are applied. The abnormal data were not discarded and were treated as variations for analysis.

ANOVA Analyses on Surface Roughness

Analysis of variance (ANOVA) is an analytical approach in which the mean of a variable as affected by different factors or factor treatment combinations is analyzed. A one-way analysis of variance is the simplest form which can test differences between more than two groups or treatments by an F-test. According to the research questions, the hypothesis about surface roughness was:

H_0: There are no significant differences among the cutting-fluid conditions (Ra_1=Ra_2=Ra_3).

H_1: Not all of the averages for the three cutting-fluid conditions are equal. In other words, at least for one pair of treatments, surface roughness is different.

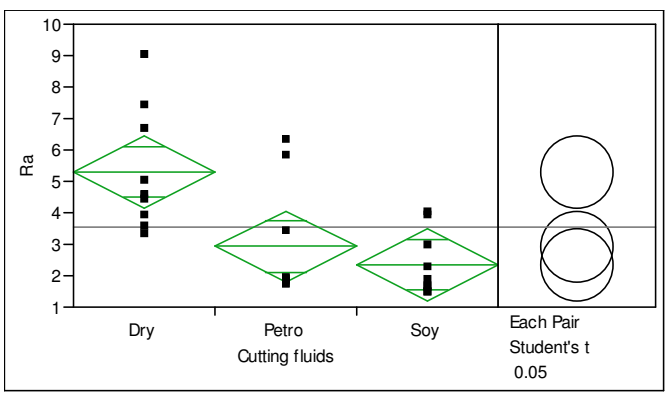

Figure. 7 One-way Analyses of Surface Roughness by Cutting Fluids

The statistical one-way analysis was conducted and the graphical display of the comparison results are shown in Figure 7. The longest horizontal line represents the mean and the other two short horizontal lines represent the 25th and 75th percentile values, respectively. The variation of surface roughness was large when no cutting fluids were applied; instead, for the soybean-based fluid condition, the surface roughness showed the smallest range of variation and the smallest average; for the petroleum-based fluid condition, a couple of surface roughness values fell far from the rest of the data, and the average value was in-between that of the dry and soybean conditions. The circles in the right column represent the probability of the response variable at three cutting-fluid conditions. A large portion of overlap of the two circles in Figure 7 indicated that the difference between the two cutting-fluid conditions may not be significant. The circle on the top (dry condition) does not have any overlap with the other two circles, indicating the surface roughness for the dry condition was different from the two cutting-fluid conditions. The result that there are significant differences among the three cutting-fluid conditions can be confirmed statistically from Table 4, because the small probability value (0.0021) given in the ANOVA analysis tells us that the variation in the observations was not caused by random variation alone. Therefore, the null hypothesis should be rejected.

Table 4. Analysis of Variance for Surface Roughness by Cutting Fluids

Source	DF	Sum of Squares	Mean Square	F Ratio	Prob > F
Fluids	2	44.3344	22.1672	8.0379	0.0021
Error	24	66.1882	2.7578		
Total	26	110.5227			

T-test on Surface Roughness for Pairs Treatment

The hypothesis test above only tells us that there were significant differences among treatments in the experiment as a whole. Following the hypothesis test, the t-test was performed in order to identify which cutting fluid conditions generated the surface roughness differences. The least significant difference (LSD) can be computed by Equation (1)

$$LSD = t_{\alpha/2}\sqrt{MSE(\frac{1}{n_1}+\frac{1}{n_2})} \quad (1)$$

where n_1 and n_2 are the number of samples collected for each cutting-fluid condition: $n_1 = n_2 = 9$. MSE is the mean square error displayed in Table 4: MSE = 2.7578.

If using student's t, $t_{a/2}$ is the t-value corresponding to the significant level a (pre-determined as 0.05) with 16 degrees of freedom: $t_{a/2} = 2.120$. Using the Bonferroni adjustment, a was set to 0.05 for the entire experimental treatment comparisons. As there were three pair-wise comparisons in this experiment (namely as dry vs. petroleum, dry vs. soy, petro-

leum vs. soy), the significant level for the pair-wise comparisons can be adjusted to 0.0167 (=0.05/3). Therefore, $t_{a/2}$ was the t-value at a probability of 0.0167 with 16 degrees of freedom: $t_{a/2} = 2.672$. The LSD can be computed as follows.

$$LSD = 2.672\sqrt{2.7578 \times (\frac{1}{9} + \frac{1}{9})} = 2.091$$

Based on the calculated LSD, and because the differences in surface roughness means at the dry and petroleum conditions was 2.38 which was larger than the calculated LSD, the surface roughness results for the dry and petroleum cutting conditions were significantly different. Similarly, the surface roughness results for the dry and soy cutting conditions were significantly different, as their mean difference of 2.962 was larger than the LSD. It can be clearly seen that there was no difference between the petroleum and the soy cutting conditions. The above pair-wise comparison results are labeled in Table 5—the average of surface roughness for the dry condition is marked as level 1 (L1) and the other two as level 2 (L2). Tables 4 and 5 together tell us that the two cutting fluids did not produce significant differences in smoothing surface roughness, but the surface finish at the two wet conditions was statistically better than for the dry condition.

Table 5. Comparisons of Surface Roughness for each Pair using Student's t Test

Level	Label*		Mean
X1(Dry)	L1		5.311
X3(Petroleum)		L2	2.931
X2(Soy)		L2	2.349

* Levels (L1 and L2) not Connected by the Same Letter are Significantly Different.

Data Analysis on Tool Wear

Visual inspection of tool wear data at the three cutting-fluid conditions listed in Table 3 found that the tool wear for the two cutting-fluid conditions was consistently smaller than for the dry condition. There was only one abnormal result in run #2 in that the tool wear of the petroleum-based fluid condition was slightly larger than the value for the corresponding dry condition (0.157 vs. 0.126). This abnormal tool wear matched with the unusual surface roughness result that occurred in run #2. To some extent, this large tool wear may provide a partial explanation why such a high surface roughness occurred in run #2, since tool condition was an important factor impacting surface finish. Overall, all of the tool wear data in Table 3 are smaller than the flank tool wear of 0.5mm, which is the cutoff value set by ISO for defining an effective tool life. Figure 8 shows sample pictures of the tool inserts with the flank wear for dry, soybean, and petroleum conditions.

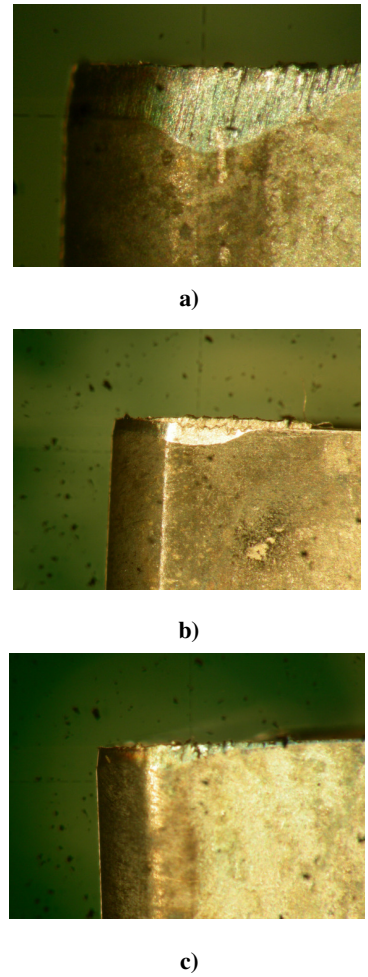

Figure 8. Tool Inserts Along with Flank Wear at Different Cutting-Fluid Conditions— a) Dry Condition, b) Soy Fluid, c) Petroleum Fluid (all seen at magnification 15)

ANOVA Analyses on Tool Wear

The one-way ANOVA analysis was conducted regarding the tool wear for the three cutting conditions. According to the research questions, the hypothesis for tool wear was:

H_0: There are no significant differences among the cutting fluid conditions ($W_1=W_2=W_3$).

H_1: Not all of the tool wear averages for the three cutting -fluid conditions are equal.

The ANOVA results are shown in Table 6; the graphic results are displayed in Figure 9. The average tool wear for the soybean cutting fluid condition (column 2 in Figure 7)

was at the lowest level, the average tool wear for the dry cutting was at the highest level, and the one for the petroleum cutting fluid was in-between. Representing the probability, the circle for the dry condition stands far away from the other two circles, which means that the tool wear for the dry condition was significantly different from the other two conditions. In other words, the application of cutting fluids significantly reduced tool wear. The small probability value (<0.0001) given by the F-test in the ANOVA analysis in Table 6 confirmed this observation. Therefore, the null hypothesis should be rejected.

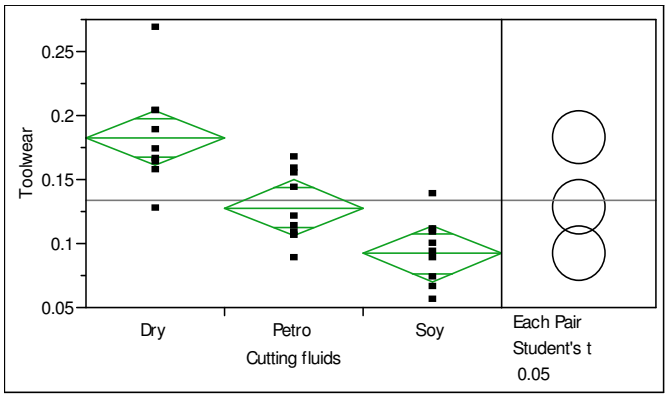

Figure 9. One-way Analyses of Tool Wear by Cutting Fluids

Table 6. Analysis of Variance for Tool Wear by Cutting Fluids

Source	DF	Sum of Squares	Mean Square	F Ratio	Prob > F
Fluids	2	0.0374055	0.018703	18.6739	<.0001
Error	24	0.0240371	0.001002		
Total	26	0.0614426			

T-test on Surface Roughness for Pairs Treatment

The ANOVA analyses in Table 6 indicated that there were significant differences among the three cutting-fluid conditions. By calculating the LSD tool wear, performing the t-test was able to identify which cutting-fluid conditions made a significant difference in reducing tool wear. Using Equation (1), the Bonferroni-adjusted LSD for tool wear was calculated as

$$LSD = 2.672\sqrt{0.001002\times(\frac{1}{9}+\frac{1}{9})} = 0.0398$$

From Table 7, the tool wear differences of the pair-wise comparisons—dry vs. petroleum, and dry vs. soy—were 0.054 (=0.182-0.128) and 0.092 (=0.182-0.092). Because these two differences were larger than the LSD tool wear, it can be concluded that applying the two cutting fluids significantly reduced tool wear. As noticed, there was a very small portion of overlap between the two circles representing the petroleum and the soy cutting-fluid conditions (see Figure 9). The tool wear difference for the petroleum and soy conditions was 0.036, which was slightly smaller than the Bonferroni-adjusted LSD of 0.0398, but larger than the calculated LSD from the student's t-value (2.120). The LSD from Student's t was computed as

$$LSD = 2.120\sqrt{0.001002\times(\frac{1}{9}+\frac{1}{9})} = 0.032$$

From the student's t-test, the tool wear results were significantly different for the petroleum and soy cutting-fluid conditions. Therefore, the three cutting-fluid conditions are labeled as L1, L2, and L3, respectively, in Table 7. The pair-wise comparison results concluded that the three tool wear averages were significantly different by pairs, and the soybean fluid performed statistically better than the petroleum alternate in reducing tool wear.

Table 7. Comparisons of Tool Wear for each Pair using Student's t Test

Level	Label*			Mean
X1(Dry)	L1			0.182
X3(Petroleum)		L2		0.128
X2(Soy)			L3	0.092

* Levels (L1, L2, and L3) not Connected by the Same Letter are Significantly Different.

Conclusions and Summary

An L_9 (3^4) Taguchi design was used to compare an experimental soybean-based cutting fluid against dry and petroleum-based cutting fluids in turning operations. The experimental data analysis revealed that the soybean-based cutting fluid performed better than the petroleum alternate product in terms of controlling tool wear, and both of the two cutting fluids performed similarly well in reducing surface roughness. The experimental study covered three machining parameters and three cutting-fluid treatments. If a full factorial DOE approach were to be used, at least 81 (3×3×3×3) data points would need to be collected in order to include all of the factors. The selected L_9 (3^4) orthogonal array with a total of 27 experimental runs saved a lot of resources. Providing supporting evidence for the manufacturing professionals who may consider green manufacturing and sub-

stituting the conventional cutting fluids with the bio-based alternates, the experimental approach presented here can be a reference applicable to real manufacturing planning practice.

It cannot be denied that the Taguchi Design is a fractional factorial design in nature. Considering the limited amount of resources, this study focused on the primary comparison of the machining performance difference brought by different cutting-fluid conditions. As noticed, there were no repetitions for the experimental run under each cutting-fluid condition. If more data were collected in this undergraduate research project, the signal/noise ratio could be introduced to identify the optimal cutting parameters for each of the cutting fluids.

References

[1] Rao, P. N. (2009). *Manufacturing Technology Volume 2—Metal cutting and Machine Tools*. New Delhi, India: Tata McGraw-Hill Publishing Company, Ltd.

[2] Rusinko, C. A. (2007). Green manufacturing: An evaluation of environmentally sustainable manufacturing practices and their impact on competitive outcome. *IEEE Transactions on Engineering Management*, 54(3), 445-454.

[3] Siniawski, M. & Bowman, C. (2009). Metal working fluids: Finding green in the manufacturing process. *Industrial Lubrication and Tribology*, 61(2), 60-66.

[4] Diniz, A. E. & Oliveira, A. (2004). Optimizing the use of dry cutting in rough turning steel operations. International. *Journal of Machine Tools and Manufacture,* 44(10), 1061-1067.

[5] Khan, M. M. A. & Dhar, N. R. (2006). Performance evaluation of minimum quantity lubrication by vegetable oil in terms of cutting force, cutting zone temperature, tool wear, job dimension and surface finish in turning AISI-1060 steel. *Journal of Zhejiang University: Science*, 7(11), 1790-1799.

[6] Cutting fluids. In *P_2Rx Wiki,* Retrieved February 20, 2012, from http://lib.wmrc.uiuc.edu/p2rx-wiki/index.php/Cutting_fluid.

[7] Adler, D. P., Hii, W. W. S., Michalek, D. J. & Sutherland, J. W. (2006). Examining the role of cutting fluids in machining and efforts to address associated environmental/health concerns. *Machining Science and technology,* 10(1), 23-58.

[8] Akagawa, A. (1997). Development of cutting fluids which are environment and human friendly. *International Journal of the Japan Society for Precision Engineering,* 31(4), 253-256.

[9] Maleque, M. A., Masjuki, H. H. & Supuan, S. M. (2003). Vegetable-based biodegradable lubricating oil additives. *Industrial lubrication and Tribology*, 55 (3), 137-143.

[10] Singh, A. K. & Gupta, A. K. (2006). Metalworking fluids from vegetable oils. *Journal of Synthetic Lubrication,* 23(4), 167-176.

[11] Raynor, P. C., Kim, S. W. & Bhattacharya, M. (2005). Mist generation from metalworking fluids formulated using vegetable oils. *Annals of Occupational Hygiene*, 49(4), 283-293.

[12] Beness, J. (n.d.). Engineering metal working fluids. American Machinist—General Cutting Update. Retrieved September 20, 2011, from http://www.cutting-cool.americanmachinist.com/ArticleDraw.aspx?artid=46250

[13] Smith, D. & Frazier, B. (n.d.). The benefits of Bio-based lubricants. Gear Solutions. Retrieved February 20, 2012, from http://www.gearsolutions.com/article/detail/5990/the-benefits-of-bio-based-lubricant.

[14] Belluco, W. & Chiffre, L. D. (2002). Surface integrity and part accuracy in reaming and tapping stainless steel with new vegetable based cutting oils. *Tibology International*, 35(12), 865-870.

[15] Belluco, W. & Chiffre, L. D. (2004). Performance evaluation of vegetable-based oils in drilling austenitic stainless steel. *Journal of Materials Processing Technology*, 148(2), 171–176.

[16] Chiffre, L. D. & Belluco, W. (2002). Investigations of cutting fluid performance using different machining operations. *Lubrication Engineering*, 58(10), 22-29.

[17] Xavior, M. A. & Adithan, M. (2009). Determining the influence of cutting fluids on tool wear and surface roughness during turning of AISI 304 austenitic stainless steel. *Journal of Materials Processing Technology,* 209(2), 900-909.

[18] Environmental Lubricants Manufacturing: Why bio based oils make better lubricants. Retrieved February 20, 2012, from http://www.elmusa.com/news/whybiobased.htm.

[19] Black, J. T. & Kohser, R. A. (2008). *DeGarmo's Materials and Processes in Manufacturing* (9th ed.). New York, NY: John Wiley & Sons, Inc.

[20] Kirby, E. D., Zhang, J. Z., Chen, J. C. & Chen, J. (2006). Optimizing Surface Finish in a Turning Operation Using the Taguchi Parameter Design. *International Journal of Advanced Manufacturing Technology*, 30, 1021-1029.

[21] Huang, M. F. & Lin, T. R. (2004). Application of grey - Taguchi method to optimise drilling of aluminium alloy 6061 with multiple performance character-

istics. *Materials Science and Technology*, 20(4), 528-532.

[22] Zhang, J. Z. & Nie, H. (2009). Experimental study and logistic regression modeling for machine condition monitoring through microcontroller-based data acquisition system. *Journal of Advanced Manufacturing System,* 8(2), 177-192.

Biographies

DR. JULIE ZHANG is an associate professor of Industrial Technology at University of Northern Iowa. She teaches courses related to manufacturing processes, manufacturing automation, statistical quality control, total quality management and CAD/CAM/CNC applications. Her research includes green manufacturing and evaluation of bio-based cutting fluids, real-time cutting tool condition monitoring, and adaptive control for automated machines. Dr. Zhang can be contacted at juie.zhang@uni.edu

DR. P.N. RAO is a professor of Industrial Technology at University of Northern Iowa in Cedar Falls, Iowa. He received his B. E. degree in Mechanical Engineering from Sri Venkateswara University, Tirupati, M. E. degree from Birla Institute of Technology and Science, Pilani and Ph. D. from Indian Institute of Technology, New Delhi, India. His current teaching and research interests include Manufacturing Engineering, Metal Cutting, CNC, CAD/CAM, Product Design, Rapid Prototyping, CIM, Tool Design, CAPP, and Technology Education. He is the author and co-author of a number of research papers in national and international journals and conferences along with a number of textbooks.

MS. MARY ECKMAN is currently an MS graduate student in the Department of Industrial Technology at the University of Northern Iowa.

Appendix I. Chemical Composition and Major Property Data for Workpiece Material E52100

Mechanical Property	
Hardness, Brinell	229
Modulus of Elasticity	210 GPa
Tensile Strength	0.74 GP
Machinability	40% (Based on 100% machinability for AISI 1212 steel)
Composition of Chemical Components	
Carbon, C	0.980 - 1.10 %
Chromium, Cr	1.45%
Iron, Fe	97.0 %
Manganese, Mn	0.35 %
Phosphorous, P	<= 0.025 %
Silicon, Si	0.230 %
Sulfur, S	<= 0.025 %

ANALYSIS OF SOLAR PANEL EFFICIENCY THROUGH COMPUTATION AND SIMULATION

Hongyu Guo, University of Houston-Victoria; Mehrube Mehrubeoglu, Texas A&M University-Corpus Christi

Abstract

Solar panels are known to have low efficiency, typically less than 25%. And combined with a solar panel orientation that is not optimized for the direction of the incident sun, the efficiency is further reduced. In this study, a computational and visual model was developed for the apparent diurnal motion of the sun to determine the declination and azimuthal angles at which a solar panel should be oriented at any time on any day for active solar trackers to maximize the received solar irradiance at any location on earth. A software simulation tool was developed to compute sunrise time, sunset time, and duration of daytime for any latitude using a geocentric model. The efficiency of solar panels due to incident angles was defined and analyzed for reduced-degree-of-freedom solar tracking systems. The analysis has significance in providing guidance in the decision process of initial solar panel investment and installation regarding the trade-offs between efficiency and cost.

Introduction

Solar panels have efficiencies lower than 40% and most typically less than 25% [1]. Many factors contribute to this low efficiency, including solar panel technology, materials and charging process. Orientation of the solar panel is one of the major factors contributing to solar energy conversion efficiency. In this study, the authors focused on the orientation of solar panels to maximize received solar irradiation to improve energy conversion based on the received solar energy.

Depending on the nature of the application and the cost requirements, the orientation of the solar panel can be either fixed or movable. Fixed-orientation solar panels are the least expensive to install but they are also the least efficient. A simple improvement can be made by a rotatable solar panel on a single axis where the tilt angle is adjusted seasonally, or monthly. To make better use of the solar energy, some tracking systems are designed to minimize the incident angle of the sunlight onto the solar panel [2-7]. The sophistication of the tracking system depends on the trade-off between cost and efficiency. Single-axis as well as dual-axis trackers exist. A single-axis tracker can be designed as a horizontal single-axis tracker (HSAT), vertical single-axis tracker (VSAT), or tilted single-axis tracker (TSAT). Different types of dual-axis trackers have also been developed and depend on the choice of the primary and secondary axis. With different system drive methods, tracking can be active or passive. The goal of dual-axis trackers is to make the solar panel track the sun so that the sun's rays are always orthogonal to the solar panel.

A typical solar tracking method requires photoelectric detection that utilizes a photoelectric sensor to follow the sun; however, this method suffers from unpredictable weather conditions which could affect tracking of the sun. A weather-independent method involves solar trajectory tracking through mathematical computations [8]. Although papers on solar tracking have been published, none includes simulations for visualizations [8-11]. Numerical information on local sunrise, sunset time, and length of a day in a year at any latitudinal location is available in astronomical almanacs and online at institutions such as U.S. Naval Observatory; however, a useful computational and visualization model of these astronomical events to assist with solar panel orientation for maximum solar irradiance at any time, any day and any location was not found in the literature. Some groups have investigated monthly solar panel orientation strategies [12]. The solar panel efficiency affected by the orientation is of interest in multiple applications [13-15].

In this study, a geocentric model was developed for computation and visualizations of the apparent diurnal motion of the sun and to simulate the computed orientation of an active dual-axis solar panel tracking system. Simulations of the apparent diurnal motion of the sun can be used to drive the dual-axis solar tracker. Snapshots of the diurnal motion of the sun for a sample date are shown in Figure 1. Duration of daytime and nighttime plots for various latitudes are displayed. MATLAB programs were developed for this simulation and visualization. In practical applications of solar panels, to reduce the cost of the installation, a reduced-degree-of-freedom solar tracking system is often adopted. These systems include seasonally adjusted fixed solar panels and single-axis solar trackers. The efficiency due to incident angles of these reduced-degree-of-freedom solar tracking systems is defined and investigated. This analysis has significance in practice for engineers who make decisions on the trade-offs between efficiency and cost in the initial planning stage of investment and installation.

Solar Tracking by Computing the Solar Declination and Azimuthal Angles

A simple model can be used to compute and simulate solar tracking. For the precision requirement of solar tracking, it is enough to assume that the orbit of the earth is a circle. It is more convenient, however, to use a geocentric model than a heliocentric model. It is necessary to understand the relationship between the horizon plane and the plane depicting the diurnal motion of the sun to see how the sun's location and orbit affects sunrise time, sunset time, and the duration of daytime and nighttime, and in effect how the solar panel should be oriented. Geometric equations relating the duration of daytime and nighttime to the relative position of the sun to the equatorial plane and the horizon plane are derived below.

Solar Declination on Any Date throughout the Year

The celestial sphere is shown in Figure 1, where the earth is at the center. N is the celestial North Pole. If the observer is standing at a point on earth with latitude, λ , then the great circle in the x-y plane in the Cartesian coordinate system with points S, B, R, and A is the local horizon circle. The great circle with points E, L, B, N, Z, H, Q, and A is the local meridian. This circle is in the y-z plane.

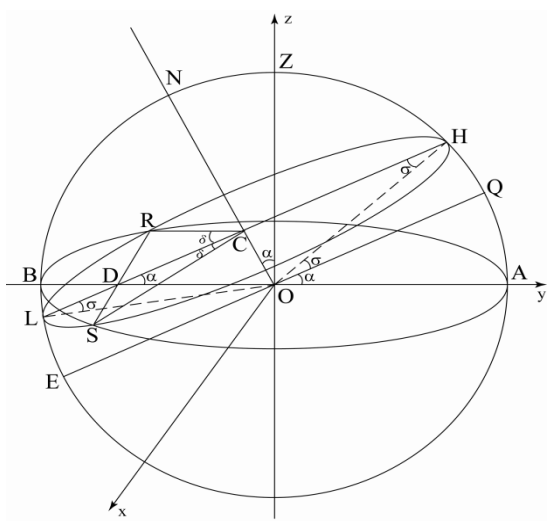

Figure 1. Diurnal Motion of the Sun on the Celestial Sphere

The line EQ is the diameter of the celestial sphere, which is also in the equatorial plane. (The equatorial plane is omitted in Figure 1 for clarity.) ON is the axis of the celestial sphere. ON is perpendicular to EQ. The small circle with points H, R, L, and S is the diurnal path of the sun. C is the center of this small circle. R is the point of sunrise, whereas S is the point of sunset. H marks the position of the sun at noon, and L is the position of the sun at midnight. The arc RHS represents the daytime path, and the arc SLR represents the nighttime path of the sun. LCH is a diameter of that small circle (CR, CL, CS, and CH are radii of the same circle)**.** The plane of that small circle lies parallel to the equatorial plane and perpendicular to the axis ON. Hence, LH is parallel to EQ and LH is perpendicular to ON. Assume the radius of the celestial sphere is 1.

$\angle$ ZOQ = λ is the local latitude. Denote

$$\alpha = \frac{\pi}{2} - \lambda \tag{1}$$

as the co-latitude. In Figure 1,

$$\angle QOA = \angle CDO = \alpha \tag{2}$$

The solar declination is denoted by

$$\sigma = \angle HOQ \tag{3}$$

which is the angle from the sun at noon to the equatorial plane. σ changes throughout the year with a period of one year. At the vernal equinox, the sun is on the equator. H coincides with Q, and $\sigma = 0$. The angle between the ecliptic plane and the equatorial plane is called the obliquity of the ecliptic, with a value $\varepsilon = 23.5°$. At the summer solstice, the sun is the highest in the sky and $\sigma = \varepsilon$, which has the maximum value. Figure 1 displays the diurnal path of the sun for an arbitrary day in the year, with a generic value of and $\sigma \neq \varepsilon$, . The obliquity of the ecliptic ε is not shown in Figure 1. At the autumnal equinox, the sun is on the equator again. H coincides with Q once again, and $\sigma = 0$. At the winter solstice, the sun is the lowest in the sky and $\sigma = -\varepsilon$, which is the minimum value.

The solar declination σ for any particular day in the year can be found, hence, the duration of daytime and nighttime can be computed for any latitude on earth and any day in the year.

Let θ denote the ecliptic longitude (not shown in Figure 1). θ varies from 0 to 2π when the sun moves on the ecliptic circle on the celestial sphere in one year. At vernal equinox $\theta = 0$; at summer solstice $\theta = \pi/2$; at autumnal equinox $\theta = \pi$; and at winter solstice $\theta = 3\pi/2$. The altitude of the sun

projected above the equatorial plane can be expressed as $\sin\theta\sin\varepsilon$. On the other hand, the same altitude is equal to $\sin\sigma$ in terms of the solar declination σ. By equating these two,

$$\sin\sigma = \sin\theta\sin\varepsilon \tag{4}$$

the solar declination σ can be found in terms of ecliptic longitude θ. When using the approximation of a circular orbit of the earth around the sun, θ can be assumed to change with a uniform angular velocity in the year. Let Y = 365.24 be the number of days in a year and let D be the number of days of the date of concern counting from vernal equinox. Then θ and D are simply related by

$$\theta = 2\pi D / Y \tag{5}$$

From Equations (4) and (5),

$$\sigma = \sin^{-1}(\sin\varepsilon\sin\theta) = \sin^{-1}(\sin\varepsilon\sin(2\pi D/Y)) \tag{6}$$

The solar panel should be oriented with an angle $\lambda + \sigma$ from the horizontal plane, which is the altitude of the sun at local noon.

Sunrise, Sunset and Duration of Daylight

The azimuthal rotation of the solar panel should follow the sun from sunrise to sunset. In Figure 1, the radius r of the small circle can be found by

$$r = \overline{CL} = \overline{CH} = \overline{CR} = \overline{CS} = \cos\sigma \tag{7}$$

Also,

$$\overline{CD} = \overline{OC}\cdot\cot\alpha = \sin\sigma\cdot\cot\alpha = \sin\sigma\cdot\tan\lambda \tag{8}$$

Since $\overline{CR} = \overline{CS}$, and $\overline{CD}$ bisects the angle $\angle RCS$, using Equations (7) and (8), the following Equation 9 is obtained:

$$\cos\delta = \frac{\overline{CD}}{\overline{CR}} = \frac{\sin\sigma\cdot\tan\lambda}{\cos\sigma} = \tan\sigma\cdot\tan\lambda \tag{9}$$

This yields

$$\delta = \cos^{-1}(\tan\sigma\cdot\tan\lambda) \tag{10}$$

The duration of the nighttime, n, is computed in hours as

$$n = 2\delta\cdot\frac{24}{2\pi} = \frac{24\delta}{\pi} \tag{11}$$

The duration of the daytime, d, is given in hours as

$$d = 24 - 24\delta/\pi = 24(1-\delta/\pi)$$

Substituting for δ from Equation (10), d is obtained as

$$d = 24[1-(\cos^{-1}(\tan\sigma.\tan\lambda))/\pi] \tag{12}$$

Using Equation (6), the duration of the daytime can be expressed as

$$d = 24 - \tfrac{24}{\pi}\cos^{-1}\{\tan\lambda\cdot\tan[\sin^{-1}(\sin\varepsilon\sin(2\pi D/Y))]\} \tag{13}$$

The sunrise time is then

$$T_r = 24\delta/2\pi$$
$$= (\tfrac{12}{\pi})\cos^{-1}\{\tan\lambda\cdot\tan[\sin^{-1}(\sin\varepsilon\sin(2\pi D/Y))]\} \tag{14}$$

and the sunset time is

$$T_s = 24 - T_r \tag{15}$$

in hours counting from midnight. All the times are local time for that particular longitude of the location of concern. The local time needs to be converted to standard time of the time zone where the location is in before they can be compared with published numerical data or observational data.

It is easy to check some special cases. When λ = 0. which is for a location on the equator, at any time during the year, d = 12, which means the daytime and nighttime are equal. If σ = 0, which is for the dates of the vernal equinox and autumnal equinox, then d = 12, which means the daytime and nighttime are equal for all different latitudes.

Computer Simulations

The algorithms for the diurnal motion of the sun and duration of daytime and nighttime were implemented in MATLAB based on the equations derived in the following section.

Diurnal Motion of the Sun

The diurnal motion and its plane for an arbitrarily chosen date, May 2, 2012, is shown in Figure 2 for different latitudes l. The software developed allows the user to choose any date and any latitude or location. Figure 2 shows the horizon plane (horizontal plane in all sub-figures) and the equatorial plane (plane parallel to the diurnal motion plane of the sun). The sphere represents the celestial sphere with the earth at its center. The small red ball represents the sun. Figure 2 can be validated with the appropriate values for latitude l and the solar declination s, based on the date of the

year described earlier. For example, for the date May 2, 2012, D = 42 (total number of days from vernal equinox March 21 to May 2) and s = 15.30° from Equation (6). For l = 90°, d = 0 (Equation (10)); then d = 24 hours, and n = 0 hours, as expected for the North Pole in summer. This is depicted in the top left subplot of Figure 2. Diurnal orbit of the sun is entirely above the horizon plane on the chosen date such that d = 24 hours for that day and n = 0, as expected for the North Pole. The bottom right subplot of Figure 2 is the diurnal path of the sun at l = -90 (South Pole) on May 2, 2012. Similarly, when l = 0, half of the diurnal orbit of the sun is above and the other half is below the horizon plane, suggesting equal day and night duration of 12 hours.

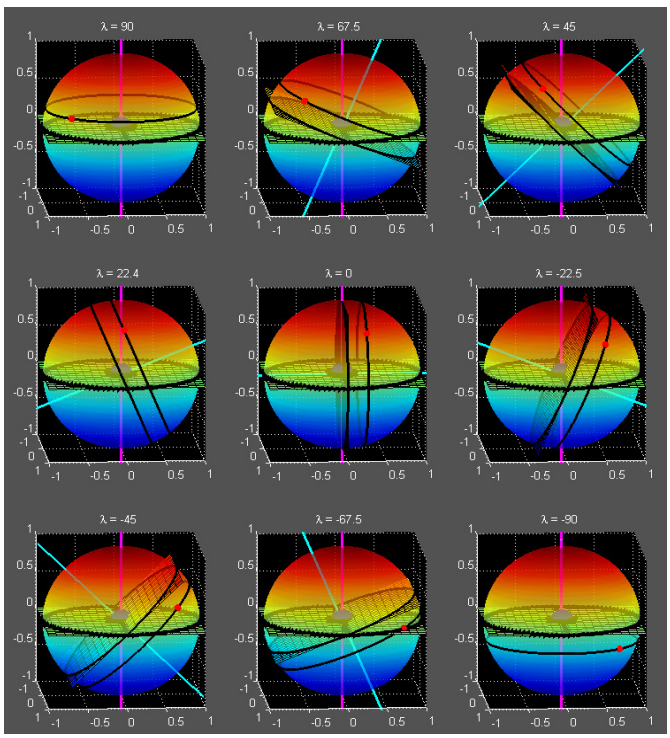

Figure 2. Computer Simulation of the Diurnal Motion of the Sun for May 2, 2012

Sunrise and sunset times for this date can be found from Equations (14) and (15), depending on the local latitude. Visual depiction of duration of daytime and nighttime for a given date is described in the next section.

Duration of Daytime for Any Latitude and Date

Figure 3 shows the duration of daytime and nighttime for one year for different latitudes l. Figure 3 was obtained by applying Equation (14) for each day of the year from January 1 to December 31. The duration of daytime on May 2, 2012, for a given l in Figure 3 (vertical green line) can be compared with the orbit of the sun on that day in Figure 2 in corresponding sub-figures. The comparison validates the results. Note, for example, for l = -45°, d = 9.88 hours and n = 14.12 hours, as depicted in Figure 3, bottom left subplot. These computations also match the depiction of daytime and nighttime durations in Figure 2 (bottom left), where the diurnal path of the sun is more below the horizon plane than it is above, visually validating the computations for May 2, 2012, with a longer nighttime than daytime. For this latitude, T_r = 7.06 hours after midnight, which is 7:04 AM and T_s = 16.94 hours, which is 4:56 PM. Notice that T_r and T_s represent local time instead of standard time.

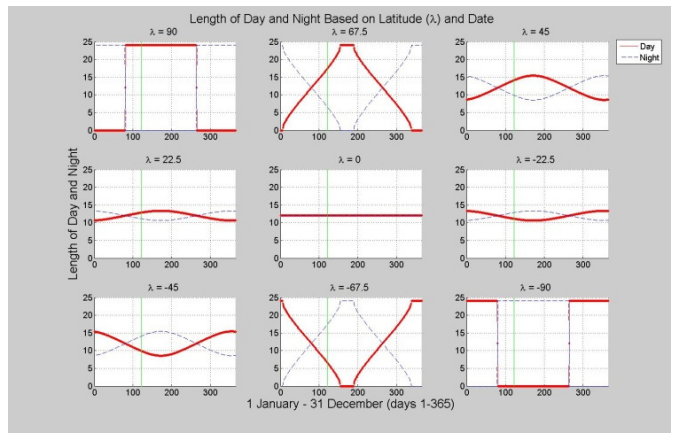

Figure 3. Duration of Daytime and Nighttime for an Entire Year for Various Latitudes l (Vertical green line represents the date May 2, 2012)

The duration of daytime was used in computing the efficiency of reduced-degree-of-freedom solar tracking systems in the next section.

Efficiency of Solar Tracking Systems with Reduced Degree of Freedom

In some applications, the efficiency of the solar panels is traded for the lower cost of the tracking system. Single-axis trackers are widely used in lieu of dual-axis trackers. The single axis can be horizontal, vertical or tilted. Using the model developed in this study, an estimation of the efficiency of these single-axis trackers can be computed when the engineers need to evaluate the trade-offs.

The solar panel efficiency due to sunlight incident angles is the only concern here. The efficiency due to incident angles of solar panels with reduced degrees of freedom is defined to be the ratio of the energy flux per unit area per day of such a solar panel to the energy flux per unit area per day

of dual-axis full solar tracker. Do not confuse this efficiency definition with efficiency of photoelectric energy conversion, which in general is less than 40%. The numerical values of the efficiency due to sunlight incident angles are much higher, but this fact does not imply any contradiction. This efficiency may vary each day in the year, but what is of particular interest is the annual average, or the seasonal average, of the efficiency. It may vary with local latitude as well. The efficiency in numerical values for New York City, as an example, which has latitude λ = 40º47', is calculated throughout this analysis. At the end of this section, the efficiencies are compared with two other locations with different latitudes, Los Angeles, CA, and Miami, FL. With this analysis, it makes it easier to estimate quantitatively how much gain in power the full tracking system may obtain compared to less-expensive partial tracker systems or even seasonally adjusted fixed solar panels. This will assist with the decision-making process on the difference choices of solar panel systems in the investment and installation of such systems.

Efficiency of Seasonally Adjusted Fixed Panel Systems

One simple improvement related to efficiency, on top of the fixed solar panels, is to seasonally adjust the tilt angle of the solar panel manually. Solar panels with dual-axis trackers and with programmed active drives, as discussed in the last section, are able to guarantee the orthogonal incident of sunlight all the time and are the most efficient. The seasonally adjusted fixed panel systems are always oriented to face due south. In the spring and fall, the tilt angle is adjusted to face the celestial equator, with an altitude angle λ, which is the local latitude.

For six months of the year, the duration of daylight is longer than 12 hours. However, the usable time for the incident sunlight is truncated at 12 hours because the sun is behind the panel for the rest of the day. For the other six months, the duration of daylight is less than 12 hours. So for three months in the summer, the incident sunlight is 12 hours long. For spring and fall there are one and half months with 12 hours of sunlight and one and half months with less than 12 hours. For winter, it is always less than 12 hours.

Summer

Assume that in summer the panel tilt is adjusted to a declination angle $\bar{\sigma} = \frac{3\varepsilon}{4}$. The average incident angle is taken as $\frac{\varepsilon}{8}$. In the three months of summer, the sunlight is longer than 12 hours. While a full tracker can take advantage of this fact, the fixed panel has to truncate the sunlight to 12 hours. The fixed panel only makes use of a portion of sunlight during the day, which is $\frac{12}{\bar{d}}$, where $\bar{d}$ is the average duration of daytime.

$$\bar{d} = 24[1-(\cos^{-1}(\tan(\frac{3\varepsilon}{4}).\tan\lambda))/\pi] \tag{16}$$

The efficiency for summer is, then,

$$\frac{12}{\bar{d}}(\cos\frac{\varepsilon}{8})\frac{1}{\pi}\int_{-\frac{\pi}{2}}^{\frac{\pi}{2}}\cos\varphi d\varphi \tag{17}$$

The efficiency varies with local latitude because the average duration of daylight depends on the latitude. For New York City, for example, with the latitude λ = 40º47', the efficiency is 53.97%.

Spring and Fall

For spring or fall, the solar panel is adjusted to aim at the vernal equinox or autumnal equinox, thus the efficiency for spring and fall is the same, due to symmetry. Here, only the analysis for the spring is described.

For the 1.5 months of spring with more than 12 hours of daylight, the average duration of daylight is

$$\bar{d} = 24[1-(\cos^{-1}(\tan(\frac{\varepsilon}{4}).\tan\lambda))/\pi] \tag{18}$$

The efficiency can be approximated by

$$\frac{12}{\bar{d}}(\cos\frac{\varepsilon}{4})\frac{1}{\pi}\int_{-\frac{\pi}{2}}^{\frac{\pi}{2}}\cos\varphi d\varphi \tag{19}$$

For New York City, with the latitude λ = 40º47', in this period, the efficiency is 59.7%.

For the other 1.5 months of spring, the average duration of daylight must be considered, which depends on the local latitude. For the first-order approximation, take the average declination as

$$\bar{\sigma} = -\frac{\varepsilon}{4} \tag{20}$$

The efficiency of the solar panel for these 1.5 months is

$$(\cos\frac{\varepsilon}{4})\frac{1}{\pi}\int_{-\frac{\pi}{2}}^{\frac{\pi}{2}}\cos\varphi d\varphi \tag{21}$$

which has a numerical value of 63.3%. The overall average efficiency for spring and fall is 61.5%.

Winter

During the three winter months, the daylight time is less than 12 hours. Take the average declination as

$$\overline{\sigma} = -\frac{3\varepsilon}{4} \tag{22}$$

and the average incident angle of sunlight as $\frac{\varepsilon}{8}$.

The solar panel efficiency for winter is approximately

$$(\cos\frac{\varepsilon}{8})\frac{1}{\pi}\int_{-\frac{\pi}{2}}^{\frac{\pi}{2}}\cos\varphi d\varphi \tag{23}$$

which is calculated to be 63.6% for New York City.

Efficiency of Horizontal Single Axis Trackers (HSAT)

HSAT trackers have horizontal axes. These trackers are able to follow the altitude of the sun but not the azimuth from east to west. There is limited improvement from seasonally adjusted fixed panels. They suffer in the same way as fixed panels in the summer and half of spring and half of fall to utilize the periods of longer than 12 hours of sunlight. The efficiency in winter is

$$\frac{1}{\pi}\int_{-\frac{\pi}{2}}^{\frac{\pi}{2}}\cos\varphi d\varphi \tag{24}$$

which is 63.7%.

The efficiency in the summer is

$$\frac{12}{\overline{d}}\frac{1}{\pi}\int_{-\frac{\pi}{2}}^{\frac{\pi}{2}}\cos\varphi d\varphi \tag{25}$$

The average daylight is the same in summer

$$\overline{d} = 24[1-(\cos^{-1}(\tan(\frac{3\varepsilon}{4}).\tan\lambda))/\pi] \tag{26}$$

For New York City, with a latitude λ = 40º47', the efficiency turns out to be 54.0%.

For half of the spring, which is right before summer, the average daylight time is

$$\overline{d} = 24[1-(\cos^{-1}(\tan(\frac{\varepsilon}{4}).\tan\lambda))/\pi] \tag{27}$$

and the efficiency is 60.2%. The average efficiency for the other half of the spring, which is immediately after winter, is 63.7%. The overall efficiency for spring or fall is, then, 62.0%.

Efficiency of Tilted Single Axis Trackers (TSAT)

In these trackers, the axis is tilted so that at noon the panel is facing the intersection of the celestial equator on the local meridian. The panel rotates daily from east to west to follow the sun. The incident angle is fixed for each day and is the same as the solar declination angle σ. The annual average efficiency for this TSAT is

$$\frac{1}{2\varepsilon}\int_{-\varepsilon}^{\varepsilon}\cos\sigma d\sigma \tag{28}$$

which is independent of the local latitude and has a value of 97.2%.

Efficiency of Vertical Single Axis Trackers (VSAT)

VSAT trackers can rotate along a vertical axis and follow the sun from east to west daily. These tracers make full use of longer daytime during the summer. Suppose the panel is optimally oriented in such a way that it faces the celestial equator at noon, the efficiency of VSAT trackers would be calculated as

$$\frac{1}{\varepsilon}\int_{0}^{\varepsilon}\frac{1}{2\alpha+\sigma}\int_{-\alpha}^{\alpha+\sigma}\cos\theta d\theta d\sigma \tag{29}$$

where $\alpha = \frac{\pi}{2} - \lambda$ is the co-latitude.

This can be approximated as

$$\frac{1}{\alpha}\int_{0}^{\alpha}\cos\theta d\theta \tag{30}$$

resulting in an efficiency of 88.2% for New York City.

The efficiencies for two other cities, Los Angeles, CA, and Miami, FL, are calculated and compared in the following tables. Los Angeles has a latitude λ = 34º03', and Miami has a latitude of λ = 25º46'.

Table 1. Efficiencies for Seasonally Adjusted Fixed panels

	SAF summer	SAF spring or fall	SAF winter
New York	54.0%	61.5%	63.6%
Los Angeles	55.9%	62.0%	63.6%
Miami	57.8%	62.3%	63.6%

Table 2. Efficiencies for Horizontal Single Axis Trackers

	HSAT summer	HSAT spring or fall	HSAT winter
New York	54.0%	62.0%	63.7%
Los Angeles	56.0%	62.4%	63.7%
Miami	57.9%	62.7%	63.7%

Table 3. Efficiencies for Tilted Single Axis Trackers and Vertical Single Axis Trackers

	TSAT	VSAT
New York	97.2%	88.2%
Los Angeles	97.2%	84.8%
Miami	97.2%	80.5%

Conclusions

The analysis of the diurnal motion of the sun on the celestial sphere using a geocentric model was used for an active dual-axis solar tracker in order to optimize the incident angle and, hence, optimize the received energy flux from the sunlight. The numerical values of the declination angles and azimuthal angles of the sun, sunrise, sunset time, and duration of daytime for any date in the year, and conducted simulations for various locations with different latitude and dates in a year were calculated. Solar panel efficiency due to incident angles for restricted-degree-of-freedom solar trackers for different seasons and the annual average were also analyzed. The results indicated that the tilted single-axis trackers (TSAT) have the highest efficiency, which is independent of the local latitude. The horizontal single-axis trackers do not offer significant improvements over the seasonally adjusted fixed panels. This analysis has significance in providing guidance in the decision-making process of initially installing a solar panel system. In summary, this paper presents not only a visual tool but also a computational tool to assist engineers and consumers in their decision making for investment in appropriate solar panels and tracking systems in terms of trade-offs for energy maximization in their particular applications.

References

[1] Green, M. A., Emery, K., Hishikawa, Y., & Warta W. (2009). Solar Cell Efficiency Tables (Version 34). *Progress in Photovoltaics: Research and Applications,* 17, 320–326. (Published online in Wiley InterScience (www.interscience.wiley.com) DOI: 10.1002/pip.911)

[2] Ning, K., Chen, J., Yu, T., Zhou, G., Chen, X., & Yu, G. (2011). Design of the Attitude Automatic Adjusting System for the Solar Panel. *Proceedings of the 2011 IEEE 2nd International Conference on Computing, Control and Industrial Engineering (CCIE),* (pp. 367-370). (dio: 10.1109/ CCIENG.2011.6008035)

[3] Chen, Y. M., & Wu, H. C. (2001). Determination of the Solar Cell Panel Installation Angle. *Proceedings of the 2001 4th IEEE International Conference on Power Electronics and Drive Systems,* (pp. 549-554).

[4] Mokhtari, B., Ameur, A., Mokrani, L., Azoui, B., & Benkhoris, M. F. (2009). DTC Applied to Optimize Solar Panel Efficiency. *Proceedings of the 35th Annual IEEE Conference on Industrial Electronics*, *IECON '09*, (pp. 1122-1127). (doi: 10.1109/ IECON.2009.5414681)

[5] Oltu, O., Milea, P. L., Dragulinescu, M., & Franti, E. (2007). Solar Panel Energetic Efficiency Optimization Method, Based on a Specific Detector and Orientation Microsystem. *Proceedings of the IEEE International Semiconductor Conference, CAS 2007,* (pp. 127-130).

[6] Rizk, J., & Chaiko, Y. (2008). Solar Tracking System: More Efficient Use of Solar Panels. *World Academy of Science, Engineering and Technology*, 41, 313-315.

[7] Li, D. H.W., & Lam, T. N. T. (2007). Determining the Optimum Tilt Angle and Orientation for Solar Energy Collection Based on Measured Solar Radiance Data. *International Journal of Photoenergy*, Article ID 85402, 1-9 (doi:10.1155/2007/85402)

[8] Xu, J., Wu, K., & Ma, L. (2009). All-Weather Automatic Solar Tracking Method Applied in Forest Fire Prevention. *Proceedings of the 9th International Conference on Electronic Measurement & Instruments, ICEMI'2009,* (pp. 1-805 – 1-809).

[9] Kuo, J. L., Chao, K. L., & Lee, L. S. (February 2010). Dual Mechatronic MPPT Controllers with PN and OPSO Control Algorithms of the Rotatable Solar Panel in PHEV System. *IEEE Trans. Industrial Electronics,* 57(2), 678-689.

[10] Chen, Y. M., Lee, C. H., & Wu, H. C. (June 2005). Calculation of the Optimum Installation Angle for Fixed Solar-Cell Panels Based on the Genetic Algorithm and the Simulated-Annealing Method. *IEEE Transactions on Energy Conversion,* 20(2), 467-473.

[11] Lu, W. H., & He, X. L. (December 2008). Development of Full-Automatic Solar Tracker and Its Application. *Optics and Precision Engineering*, 16(12), 2544-2550.

[12] Dousoky, G. M., El-Sayed, A. H. M., & Shoyama, M. (2011). Maximizing Energy-Efficiency in single-Axis Solar Trackers for Photovoltaic Panels. *Proceedings of the 8th IEEE International Conference on Power Electronics - ECCE Asia*, (pp. 1458-1463). The Shilla Jeju, Korea.

[13] Chang, Y. (2011). Vehicle Profile Design versus Solar Energy Collection: Styling Considerations for Solar-powered Personal Commuter Vehicles. *International Journal of Engineering Research & Innovation*, 3(1), 15-24.

[14] Soares, A., Li, C. (2011). Using Solar Energy in Robotics and Small-Scale Electronic Applications. *International Journal of Engineering Research & Innovation*, 3(2), 27-30.

[15] Tango, R. W. (2009). Technology Integration into Architecture Building Systems. *Technology Interface International Journal*, 10(2), 1-15.

Biographies

HONGYU GUO is an Assistant Professor of Computer Science at University of Houston – Victoria. He received his Ph.D. degree in Computer Science from the University of Florida. His research interests are in computer vision, simulation and image processing. Dr. Guo may be reached at guoh@uhv.edu.

MEHRUBE MEHRUBEOGLU is an Associate Professor of Mechanical Engineering and Engineering Technology at Texas A&M University-Corpus Christi. She earned her B.S. degree in Electrical Engineering from The University of Texas at Austin, MS degree in Bioengineering from Texas A&M University, and Ph.D. degree in Electrical Engineering from Texas A&M University. Dr. Mehrubeoglu's interests lie in imaging and image processing applications, instrumentation, optical property measurements, and renewable energy. She can be reached at ruby.mehrubeoglu@tamucc.edu.

MECHANICAL DESIGN OF A STANDARDIZED GROUND MOBILE PLATFORM

Nina P. Robson, Texas A&M University; J. Morgan, Texas A&M University; H. Baumgartner, Texas A&M University

Abstract

The paper summarizes the mechanical design of a Standardized Ground Mobile Platform (SGMP) with special attention on the development of a novel type of passive suspension. The suspension mechanism consists of two planar closed kinematic chains on each side of the rover. The design considered here was simpler than existing passive suspension mechanisms in the sense that the number of links and joints have been significantly reduced, without compromising the climbing capability of the rover.

Background

The first planetary exploration rovers, Lunakhod 1 and 2, each visited the moon to gather information and send pictures of the terrain. In 1996, NASA's Jet Propulsion Lab and the California Institute of Technology designed new rovers with identical structures; they were named Sojourner and Marie-Curie and weighed about 10.5kg. [1], [2]. The Rocky 7 design and dimensions are similar to Sojourner. As wheeled robots evolved, the mobility system changed from two-wheel steering systems to Ackerman type [3]. Rough-terrain mobility can be increased by shifting the center of gravity. A good example of this is the NASA Sample Return Rover (SRR), which was designed for missions on Mars and has an active suspension system with variable angles between linkages [4]. Shrimp is a six-wheeled rover, designed by the Swiss Federal Institute of Technology. It has one front four-bar linkage to climb over obstacles up to twice its wheel diameter without stability problems. The middle four wheels have parallelogram bogie, which balances the wheels' reaction forces during climbing [5]. Mars Exploration rovers were designed on the basis of Sojourner. Each of them is about 1.6 meters in length and weighs 174kg. The mobility system uses a rocker-bogie suspension and four-wheel steering [6]. Tao et al. [7] presented the design of a six-wheeled robotic rover with passive/active suspension for uneven terrain. The rover suspension consists of two articulated frames, each with three degrees of freedom (DOF) and where each joint of the suspension can rotate passively or be driven by a motor. Singh et al. [8] aimed to design a suspension mechanism which would utilize the advantages of both passive-suspension and active-suspension rovers. As future space exploration, rescue and other missions include the principle of reducing costs, new, more flexible rover designs will be needed. This need provides a number of highly motivational educational and research opportunities for design, development, and testing of new small-form–factor, ground-based robots.

Concept of Operation

The overall goal that was set for the multidisciplinary development team was two-fold. Electronically, the system had to be manageable from a remote location and be capable of adding/upgrading sensor and control technologies through a slice-based architecture. Mechanically, the system had to be low cost, small, compact, highly maneuverable, and be able to be fabricated and maintained with a minimum investment in tools/materials. An overview of the concept of operation of SGMP is shown in Figure 1. As the figure indicates, the system architecture is Internet–based, thus allowing for monitoring and control of the robot from anywhere that an Internet connection could be secured. The heart of the system is the MySQL Server. This resource accepts route-planning inputs from a Base Station as well as collects geographical positioning and other sensory information from the robot. Route planning information is downloaded from the server to the robot, while information sent from the robot to the server can be transferred to a Base Station that requests this information. The server can also record route generation and tracking data for later playback and analysis.

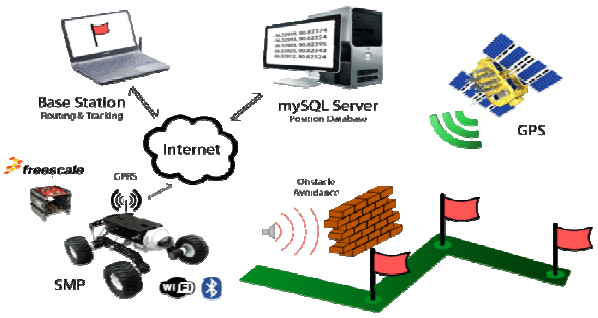

Figure 1. SGMP Concept of Operation

The SGMP robot has the ability to connect to the server via a wireless Wide Area Networking link using GPRS. In addition to the GPRS communications, the robot can use

either Bluetooth or wireless Local Area Networking to communicate locally. The robot uses ultrasonic detection for collision avoidance and has both GPS and AHRS to assist in path following. The mobile platform uses a Freescale Tower architecture to provide the on-board, slice-based command, control, and communications functions. The hardware/software infrastructure of the vehicle is based on subsumption architecture, which is a way of decomposing a complex behavior into "simple" modules [9]. The robot was intended to operate in an urban-type environment with the ability to avoid large obstacles and negotiate uneven terrain.

Mechanical Design of a Novel Articulated Suspension

The mechanical design for the SGMP was developed with the main goal of improving the size, maneuverability, and suspension of existing Surface Mobility Platforms (SGMP) [10]. In four-wheel-drive vehicles, obstacle limit is generally half of the wheel diameter [1]. It is possible to pass over this height by pushing the driving wheel to the obstacle, which is called climbing. For this condition, the contact point of the wheel and obstacle is at the same height as the wheel center. Although obstacle geometries can vary, the most difficult geometry which can be climbed by a wheeled vehicle is a stair-type rectangular obstacle. For that condition, climbing motion consist of two sub-motions. The first is a vertical motion, which causes a horizontal reaction force on the wheel center. The vertical motion instant center is at infinity. The second sub-motion is a soft rotation about a point located at the top of an obstacle, with an instant center of rotation at that point. Tests show that the Mars rover is able to overcome about 1.5 times the height of its wheel diameter. This limitation forces scientists to improve their current designs.

Climbing over an obstacle is a critical problem when wheel forces in the opposite direction of motion produce a moment about a pivot joint to rotate the bogie [3]. If the surface friction of an obstacle is not enough to climb, the obstacle force on the wheel can reach high values. A solution for this problem is the use of a linear-motion suspension where obstacle reaction force cannot create any moment.

Based on all of these factors, the challenge in this current study was to design a suspension which would: 1) be simple in structure, 2) allow for a near to straight line motion of the center of the wheel in order to decrease overturn moment, 3) have a climbing capacity of about two times the wheel diameter, and 4) have the ability to maintain equal force and maintain equal load distribution on all wheels. Therefore, the goal of this kinematic synthesis was to calculate the design parameters for the linkage suspension that accounts for the physical contact of the wheel with an obstacle in the workspace during motion. For the synthesis, the authors defined a start and an end position and used velocity and acceleration task specifications defined in the two positions, which are directly derived from the geometry of the problem [11] and are compatible with contact and curvature constraints of the wheels with obstacles in the environment. After the task was specified, the dimensions of the chain, which would satisfy the task specifications, were calculated. A four-bar linkage was synthesized to obtain the desired approximate straight-line motion of the wheel center. The suspension on each side of the platform was constructed by connecting two four-bar linkages symmetrically. Figure 2 shows two of the five designs that best fit the requirements [11]. Tests were performed to assure that each suspension moved smoothly throughout the task.

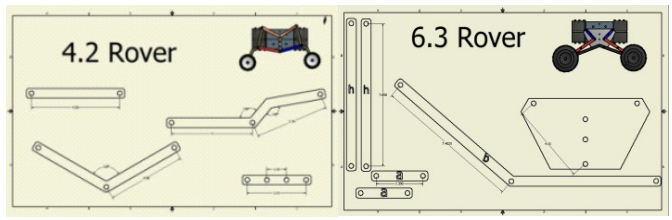

Figure 2. Linkage Type and Link Lengths for Each Design

Because the proposed bogie design was to be symmetrical, reaction forces of the front and rear wheels were identical. During operation on rough terrain, if the robot can maintain its balance at all times, even when frozen position, it can be said that the robot has static stability. Physically, the boundary for stability criteria is related with a polygon, which consists of contact points between the ground and the wheels [12]. If the projection of the center of gravity on the ground plane stays inside of the stability area at all times during operation, the robot is considered to be stable. The stability of the robot can be defined by using the gravitational stability margin [13].

The maximum slope of the terrain that the robot can climb is called gradeability, The maximum downhill and cross-hill gradeability can be easily calculated and are functions of the projection of the center of gravity on the slope and its distance to the wheels. Since the center of gravity is sufficiently low for all design models, the coefficient of friction of the wheels would be the next limiting factor when traversing a sloped surface. For that reason, hollow rubber wheels were chosen. Each rubber wheel was mounted on a plastic hub and was additionally secured by an adhesive along the circumference of the hub. The wheels were non-pressurized and could deform and return to their shape, providing uniform, low-maintenance traction. A diameter of 3 inches was chosen for the wheels. Wheel width contributes to traction as a factor of the ground surface area dis-

placing the normal force on each wheel. In challenging environments such as sand, wider wheels aid in preventing the unit from sinking into the shifting soil.

Development concepts for each rover design had an approximate size of 14”x14”x14” and a weight of 14 pounds for the five different suspension designs. The two top designs are shown in Figure 3. They were tested using three primary criteria: 1) obstacle climbing ability of the suspension; 2) linear motion capacity of the suspension; and, 3) platform-suspension system stability in climbing slopes. These criteria are described below.

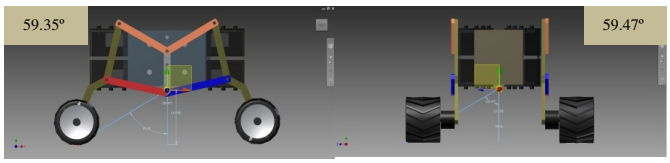

a) Design Model 4.2

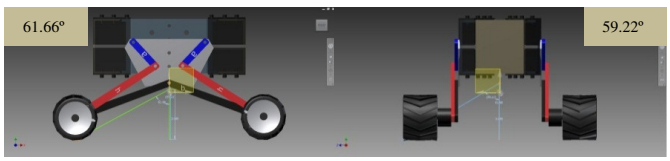

b) Design Model 6.3

Figure 3. Center of Gravity for the Top Two Designs

Obstacle Climbing Ability and Linear Motion Capacity of Suspension

In order to quantify the desired linear motion of each of the linkage systems, the maximum displacement of the wheel center in the *x* direction was calculated. The displacement of the value for the *y* direction gave insight into the maximum height of an object that the platform could overcome. Design 4.2, shown on the left in Figure 4, meets and exceeds the goal of 1.5 times the wheel diameter climbing height, while minimally diverging in the *x* direction late in its path.

The trajectory of the center of the wheel of design 6.3 (Figure 4 to the right) follows a circular path proportional to the length of input crank *b* and its travel is restricted by output crank *a* and coupler *h*. These yield semi-vertical travel within the range of actuation, increasing in linearity as the length of *b* link increases.

Center of Gravity and System Stability

The maximum slope, or gradeability, was broken into two perspectives (see Figure 3). Design 4.2 (Figure 3a), has a wheel base well outside of the body, resulting in a good gradeability. The center of mass is higher than some of the other designs, but only a few degrees of the cross-hill gradeability is traded for the greater ground clearance. While design model 6.3 (Figure 3b) seems to have respectable gradeability and cross-hill gradeability, there is a fundamental stability issue with the geometry. Since the linkage system would be pivoting about the center fastening point, there would be a need for a secondary set of linkages in order to add stability.

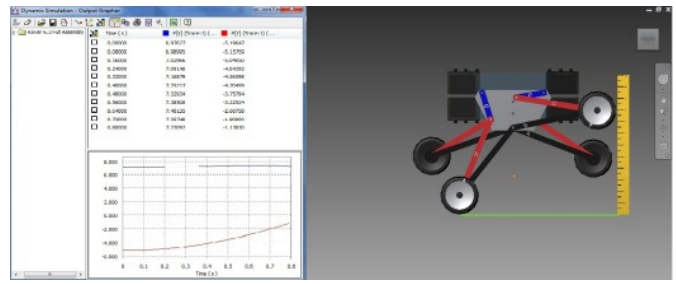

a)

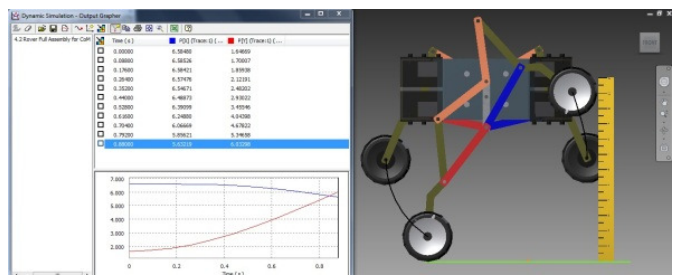

b)

Figure 4. Climbing Ability of the Top Two Designs

Design model 4.2 was chosen as the best overall design based on its climbing capacity of about 3 times the wheel diameter, and its linear ratio of 0.1. The linear ratio indicates the ratio of *x_max* displacement over the total *y* displacement from the ground, which is close to a straight line for this design. Even though the linkages were sized to accommodate this height, the center of mass was maintained low enough to offer a forward climbing angle (gradeability) of 59.35º, (Figure 5, right) and a cross-hill gradeability of 59.47º, (Figure 5, left).

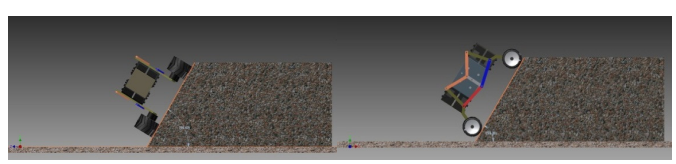

Figure 5. Gradeability for Design 4.2

The kinematic analysis of the suspension uses the idealization that the links do not flex during movement and can be considered as rigid. The constraint equation (1) of a general four-bar linkage can be used for deriving the output angle Y as a function of a known input angle Q (see Figure 6). The constraint equation is obtained from the requirement that the coupler link maintains a constant distance between the moving pivots of the input and output cranks [14]:

$$C: \quad (\mathrm{B} - \mathrm{A})\ (\mathrm{B} - \mathrm{A}) - h^2 = 0 \qquad (1)$$

where

$$\mathbf{A} = \begin{Bmatrix} a\cos\theta \\ a\sin\theta \end{Bmatrix} \text{ and } \mathbf{B} = \begin{Bmatrix} g \\ 0 \end{Bmatrix} + \begin{Bmatrix} b\cos\psi \\ b\sin\psi \end{Bmatrix}$$

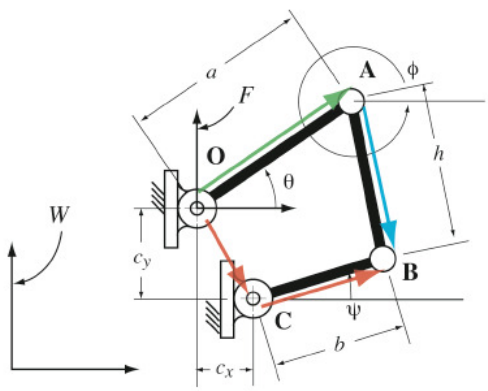

Figure 6. Four-Bar Linkage Configuration

Differentiation of this constraint yields the speed ratio of the linkage, which defines its mechanical advantage in a particular configuration. For a given input angle and a known value of the output angle, the position loop equations are solved to determine the coupler angle:

$$\phi = \arctan\left(\frac{b\sin\psi - a\sin\theta}{g + b\cos\psi - a\cos\theta}\right).$$

The first derivative of the loop equations of the four-bar linkage defines the velocity loop equations, which are used to compute the angular velocities of the output crank and coupler link. It was assumed that the input crank of Design 4.2. would move with a constant velocity of 1deg/s. The locations of the fixed pivots **O** and **C** and moving pivots **A** and **B** with respect to a fixed frame W, as well as the link lengths, were obtained to be **a** = 4, **b** = 4.5, **h** = 3.85. The offsets were cx = 0 and cy = -3 (see again Figure 6). The results from the kinematic analysis for different input crank angles Q, in the range of 30° to 90°, are given in Table 1.

Table 1. Results from the Kinematic Analysis

Q° In. angle	Y° Out. angle	F° Coupler angle	• Q(deg/s) in. vel.	• Y (deg/s) out. vel.
30	16.09	-77	14.33	-37.36
40	24.44	-74.4	16.15	-29.15
50	32.45	-71.4	18.48	-19.16
60	40.04	-67.9	21.35	-7.41
70	47.16	-63.9	24.75	5.76
80	53.75	-59.2	28.60	19.57
90	59.76	-53.9	32.74	32.74

Figure 7 shows the SGMP undergoing a number of tests. The chassis and suspension were primarily constructed from 6061 Aluminum, which was chosen for its light weight and availability in various extruded profiles. Each piece was drilled manually using a Bridgeport vertical mill, which had been fitted with a digital x and y readout. In order to couple each motor to the legs, a two-piece adapter was modeled in 3D and then printed in ABS plastic, using a Stratasys FDM 200MC rapid prototyping machine. This method was also used to create the module, which holds each level of circuit boards.

Figure 7. The Standardized Ground Mobile Platform (SGMP)

Conclusions

The mechanical design of the Standardized Ground Mobile Platform (SGMP) was discussed with special attention on the development of a novel type passive suspension mechanism. Different designs were analyzed based on a number of system requirements. The advantages of the final design are its linear motion, ability to overcome obstacle capacities, stability in climbing either uphill or downhill, as well as compact size and low cost. The platform employs an open-electronics hardware and software architecture. The working prototype of the new design was discussed and presented.

References

[1] Fiorini, P. (2000). Ground Mobility Systems for Planetary Exploration. *Proceedings of the IEEE-ICRA Conference*, (pp. 908-913).

[2] Bonitz, R. G., Nguyen, T., & Kim, W. (2000). The Mars Surveyor'01 Rover and Robotic Arm. *Aerospace Conference Proceedings*, *IEEE,* (7, pp. 235-246).

[3] Volpe, R., Balaram, I., Ohm, T., & Ivlev, R. (1997). Rocky 7: A next Generation Mars Rover Prototype. *Journal of Advanced Robotics,* 11(4).

[4] Iagnemma, K., Rzepniewski, A., Dubowski, S., Pirjanian, P., Huntsburger, T., et al. (2000). Mobile Robot Kinematic Reconfigurability for Rough Terrain. *Proceeding of the SPIE ISISAM Conference.*

[5] Siegwart, R., Lamon, P., Estier, T., Lauria, M., & Piguet, R. (2002). Innovative Design for Wheeled Locomotion in Rough Terrain. *Robotics and Autonomous Systems*, 40, 151-162.

[6] Mars Exploration Rover Landings Press Kit (2004, January). National Aeronautics and Space Administration (NASA). Retrieved from http://www.scribd.com/doc/48830087/Mars-Exploration-Rover-Landings-Press-Kit

[7] Tao, J., Yang, F., Deng, Z., & Fang, H. (2011). Kinematic Modeling of a Six-wheeled Robotic Rover with a Passive/Active Suspension. *9th World Congress on Intelligent Control and Automation*, (pp. 898-903).

[8] Singh, A., Eathakota, V., Krishna, K., & Patil, A. (2009). Evolution of a four wheeled active suspension rover with minimal actuation for rough terrain mobility, *Proceeding of the IEEE International Conference on Robotics and Biomimetics*, (pp. 794–799).

[9] Morgan, J., Wright, G., Robson, N. P., Baumgartner, H., & Lopez, J. (2011). Development of a Standardized Ground Mobile Platform for Research and Education. *Proceedings of the AUVSI Unmanned Systems North America*, Washington DC.

[10] Surface Mobility Platform: A Rugged Robotics Research Platform that is Agile and Easy to Maintain. (2007). Gears Educational Systems, LLC. *Illustrated Assembly Guide*. Retrieved from http://www.gearseds.com/files/SMP_construction_guide_finalrev8%20(3).pdf

[11] Robson, N., & McCarthy, J. M. (2007). Kinematic Synthesis with Contact Direction and Curvature Constraints on the Workpiece. *Proceedings of the ASME IDETC Conference*, Las Vegas, NV.

[12] Dudek, G., & Jenkin, M. (2001). *Computational Principles of Mobile Robotics*. Cambridge University Press.

[13] Apostolopoulos, D. S. (2001). *Analytical Configuration of Wheeled Robotic Locomotion*. Ph.D dissertation, the Robotics Institute, Carnegie Mellon University, Pittsburgh, PA.

[14] McCarthy, J. M. (2000). *Geometric Design of Linkages*. Springer-Verlag, New York.

Biographies

N. ROBSON is an adjunct assistant professor in Engineering Technology and Industrial Distribution at Texas A&M University and an Assistant Researcher in the Mechanical and Aerospace Engineering Department at the University of California, Irvine. Her email address is npatarin@uci.edu.

J. MORGAN is a professor in the Engineering Technology and Industrial Distribution Department at Texas A&M University. His e-mail address is morganj@entc.tamu.edu.

H. BAUMGARTNER is an undergraduate student at Manufacturing and Mechanical Engineering Technology at Texas A&M University. His e-mail address is herbert.baumgartner@neo.tamu.edu

CENTRALIZED VISION-BASED CONTROLLER FOR UNMANNED GUIDED VEHICLE DETECTION

Ravindra Thamma, Leela Mohan Kesireddy, and Haoyu Wang, Central Connecticut State University

Abstract

Traditional track-based Unmanned Ground Vehicles (UGV) cannot deviate from their routes due to this track limitation in their navigation methods. Track limitation has to be overcome in order to render a UGV more flexible. It is desirable to have a UGV move without tracks and have the ability to deviate to and from routine routes in order to have flexibility in tasks. In this study, the authors proposed a navigation system to aid multiple UGVs in navigating to various locations without any physical tracks and without colliding with one another. The authors demonstrated an image -recognition-based trackless navigation system to enhance the flexibility of multiple UGVs. To accomplish this feat, an image-recognition algorithm was developed to identify the position and orientation of multiple UGV's using a Centralized Image-Based Controller Unit (CIBCU). This CIBCU is connected to a vision system and radio-frequency (RF) communicator. The CIBCU then implements the image-recognition algorithm, anti-collision and navigation algorithm, and centralized control center to track and navigate multiple UGVs without physical tracks. A prototype was developed to demonstrate and test the Vision-Based Navigation System. Statistical analyses were carried out on this newly developed system in order to find behavior-of-positioning error.

Introduction

Conventionally, controlling Unmanned Ground Vehicles (UGV) and Automatic Guided Vehicles (AGV) has been a challenge. Tracks serve as a key element for navigation systems for a mobile UGV. UGV tracking is a critical component for providing position, directions, and travel information for motion along a trajectory with minimal deviation. Many researchers have proposed different tracking techniques such as dead reckoning, navigation using active beacons, landmark- and map-based navigation, ultrasound, and Global Positioning System (GPS).

Most of the available navigation systems make use of a constant exchange of data between the controller and UGV that is costly in more ways than one. The exchange of data contributes to a slower system, resulting in lower UGV velocity. Furthermore, these systems are complicated by various parts and are often constrained to a pre-defined area. The post-implementation cost can also be a factor against its use. It appears that a newer system that does not carry these drawbacks will be beneficial to this area of study.

Many navigation techniques have been used over the last two decades for tracking a UGV. Dead-reckoning [1] is a process of estimating one's current position based on a previously determined position of the UGV. This is accomplished by advancing a previous position based on a known path and speed over a period of time. However, incremental motion often results in errors. Other navigation systems use active beacons [2] such as laser, sonar, or radio. This technique determines the position of a UGV by drawing a triangle through installed beacons and measuring the distance. The disadvantages of this technique include inaccuracy of distance measurements caused by signal delay, as well as installation and maintenance costs. GPS systems are more advanced and accurate at tracking the position of a UGV, but do not work in an indoor environment where satellite signals are often blocked.

Presently, wireless techniques are extensively used to track the UGV using distance measurement techniques. Radio frequency (RF) and ultrasound [3,4] are extensively used in these navigation techniques. In some cases, both ultrasound and RF are used together for greater precision. All of the aforementioned navigation systems involve a constant exchange of data between the controller and the UGV, resulting in a large amount of overhead, and the employment of more sensors and constraints to the pre-defined landmarks. This results in a higher power consumption and shorter battery life of the UGV. It also results in slower operation and response.

Vision-based navigation systems generally use less data for tracking the UGV position, resulting in faster operation and response. This is different from previous navigation systems like the landmark- and map-based navigation techniques, which rely on predefined landmarks, maps, or pre-information about the environment [5]. No assumptions about the knowledge of the location are made for the vision-based navigation system.

The concept of vision navigation has been in development for the last 20 years [6] in the area of mobile robot naviga-

tion. Even though it was introduced to overcome the disadvantages in the previous techniques, it is implemented in accordance with the previous techniques. In many techniques, vision systems (i.e., cameras) are used to visualize the environment and to guide the robot. Vision systems are used to find and measure the location of 3D structures with respect to a CAD-model [7]. The integration of a CAD model to visual measurement and direct feedback of measurement results to the CAD model is a key aspect for this technique. In other techniques, vision systems are used to generate a three-dimensional (3D) environmental map from data taken with stereo vision [8]. Vision systems are used to develop more precise segmentation. From the obtained segmentation, a 3D environment is built using occupancy grid and floor height maps. In another vision-based technique, vehicle position and orientation are determined using panoramic images [9]. Omni-directional sensors are used for obtaining a 360º field of view. Recognizing landmarks in a panoramic image from a prior model of distinct features in a given environment gives information about the robot's location.

Most of these techniques rely on assumptions based on prior knowledge of the scene. Some researchers have proposed using a vision-based system that functions without any prior knowledge of the scene. In this technique, a stereo -based vision system is built from feature correspondences and 3D information from image sequences of the scene [10]. This method uses two cameras for capturing the image frames at a fixed point in time. One camera is used to capture interface images and a second camera is used to collect the stereo image. The relative position of the camera motion is then estimated by registering the 3D feature points from two consecutive image frames.

There are many different vision navigation techniques proposed by prominent researchers. Various techniques utilize different methodologies to track UGVs with a vision system. Some of the vision techniques use a prior model of the environment [11]. Some of the techniques draw imaginary horizontal and vertical lines to find the position of the vehicle [9]. Other techniques use information from gray-scale images to find the path clearance to navigate the vehicles [12].

Some vision techniques use panoramic imagery. Omni-directional sensors are used in obtaining a 360º field of view, permitting the various objects near a robot to be imaged simultaneously. The robot's location is found by recognizing landmarks in a panoramic image from a prior model of distinct features in a given environment [11] (Guerrero, 2001). Other vision techniques find the position of the vehicle using collective measurement data obtained directly from the raw data of gray-level images. Such data is independent of the 3D surface texture, is measured in dimensional units, and requires no 3D reconstruction. The control schemes are based on a set of "if / then" fuzzy rules with almost no knowledge about the vehicle's dynamics, speed, and heading [12]. In some techniques, robot navigation is calibrated based on navigational lines. The position of a robot is based on extracted straight lines, assuming that the robot moves on level ground. The effect in the image of camera rotation is computed from the homography of a line at infinity. The corresponding vertical lines in two uncalibrated images are then used to compute both the robot heading and a region in the image that corresponds to the free space ahead [11].

One more important feature to be considered in vision navigation is the nature of the vision system. The number and placement of vision-system cameras play an important role in the function and performance of the navigation system. Some techniques utilize vision systems that are placed on the vehicle [13], while in others they are placed stationary in the navigation field [8]. Some techniques have only one vision system, while others utilize multiple vision systems placed at different positions in the navigation system.

Although vision-based navigation systems are designed to overcome the disadvantages of the traditional navigation systems, some still depend on traditional techniques like maps and developing of 3D environments from an image system. When such systems use more than one vision system, this further complicates the implementation of vision-based navigation. A vision-based system must be implemented in such a way as to overcome all of these disadvantages, while navigating on level ground without using any tracks.

All of the aforementioned systems need large infrastructure and software, resulting in complex and costly techniques. They are all dependent on the previous techniques and require some type of assumptions about the environment. Therefore, there is a need for the development of a navigation technique which uses less infrastructure and simpler algorithms. Such a system should provide navigation for multiple vehicles with lower overhead and less software and hardware.

In this study, a Vision-Based Navigation System was developed to navigate a UGV from a given position to a predefined final position based solely on this system. Automated software, developed as a Centralized Image-Based Controller Unit (CIBCU), would run the algorithms for vision processing, orientation, anti-collision, and navigation. It was tested using a prototype of the vision-based navigation sys-

tem and UGVs, and data analysis was carried out on the test data. The goal of this study was to develop a prototype Vision-Based Navigation System to track multiple Unmanned Ground Vehicles.

Methodology

The vision-based navigation system developed in this study involved processing the image generated by the vision system and navigating multiple UGVs such that they would not collide with each other in accordance with a predefined priority. The basic layout of the proposed solution as shown in Figure 1 helps to illustrate the methodology. The vision system generates the images, and sends them to the vision-processing algorithm. The vision-processing algorithm then processes the image and generates the coordinates of each vehicle. The orientation algorithm then processes the orientation of each vehicle using the coordinates generated by the vision-processing algorithm. An anti-collision algorithm checks the probability of collision and stops the UGV according to its priority. The navigation algorithm navigates the vehicles according to the orientation of each vehicle. The data of the navigation are then transmitted to the vehicles using RF communication.

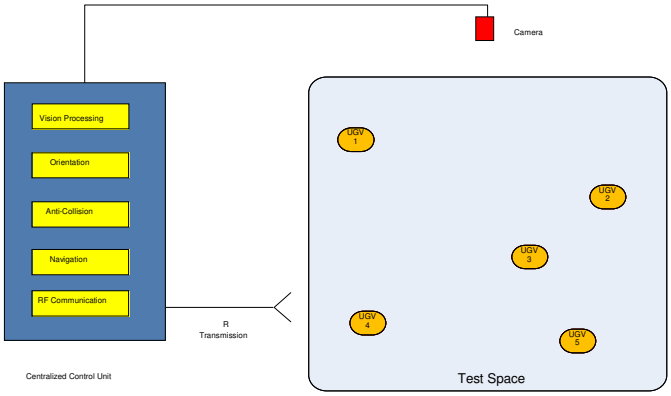

Figure 1. Layout of the Proposed Vision-Based Navigation System

The CIBCU Control Panel is the user interface for operating the vision-based navigation system and works with all five main parts of the system. This control panel provides manual control levers and overriding capabilities to the human user, and has a user-friendly interface that provides user controls for all of the UGVs. The positions of the different UGVs are captured through the vision system camera; these images are then transferred to the vision-processing algorithm. The vision processing system uses the data from the images to provide x and y coordinates for the UGVs. The orientation system calculates the orientation angle of each UGV. The position and orientation information is used by the anti-collision algorithm to find the possibility of any collisions. Finally, the information about the x and y coordinates is fed to the navigation-control algorithm.

The navigation algorithm forms the heart of the entire set up as this system acts as the brain. Navigating all of the UGVs from their present positions to their final positions is the basic responsibility of the navigation algorithm. The RF communication control system handles the transmission of control data to each UGV. A conventional multiplexed radio transmitter serves as the communication medium.

All of the above discussion is developed using a VB.net program. The main function of this program is to navigate the UGVs according to the positions and orientations derived from the latest acquired images. The flow of the program is to acquire the latest image from the vision system, resize and compress the image for faster processing, generate the coordinates of the vehicles by comparing the acquired image with reference images, calculate the orientation of the vehicles from the generated coordinates, and navigate the vehicles to their final positions. This flow is implemented by using the previously described algorithms.

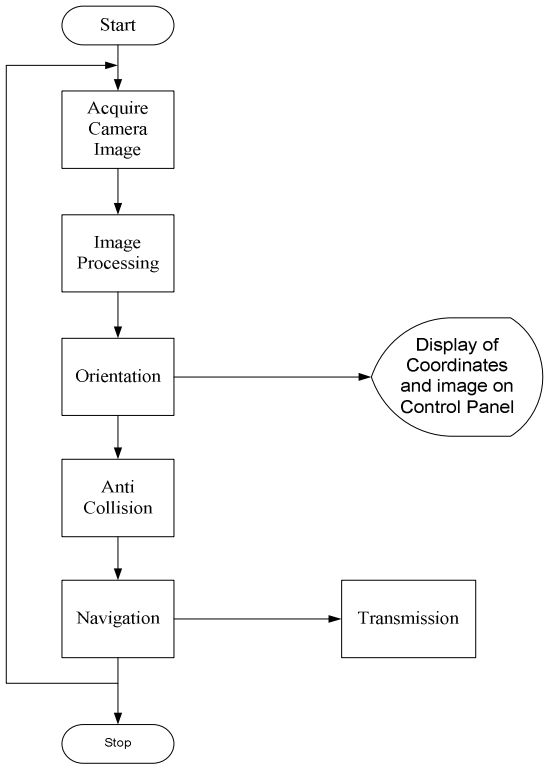

The program is divided into five main parts, based on these algorithms (see Figure 2):

Figure 2. Flowchart for the Vision Navigation Program

RF Communication

The signals from the CIBCU are received by the transmission hardware and send navigation signals to the UGVs for navigation. A Parallax Basic Stamp (BS2SX) microcontroller in the transmission hardware is programmed to receive a signal from the CIBCU and transmit corresponding navigation signals. Transmission hardware is connected to the controller's serial port to receive serial commands, as well as being connected to the RF transmitter to transmit radio signals. The BS2SX microcontroller is capable of receiving and sending serial data.

The BS2SX in the transmission hardware is programmed to receive a unique command and transmit a corresponding unique set of navigation signals. As the BS2SX receives a command from the serial port, it analyses the command using an "if else" loop. Each UGV has a predefined set of signals for navigation of each UGV and some universal signals, which provide specific navigation control for every UGV. Universal signals are in the range of 68 – 99, with 66 being the universal stop command. Table 1 gives the range

UGV Number	Signal Range
1	11 – 15
2	21 – 25
3	31 – 35
4	41 – 45
5	51 – 55

of signals for each UGV.

Table 1. Signal Ranges for Each UGV

The BS2SX program receives a command through a serial input (SERIN) in the form of numbers. The number received is assigned to a variable, which is first checked to see if it falls in the range of universal signals. If the signal falls in the range of universal signals, the corresponding signal is transmitted via the RF transmitter (Figure 9). If the variable is not in the range of universal signals, then it is verified as to which UGV it belongs. Once it falls into a specific UGV range, it then checks for corresponding signals and sends it out. The transmit signal is a combination of three numbers.
The BS2SX receives its commands through the serial port at 9600 baud rates on pin 16, which is connected to the serial port. A PULSOUT signal is sent out to the transmitter to place it in a wake-up state before sending the signal. Then the actual signal is sent out to the transmitter from pin 7. The basic stamp is programmed to receive the signal continuously from the serial port by using a loop.

RF receivers are placed on every UGV to receive the signals. The BS2SX receives the signals through another RF receiver and navigates the UGVs. The receiver on each UGV is connected to a BS2SX, which controls the UGV. All of the UGVs receive all of the signals but only respond to signals assigned to them.

Every UGV has a unique signal for every movement (see Table 2), all of which are preprogrammed on the UGV. The RF receiver on each UGV is always in the wake-up state to receive the signals. It receives every signal at its frequency

UGV -1		UGV -2		UGV -3	
Signal	**Movement**	**Signal**	**Movement**	**Signal**	**Movement**
11	Forward	21	Forward	31	Forward
12	Backward	22	Backward	32	Backward
13	Clockwise	23	Clockwise	33	Clockwise
14	Counterclockwise	24	Counterclockwise	34	Counterclockwise
15	Stop	25	Stop	35	Stop

UGV -4		UGV -5	
Signal	**Movement**	**Signal**	**Movement**
41	Forward	51	Forward
42	Backward	52	Backward
43	Clockwise	53	Clockwise
44	Counterclockwise	54	Counterclockwise
45	Stop	55	Stop

and sends it to the BS2SX for processing.

Table 2. Signals Specific to each UGV

Each Boe-Bot UGV (Figure 3) is programmed for five important movement functions: forward, backward, clockwise, counterclockwise, and stop. The BS2SX sends out the pulses to the servo motors according to the signal it receives. Every UGV is programmed to make uniform move-

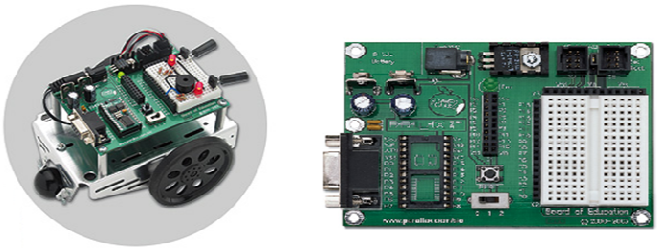

ments. The movement of the UGV is controlled by the PULSOUT signals to the servos. The servos on every UGV are connected to pins 12 and 13 of the BS2SX.

Figure 3. Parallax Boe-Bot and Board of Education

All of the UGVs receive all of the signals transmitted from the transmitter. Once the signal is received by the UGV, the BS2SX on each UGV analyzes the signal it received. If the signal received belongs to that UGV, then it responds with that specific movement.

Centralized Image-Based Controller Unit

The main window of the vision-based navigation system

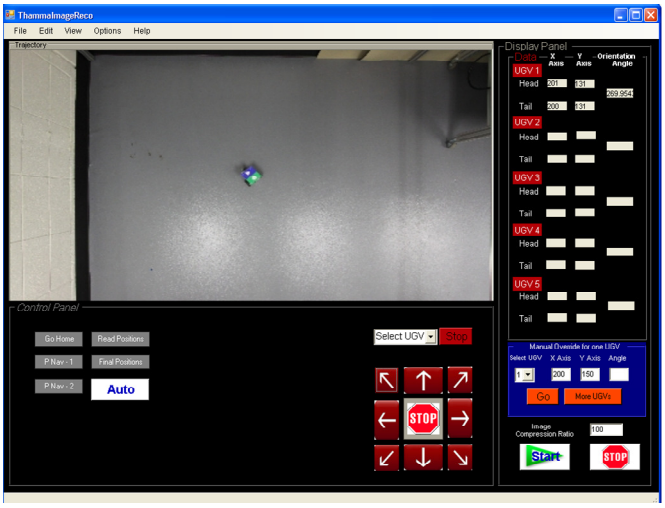

is shown in Figure 4. This screen shows the image of the bots which move relative to the x, y coordinates and the orientation angles for all of the UGVs.

Figure 4. Snapshot of the Main Screen

Test Environment

Verification of this vision-based navigation system was accomplished with a test environment set up to navigate the bots according to the images acquired from the vision system. The setup needed a predetermined space in which the bots were to be navigated, a frame to hold the camera at the top center of the predetermined space, a server to run the program and process the images and send the navigation signals, five UGVs with RF receivers, and transmission hardware.

A test environment was set up with all of the requirements for full verification. The space for the UGV navigation was determined and a frame was built covering the predetermined area and a vision system was hung from the top of the frame. A server with high processing power was used to handle the overhead caused by the program. The vision system and transmission hardware were hardwired to the server. All of the UGV's were given unique labels which had the symbols of the head and tail of each vehicle. Each component of the test environment is discussed in detail below.

The UGVs' test space was the predetermined space (see Figure 5) in which the bots would be navigated. The test space was recognized by the frame built to surround the test area. The frame was built using aluminum bars, and was 8 feet in length, 8 feet wide, and 7 feet high (8'x8'x7'). The frame held the vision system at the top of the mid-center of the predetermined area.

A high-quality vision system was needed to provide robust images of the environment. The vision system had to be capable of capturing images at regular intervals and be capable of operating remotely. The vision system also had to cover the total test space and provide high-quality imag-

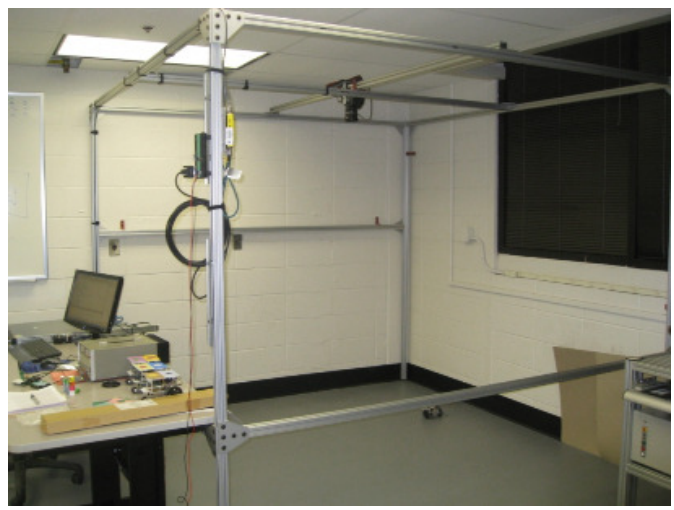

es. A Canon 50D SLR camera was used as it fulfilled all of the above requirements. It was fitted with a wide-angle lens to cover the test area.

Figure 5. Test Space

The vision system was connected to the server using a USB cable. It was operated by the EOS utility provided by Canon. It could be programmed to capture continuous images with a predefined delay between the images and to save them in a specific location on the server. It could also be operated manually. The transmission hardware was built using a Board of Education (BOE) component carrier board, a BS2SX, and an RF transmitter. The BOE provided the interface for the BS2SX to connect to the serial port and to hold the transmitter module. The BS2SX was programmed to receive the signals from the CIBCU and transmit signals using an RF transmitter. The RF transmitter used in this project was a Parallax 433.92MHz RF transmitter module. This module comes with a transmitter chip, an antenna, and

four connection pins. It operates at a baud rate of 12.0k – 19.2k and transmits up to 500 feet.

Testing and Data Analysis

All of the algorithms and programming discussed above were validated by testing in the test environment. At first, synchronization between the different parts of the setup was tested After which the different modes of operation of the program were tested. The vision system was tested for remote shooting by connecting it to the controller and taking test shots. Zoom and focus of the lens were adjusted to cover the whole test area. The vision system can be programmed for different photo formats and image orientation. The vision system was set to save images in the jpeg format with date and time stamps in the specified folder by the user. The vision system was also set to take images in a continuous mode with the image capture interval and number of images being controlled from the remote-control panel.

RF communications of both the transmitter and receiver was tested for functionality. The RF transmission was tested by checking which signal the RF hardware was receiving and which signal it was sending out. The RF receiver was tested by placing a DEBUG code in the receiver program and checking which signals it was receiving. The RF communication was tested by sending signals to the vehicles to move them forward, backward, right, and left. It was tested on all vehicles for continuous signal transmission and transmission range. The synchronization test was conducted to test the synchronization between the controller, vision system, and RF transmission. It was tested by running the program to navigate the vehicles to verify proper performance. It was also tested for all modes of operation and at different speeds of the UGV and camera intervals.

The vision navigation was first tested by the navigation of one vehicle from its present position to a given position. This was done by running the program in the individual-UGV mode. Only one vehicle was placed in the test field and navigated to a final position specified by the coordinates. In this mode, an image was taken and processed and the UGV navigated towards the final position. After every movement in its trajectory, another image was taken and processed to check if the vehicle had deviated from its path. If the vehicle deviated from its original path it was rotated to get it back to its final position. If the vehicle was near the final position within an acceptable tolerance, the vehicle navigation was stopped. The data for every position was recorded automatically in a ".csv" file.

The Vision Navigation test was run continuously ten times by navigating the same UGV between the same start and final positions. All of these data were recorded for subsequent analysis using the save-data option, as seen in Table 3. The x, y coordinates of head and tail orientation of the vehicle for every image were recorded across ten sets of data. The error in the data will be different every time the bots are navigated, thus the mean value was calculated from the ten data sets. These mean data were then plotted to illustrate performance of the system.

Mean Values				
Tail X	**Tail y**	**Head X**	**Head Y**	**Orientation Angle**
170	108	170	105	261
127	58	122	58	266
136	61	130	60	260
144	66	141	65	253
154	74	150	72	244
160	80	152	80	240
187	105	164	85	242
171	93	170	92	245
178	101	178	101	248
203	127	182	107	252
213	136	188	112	258
191	114	192	115	305
229	154	191	122	245
194	130	194	130	258

Table 3. Mean Values Table of Test Data Recorded

Figure 6 is a plot of the mean tail data showing the relationship between the *x* and *y* coordinates. As can be seen, there was not much deviation from the expected path. Figure 7 is

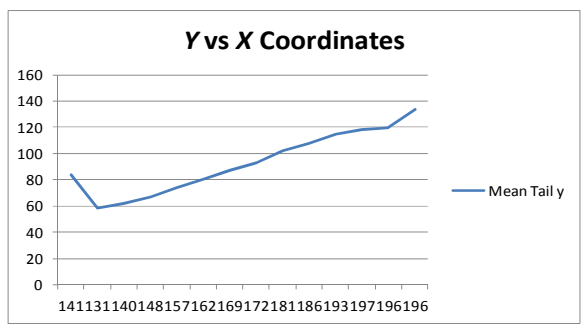

a plot of the mean head data showing the relationship be-

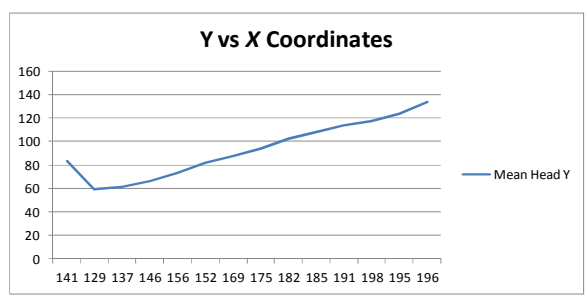

tween the x and y coordinates. There is not much deviation from the expected path.

Figure 6. y versus x Coordinates

Figure 7. y versus x Coordinates

Figure 8 is a plot of the mean orientation data showing the deviation from expected values of the orientation angle. The orientation angle graph should also be a straight line. However, it was observed that the UGVs deviated from their expected path. The deviation was the effect of a change in

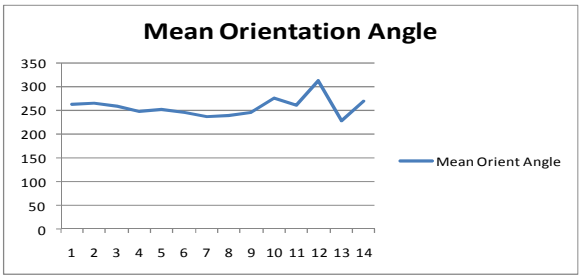

the coordinates on heads and tails of the vehicles. Furthermore, the deviation was only in the area indicated in the graphs. This is because most of the deviation in the orientation angle was dependent on both head and tail coordinates.

Figure 8. Deviation in Orientation Angle

Figure 9 is a plot of the data calculated from the mid-

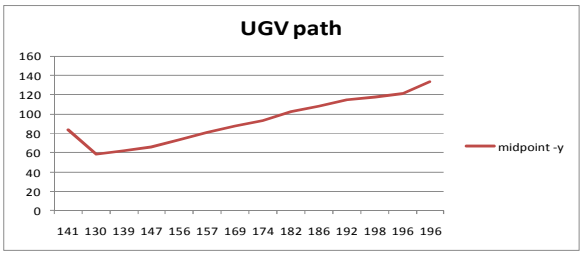

points of the mean data to illustrate the deviation from expected values. This graph gives the actual path of the bot. There is not much deviation as the UGV moved from its present position to its final position.

Figure 9. Deviation in UGV Path

Conclusions

The implementation and testing of this vision-based navigation system allowed for some conclusions to be drawn, which would have a positive effect on the efficiency of the system. Efficient operation of the vision-processing system results in better operation of the navigation system. Thus, vision processing is the most important part of the project. If the coordinates generated by the vision-processing unit are incorrect, all other parts of the system result in error, as all other parts of the system depend on the values of the coordinates generated by the vision-processing unit.

Vision processing depends on the image generated by the vision system and the reference images. Both the image and reference image directly depend on the image labels on the UGVs, therefore the image labels on the bots are the key element for the success of the project. This means more work and time are spent coming up with better image labels that can help in generating exact coordinates of the vehicles.

Recommendations

After working extensively with the reference images, the authors came up with some recommendations for making image labels:

1. All of the images should have a square background with different shapes on them.
2. All of the shapes on the images should be as sharp as possible.
3. Both background and shape on a label should be of different colors.
4. Care should be taken to have different colors on the labels for backgrounds and shapes.

References

[1] Bowditch, N. (1995). Dead Reckoning. In *The American Practical Navigator* (pp. 113-118). Bethesda, MD: National Imagery and Mapping Agency. Retrieved from http://www.irbs.com/bowditch/pdf/chapt07.pdf.

[2] Rathbone, R. R. (2000). Beacon-referenced dead reckoning: a versatile guidance system. *Robotics Engineers,* 11-16.

[3] Thamma, R. (2008). Navigational aids to predict the position of automated guided vehicles with ultrasound and radio frequency sensing. *Proceedings of the IAJC-IJME International Conference,* (pp. 154-165).

[4] Thamma, R. (2009, Winter). Estimating Position and Orientation of an Unmanned Guided Vehicle with Ultrasound and Radio Frequency Sensing. *Technology Interface Journal*. Special Edition, 10(2).

[5] Saeedi, P. D. (2006). Vision-Based 3D trajectory tracking for unknown environments. *IEEE Transactions on Robotics, 22*(1), 119-136.

[6] DeSouza, G., & Kak, A. C. (2002, February). Vision for mobile robot navigation: A survey. *IEEE Transactions on Pattern Analysis and Machine Intelligence,* 24(2), 237-267.

[7] Gasteratos, A., Beltran, C., Metta, G., & Giulio, S. (2002). PRONTO: a system for mobile robot navigation via CAD-model guidance. *Microprocessors and Microsystems,* 26, 17-26.

[8] Jens-Steffen Gutmann, M. F. (2008). 3D perception and environment map generation for humanoid robot navigation. *The International Journal of Robotics Research, 27*(10), 1117-1134.

[9] Fiala, M., & Basu, A. (2004). Robot navigation using panoramic tracking. *Pattern Recognition,* 34, 2195-2215.

[10] Huei-Yung, J. H. L. (2006). A Visual Positioning system for vehicle or mobile robot navigation. *IEEE Transactions on Information & Systems, 89*, 2109-2116.

[11] Guerrero, J. J., & Sagues, C. (2001). Uncalibrated vision based on lines for robot navigation. *Mechatronics, 11*, 759-777.

[12] Kundur, S. R., & Raviv, D (2000). Active vision-based schemes for autonomous navigation tasks. *Pattern Recognition,* 33, 295-308.

[13] Wu, C. J., & Tsai, W. H. (2009). Location estimation for indoor autonomous vehicle navigation by omni-directional vision using circular landmarks on ceilings. *Robotics and Autonomous Systems, 57,* 546-555.

Biographies

RAVINDRA THAMMA is with Department of Manufacturing and Construction Management, Central Connecticut State University, New Britain, CT 06053 USA (Tel: 860 -832-3516; fax: 860-832-1806; (e-mail: thammarav@ccsu.edu).

LEELA MOHAN KESIREDDY is a graduate student at Central Connecticut State University, New Britain, CT 06053 USA (Tel: 860-329-2373; (e-mail: kesireddylem@ccsu.edu).

HAOYU WANG is with Department of Manufacturing and Construction Management, Central Connecticut State University, New Britain, CT 06053 USA (Tel: 860-832-1824; fax: 860-832-1806; (e-mail: wanghao@ccsu.edu).

MODELING LEAD VEHICLE DYNAMICS THROUGH TRAFFIC SIMULATION AND FIELD DATA

Fang Clara Fang, University of Hartford; Fei Xue, University of Hartford

Abstract

The majority of existing driver-behavior and car-following data sets, upon which many models are based, are relatively old and focus primarily on the following vehicle instead of the lead vehicle. Therefore, the purpose of this study was to look at how lead vehicle speed varies along basic uniform roadway segments, with grade and with horizontal curvature in the microscopic traffic. The simulation results showed that lead vehicle speed will remain constant under any circumstances, irrespective of slope or grade, or road type. The simulation results may not, however, reflect real lead vehicle dynamics in the real world. The behavior of a lead vehicle at an intersection with a traffic signal was also investigated. When approaching a red light, a linear regression was drawn between lead vehicle deceleration distance and its original speed, i.e., the speed before deceleration. The study showed that at higher roadway speeds, more lead vehicles slowed down to pass the intersection with a green light. Moreover, this study examined how a change in speed for all vehicles in a curve is caused by the change in speed of the lead vehicle. The study, calibrated using field data, was carried out by an Application Programming Interface function in the advanced simulation model, namely AIMSUN. The results showed that if the speed of all of the lead vehicles is influenced by roadway curvature, i.e., there is a reduction in speed, the overall average speed of the traffic network will be affected in the same manner regardless of the volume and speed limit.

Introduction

In traffic engineering, increased computer power has resulted in increasing use of more microscopic traffic simulation models over larger traffic networks. Older models used primarily macroscopic traffic analyses, which involved the aggregate behavior of a traffic stream, characterized by its volume, speed, and density. Recently, microscopic traffic simulation models which track the temporal locations and velocity patterns of individual vehicles in small time steps—that could be as small as 0.10 second in some cases—have been attracting increased attention and receiving increased use. Microscopic simulation models use "car following theory" [1] to capture the changes in an individual vehicle's velocity and, thus, its location in response to the vehicle it is following; a lead vehicle. Recent work [2], [3] has indicated that assumptions regarding car following rules make a difference in emissions estimates and also to the overall aggregate traffic parameters produced by traffic simulation models. The majority of existing driver-behavior and car-following data sets are relatively old and focus primarily on the following vehicle instead of the lead vehicle.

While almost all microscopic traffic simulation models are stochastic based, very little attention has been paid to the lead vehicle dynamics. In other words, the models assume that every vehicle/driver has a relatively constant desired free-flow speed. This desired speed typically varies between simulated vehicles and is often a function of the speed limit on a given link. The percentile of a given driver on the desired speed distribution is assigned stochastically. If the vehicle is not following another vehicle, in other words it is leading, it travels this desired speed. Some models, such as PARAMICS, alter this speed due to horizontal curvature when it is coded into the network but, for the most part, this speed is assumed constant over time with no relationship to its surroundings. In reality, it is obviously reasonable to assume that grade and curvature also affect lead vehicle speed variability. Moreover, transportation planning researchers have illustrated that surrounding land use [4], as well as road and shoulder width, can affect speed.

Since the behavior of lead vehicles is the main input for second-by-second operations of the following vehicle via the car-following theories of microscopic traffic simulation models, studying the lead vehicle dynamics is important. This is especially true since the vehicle dynamics or modes are the new key input variables for emission models. It is essential to get the lead vehicle dynamics to replicate real-world driver behavior to make traffic simulation models useful for modal emission modeling. Some researchers have pointed to the need to collect lead vehicle data [2], but to date none have been collected. Most car-following tests that have been carried out in an effort to advance car-following models were conducted on test-track facilities and in vehicular tunnels [5]. In these tests, lead vehicle speed usually followed a predetermined speed pattern, including constant, random, or sinusoidal patterns [6-8]. Therefore, there is not a complete understanding of how lead vehicle speed varies with grade, with horizontal curvature, or as vehicles accelerate or decelerate within the network along basic uniform

roadway segments.. In addition, it is unknown whether the behavior of all drivers is relatively the same, or if variation from person to person is large enough that a certain number of distinct driver categories must be established for modeling purposes.

The critical second-by-second vehicle operations in a simulation model are dictated by microscopic flow theory or so-called car-following models. The majority of existing driver-behavior and car-following data sets, upon which these models are based, are relatively old and focus primarily on the following vehicle instead of the lead vehicle. In addition, simulation models typically assume that lead vehicles travel at a relatively constant desired speed with minor, random acceleration or deceleration changes. The limited study of lead vehicles is surprising because the behavior of lead vehicles is the most fundamental input to the microscopic car-following theories and, therefore, affects accuracy. As such, it is necessary to understand the lead vehicle dynamics over different roadway and traffic conditions and to use this information to replicate real-world driver behavior. Furthermore, the lead vehicle typology developed in this current study will be essential for establishing the type and size of driver samples needed for future real-world driving data collection.

Objectives

If a vehicle is not following another vehicle, it can be seen as a lead vehicle. A lead vehicle should travel at its desired speed, the maximum allowable speed. In reality, it seems reasonable to assume that the desired speed might not be fixed but in fact vary with each basic roadway segment, grade, and horizontal curve. To test such an assumption, microscopic traffic simulation models that are based on 'car -following theory' appear easy to employ due to their conceptual similarities with the assumption.

The purpose of this study, then, was to evaluate how lead vehicle speed varies along basic uniform roadway segments, with grade and with horizontal curvature in the microscopic traffic simulation environment, using AIMSUN. The next section presents the experimental method of capturing lead vehicle information, and the three subsequent sections focus on testing the three hypotheses, which are:

Hypothesis 1: Lead vehicle velocity is influenced by horizontal curvature over all kinds of roadway types.
Hypothesis 2: Lead vehicle velocity is influenced by grade over all kinds of roadway types.
Hypothesis 3: Lead vehicle deceleration rate is influenced at intersections with signals for both green and red lights.

In addition, the study investigated how the change in speed at a curve for all vehicles is caused by the change in the speed of the lead vehicle using field data.

Detect Lead Vehicles in Simulation

Lead vehicle means the vehicle is unconstrained by a vehicle in front of it. In this simulation study, a lead vehicle was defined as one where no other vehicle has passed the current position in the same lane within the past 5 seconds. This definition is consistent with the one used in the field data collection process, where constrained driving was considered when the driver was following another vehicle with less than a five-second headway or the brake lights illuminated on a vehicle ahead of the instrumented vehicle [8]. Additionally the five-second time interval/headway is equivalent to a 330ft headway on an urban road with an average speed 45 mph, or 513 feet on a freeway with an average speed of 70 mph.

Lead Vehicle Dynamics on Horizontal Curves

Lead vehicle dynamics on horizontal curves were studied using AIMSUN as the simulation tool. As shown in Figure 1, a study area in the city of Hartford, CT, was selected including a segment of I-91 with both on and off ramps, several urban streets with eight signalized intersections, one stop sign, and one yield control. The traffic was comprised of cars, trucks, and buses.

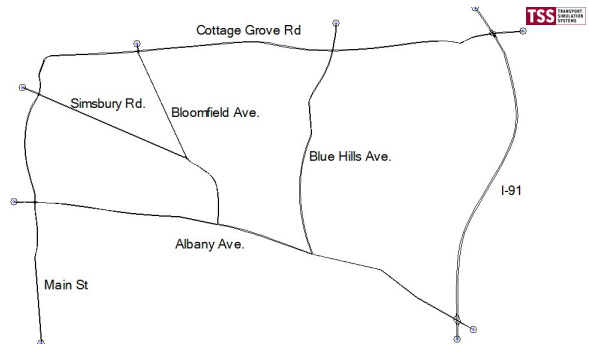

Figure 1. Traffic Network of the Study Area

Figures 2 and 3 detail the placement of detectors on two horizontal curves on an urban street—Cottage Grove Road (Figure 2); and the I-91 freeway (Figure 3), in order to determine whether or not the horizontal curvature affects the velocity of a lead vehicle. One detector was set before the curve and the other within the curve. The speed of the lead vehicle was measured and compared by these two detectors as it passed them.

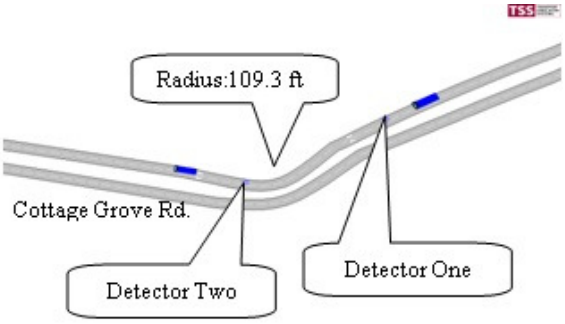

Figure 2. Lead Vehicle Velocities with Urban Street Horizontal Curves

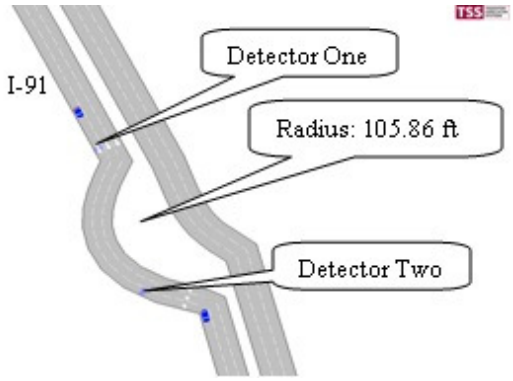

Figure 3. Lead Vehicle Velocities with Freeway Horizontal Curves

The simulation was run for 20 minutes. In total there were 75 lead vehicles going through the curve on the urban street, all of which showed no change in velocity (less than 1 mile per hour). Similarity, the 164 lead vehicles detected on the freeway segment also exhibited no change in velocity. The study showed that lead vehicle speeds will stay constant on a curved road on any type of roadway in the simulation environment, AIMSUN.

Lead Vehicle Dynamics on Roadway Grades

Lead vehicle behavior affected by grade was examined using AIMSUN. As shown in Figures 4 and 5, a segment on Blue Hill Avenue (Figure 4), an urban street with an 8.02 percent grade, and a segment on I-91 (Figure 5), a freeway with a -8.52 percent grade, were chosen. Two detectors were placed in each segment: one in advance of the grade and the other on the peak of the grade. The simulations were run for 20 minutes. Based on the data recorded by the detectors, including the number of vehicles and their speeds, sixty-six lead vehicles were captured going past the Blue Hill Avenue detector and eighty-seven lead vehicles were recorded on the freeway. None showed any change in speed. The results of the simulation using AIMSUN showed that neither lead vehicle behavior nor speed was affected by grade.

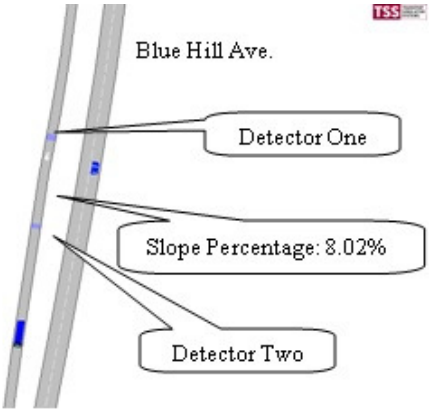

Figure 4. Lead Vehicle Velocities with Urban Street Slopes

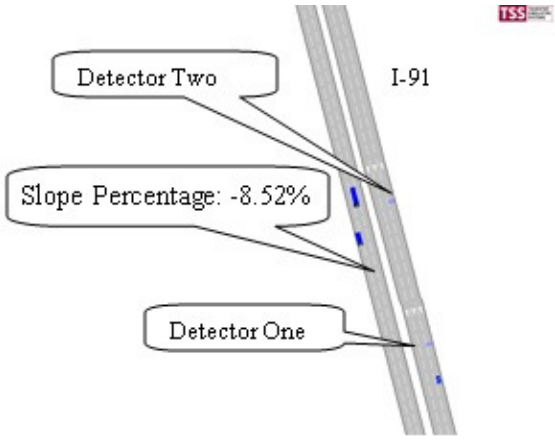

Figure 5. Lead Vehicle Velocities with Freeway Slopes

Lead Vehicle Dynamics at Intersections

In this section, the behavior of a lead vehicle at an intersection with a traffic light was investigated. Two scenarios were considered: one was to study how a lead vehicle responds to a red light, while the other was how it reacts to a green light when approaching the intersection.

Approaching a Red Light

It was found that all vehicles would reduce their speed when approaching a red light. Without the interference of other vehicles ahead, the extent to which a lead vehicle re-

sponds to this scenario is simply a function of its perception of and reaction to the red stop signal. This experiment studied the deceleration distance of a lead vehicle since it was easier to measure and more intuitive to understand. The deceleration distance measures the distance that a lead vehicle travels from its current speed to a dead stop with a constant rate of deceleration. The intersection at Main Street and Albany Avenue was studied, as illustrated in Figure 6. The approach roads were selected so that road design elements such as grade and curvature would not affect the vehicles' change in speed.

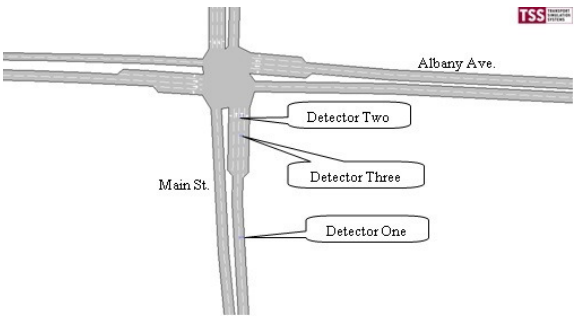

Figure 6. Lead Vehicle Deceleration Distance with Traffic Signal

Detector One (Figure 6) was placed 305.9 feet away from the stop line of the intersection. A vehicle was determined to be leading if no other vehicle passed the detector within 5 seconds of that vehicle. For a lead vehicle approaching a red traffic signal, its speed was tracked and measured at every simulation step as it traveled to the stop line. Once the lead vehicle started to decelerate, the distance to the stop line was determined to be the deceleration distance.

In order to study the relationship between vehicle speed and deceleration distance, three speed ranges were examined: 20~30 mph, 30~40 mph, and 40~50 mph. A simulation of 20 minutes was used for each scenario. A total of 129 lead vehicles approaching a red light were evaluated and their corresponding deceleration distances were measured. Figure 7 shows the relationship between lead vehicle speed before deceleration (mph) and the deceleration distance (feet).

A linear regression was performed on the experimental data and the following equation was derived:

$$y = 5.547x - 41.712 + \varepsilon$$

where

y = Lead vehicle deceleration distance while approaching the red light (feet)

x = Lead vehicle speed before deceleration while approaching the red light (mph)

ε = A normal distribution with a mean of 0 and a standard deviation of 38.68 feet

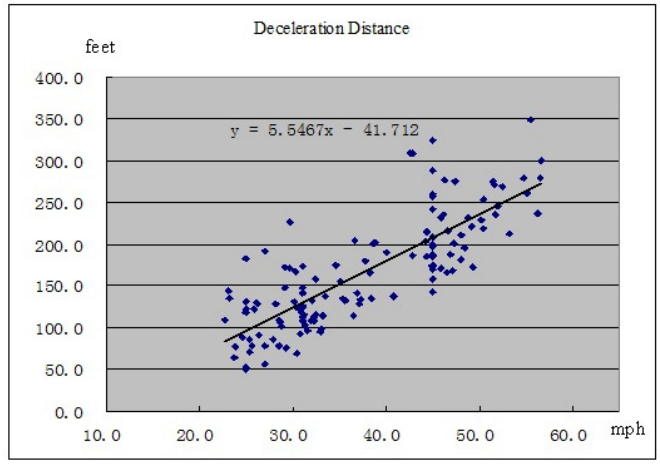

Figure 7. Lead Vehicle Speed before Deceleration vs. Deceleration Distance

The R value in this regression model was 0.809. Moreover, both the ANOVA and T-test showed that the P-value of the coefficient of the slope was 4.15×10^{-31}, which means that there was a strong linear relationship between the lead vehicle deceleration distance and its speed before deceleration. In addition, the domain of this model was that x was between 10 and 60 mph, as this was on an urban road.

Approaching a Green Light

How a lead vehicle changes its speed when approaching a green light at an intersection is discussed in this section. The hypothesis was that 'aggressive' lead drivers would speed up at a green light, while 'safe' lead vehicle drivers would slow down. At the intersection of Main Street and Albany Avenue, two more detectors were added on the intersection approach: Detector Two and Detector Three, as shown in Figure 6. Detector One was still used to test whether or not a vehicle was a lead vehicle, based on the 5-second rule. Once the detector captured a lead vehicle while the traffic light was green, then the vehicle would be tracked as such. When the tracked lead vehicle passed through Detector Two with the same green light, its speed was compared with that from Detector One. If a reduction or increase in speed of 2 mph or more occurred, the speed change was noted.

This study excluded the following two scenarios:

1) The traffic light switched to red while the lead vehicle was passing through Detector Two.

2) If there was a significant number of queued vehicles ahead of the lead vehicle that prevented it from traveling freely through the intersection. The scenarios could be easily detected with Detector Three, which was placed close to the stop line in order to measure any queued vehicles.

A series of vehicle original speeds (speed before slowing down or speeding up) were examined and are presented in Table 1. It was found that no lead vehicle changed its speed passing the junction with an original speed of less than 30 mph. The higher the original speed, the higher the percentage of vehicles that slowed down. When the original speed reached 45 mph, all of the lead vehicles slowed down at the intersection. It is worth pointing out that at speeds above 50 mph, one vehicle sped up while the rest slowed down.

Table 1 Variation of Lead Vehicle Speed at Green Light Intersection

Original Speed	Number of vehicles speed unchanged	Number of vehicles speed decreased	Number of vehicles speed increased
0~30 mph	13	0	0
30~35 mph	18	2	0
35~40 mph	12	5	0
40~45 mph	4	12	0
45~50 mph	0	15	0
50mph and above	0	13	1

Figure 8 illustrates how the speed decreased compared with various approaching speeds. The x axis in the figure shows the speed before slowing down, while the y axis is the speed reduction when the vehicle went through the intersection with a green light.

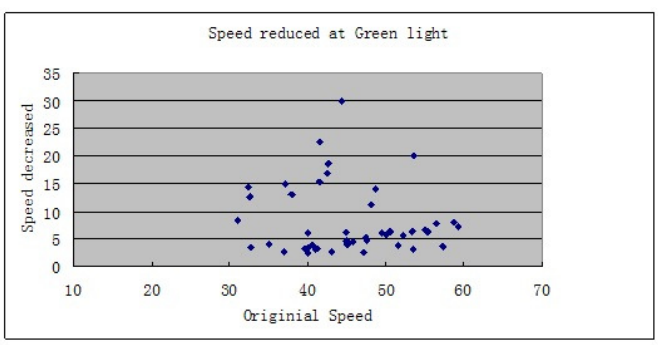

Figure 8. Speed Reduction at Green Light versus Vehicle Approaching Speed

The ANOVA analysis showed that the data were randomly distributed and there was no obvious linear or other relationship discovered between these two factors.

Simulation using Field Data

Change of Lead Vehicle Speeds in the Simulation by Application of a Programming Interface (API)

The simulation study showed that lead vehicle speeds are NOT affected either by horizontal curvature or grades on various types of roadways (with different posted speed limits). The field study suggested that there were statistically significant differences in speed and acceleration patterns for older and younger lead drivers [8].

This section reviews how the speed at a curve for all vehicles, caused by the change in the lead vehicles' speed, changed. A segment on the study route used in the Belz and Aultman project [8] was selected. As shown in Figure 9, the radius of the curve was 175.35 feet. The total length of the curved road was then set to be 601.56 feet. The speed limit of the road was 40 mph, one lane per direction. The study period was 9:00am to 9:20am. The traffic composition was 90% cars and 10% trucks. As shown in Figure 9, two detectors were planned, one at the beginning and the other at the end of the curve.

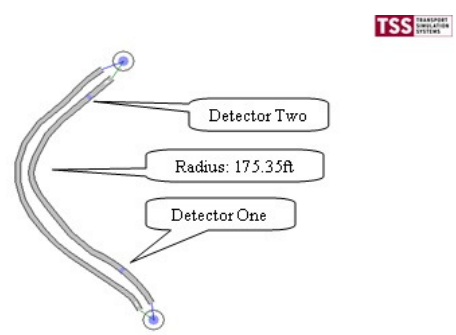

Figure 9. Study Scenario

Since the simulation software, similar to AIMSUN, does not automatically change the speed of a vehicle when it negotiates a curve, the study applied an Application Programming Interface (API) to manually change the speed of all lead vehicles. The flowchart of Figure 10 describes how the API was applied in order to achieve this purpose.

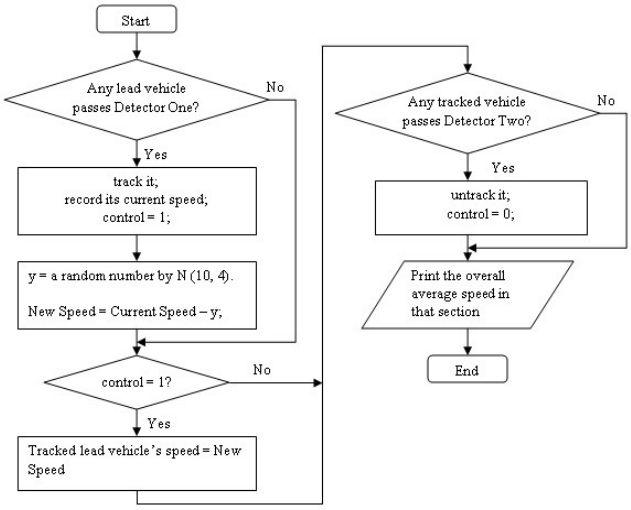

Figure 10. Flowchart of API to Manually Control the Speed of Lead Vehicle

An API is available as an advanced feature in some simulators such as AIMSUN to provide an interface connection between user-defined applications and the simulation environment. The flowchart of Figure 10 was repeated in every simulation step. It showed that once Detector One captured a lead vehicle, it would be tracked and its speed reduced. The reduction is stochastically assigned following a Normal Distribution with a mean of 10 mph and a standard deviation of 4. The vehicle traveled at this reduced speed within the curve. After it passed the curve and Detector Two, the vehicle would be released from its "tracking" status and allowed to resume a speed automatically assigned by the simulation software based on its characteristics and the speed limit of the roadway.

Impact of Lead Vehicle Speed Change to the Overall Network given a Speed Limit of 40 mph

Table 2 presents the average speed of all vehicles passing that section during a 20-minute period where the roadway speed limit was 40 mph. Two scenarios were considered: one without API control to represent that there would be no change in lead vehicle speed, and one with API control to show where all lead vehicles are forced to slow down according to the distribution explained in Figure 10. The overall average speed of all vehicles in that section without API control and with API control under different traffic volumes were compared and summarized in Table 2. Here, API only controls the speed of the lead vehicles.

Table 2. Overall Average Speed affected by Lead Vehicle Speed Changes

Volume Vehicles per hour	Overall Average Speed without API	Overall Average Speed with API	Difference
200	43.56	36.25	7.31
600	42.57	37.68	4.89
1000	41.70	37.26	4.44
1400	40.31	36.77	3.54
1800	38.09	36.03	2.06

(Roadway: Speed limit = 40 mph)

The results shown in Table 2 clearly indicate that the overall average network speed decreased when the network traffic got heavier, if there was no change on lead vehicle speed (i.e., without API control in the simulation). However, the situation was quite different for the case where the lead vehicles did change their speed in order to negotiate the curve (i.e., with API control in this experiment). The simulation showed that the overall speed fluctuated between 36 and 37 mph. Since the speed of the lead vehicles was reduced by a random value with a standard deviation of 4 mph, compared to the speed standard deviation of 0.58 mph in Table 2, it was believed that traffic volume was independent of overall average speed. The finding suggests that if the speed of all lead vehicles is affected by the curvature, i.e., resulted in a reduction in their speed, all of the vehicles in the entire network would be affected in the same manner, regardless of the volume.

Impact of Lead Vehicle Speed Change to Overall Network for Various Speed Limits

This section presents the results of whether or not the roadway speed limit affected the results. Table 3 shows the results for a local road of 25 mph and a freeway of 60 mph. Both cases showed consistent results with the speed limit of 40 mph. The overall average speeds decreased while the traffic volume increased. However, with a drop of lead vehicle speed, there seemed to be little impact on the overall network speed by the change of volume.

As shown in Tables 2 and 3, the differences in average speed (the last column) were approximately the same in terms of a variety of traffic demands. It means that API reduced almost the same amount of speed from its original speed under different speed limits. Hence, the reduction of network speed by API is independent of the speed limit.

Table 3. Overall Average Speed affected by Lead Vehicle Speed Changes

Speed limit mph	Volume Vehicles per hour	Overall Average Speed without API	Overall Average Speed with API	Difference
60	200	62.49	55.96	6.53
	600	61.21	55.52	5.69
	1000	59.84	55.38	4.46
	1400	58.46	55.90	2.56
	1800	55.95	54.43	1.52
25	200	27.14	19.83	7.31
	600	26.19	20.72	5.47
	1000	25.33	19.87	5.46
	1400	24.55	19.96	4.59
	1800	23.06	20.42	2.64

(Roadway: Speed limit = 60 mph and 25 mph)

Impact of Each Vehicle Speed Change to the Overall Network

An interesting experiment was conducted to study how the network would behave if each vehicle would respond to the curvature by reducing its speed following a statistical distribution, explained in Figure 10. Table 4 presents the comparison of two cases for a roadway of 40 mph: one with speed control of each vehicle, and one with speed control of the lead vehicle only.

Table 4 A Comparison of Overall Average Speed

Volume Vehicles per hour	Overall average speed with control of each vehicle	Overall average speed with control of lead vehicles
200	33.95	36.25
600	10.40	37.68
1000	6.87	37.26
1400	3.60	36.77
1800	3.54	36.03

(Roadway: Speed limit = 40 mph)

It was surprising to discover that the overall average speed with a control of each vehicle's speed decreased very quickly with an increase of traffic volume. The reason is that with an application of normal distribution, the speed reduction of each vehicle is randomly assigned (so that some vehicles slow down much more than others do). As a result, a vehicle with a current speed of 40 mph might be forcefully slowed down to 15 mph, which would create a bottle-network or slow-moving queue scenario in the traffic and, therefore, have a more profound impact on the entire network.

Conclusion

The simulation results showed that lead vehicle speed will remain constant in any circumstances, whether with slope or grade changes and on all selected road types. With real-life experience, it is reasonable to assume that lead vehicle speed and acceleration are affected by the curvature and grade of the road. These hypotheses were also validated by field studies [9], [10]. Hence, the results generated by the microscopic traffic simulation model do not match the proposed hypotheses. It is believed that the simulation does not reflect lead vehicle dynamics in the real environment. Some detailed findings and justifications about the simulation study are provided below:

First, in AIMSUN, when a car is travelling on a horizontal surface, its speed will be affected by three factors: maximum desired speed of the vehicle, speed acceptance of the vehicle, and speed limit of the section or turn. The maximum desired speed is a maximum value between a speed generated by the characteristics of the driver and a speed imposed by the presence of a vehicle in front of it, neither of which take into account road geometric information. Speed acceptance of a vehicle is part of a driver's characteristics which still do not include effects of the geometry of the section. The only geometric information of the sections is the speed limit of the section that is unfortunately a fixed value, so it becomes very easy to understand why the vehicle speed will not be affected by any horizontal curvature of the section.

Secondly, in AIMSUN, when a vehicle is travelling on a section with a slope, the slope percentage will only change its maximum acceleration. The calculation of the vehicle velocity uses the same calculation for when the vehicle is on a horizontal surface. Therefore, the slope percentages will not change the vehicle speed. In other words, AIMSUN is just a program that applies the microscopic traffic simulation in a mathematical way, and cannot replace field tests.

Moreover, the behavior of a lead vehicle at intersections with traffic signals was investigated. When approaching a red light, a linear regression was drawn between lead vehicle deceleration distance and the vehicle's original speed; i.e., the speed deceleration before deceleration. However, the data also showed a more random distribution when ap-

proaching a green light. The study showed that the higher the roadway speed, the higher the percentage of lead vehicles that slowed down. More lead vehicles would reduce their speed when they travel on the higher speed roadways when approaching an intersection with a green light.

Finally, how the change in speed at a curve for all vehicles caused by the change in speed of the lead vehicles was studied using field data. An API was developed to manually carry out this plan in the simulation. The findings show that if the speed of all of the lead vehicles is affected by curvature, i.e., resulted in a reduction in speed, all of the vehicles in the entire network would be affected in the same manner regardless of the volume and speed limit.

It is suggested that a more realistic speed distribution of lead vehicles responding to the external environment, e.g., curvature or grade, should be used in the simulation. Data collection on various driver populations with different behavior or age groups is absolutely necessary to enhance the accuracy of the simulation.

Acknowledgement

The authors would like to acknowledge Dr. Lisa Aultman -Hall and Nathan Belz at the University of Vermont, and the New England University Transportation Center (NEUTC) for their support on this project.

Reference:

[1] Brackstone, M., & McDonald, M. (1999). Car-following: a historical review. *Transportation Research,* Part F., 2, 181-196.

[2] Rakha, H., Snare, M., & Dion, F. (2004). Vehicle Dynamics Model for Estimating Maximum Light Duty Vehicle Acceleration. *Transportation Research Record.* 1883, 40-49.

[3] Rakha, H., & Crowther, B. (2003). Comparison and Calibration of FRESIM and INTEGRATION Steady-state Car-following Behavior, *Transportation Research*, 37A, 1-27.

[4] Kloeden, C., McLean, A., Moore, V., & Ponte, G. (2005). Traveling Speed and the Risk of Crash Involvement. University of Adelaide. NHMRC Road Accident Research Unit. Retrieved July 15 from http://casr.adelaide.edu.au/speed.

[5] Rothery, R. (1992). *Chapter 4: Car Following Model, Traffic Flow Theory*, A state-of-the-Report, revised Monograph, Transportation Research Board (TRB) Special Report 165.

[6] Todosiev, E. P. (1963). *The Action Point Model of the Driver Vehicle System,* Report No. 202A-3, Ohio State University, Engineering Experiment Station, Columbus, Ohio.

[7] Ranjitkar, P., Nakatsuji, T., Azuta, Y., & Gurusinghe, G. (2003). Stability Analysis Based On Instantaneous Driving Behavior Using Car-Following Data, *Transportation Research Record.* 1852, 140-151.

[8] Ohlhauser, A. D., Milloy, S., & Caird, J. K. (2011). Driver Responses to Motorcycle and Lead Vehicle Braking Events: The effects of motorcycling experience and novice versus experienced drivers. *Transportation Research Part F: Traffic Psychology and Behavio.* 14(6), 472-483

[9] Belz, N., & Aultman-Hall, L. (2010). Analyzing the effect of Driver Age on Operating Speed and Acceleration Noise using On-board Second-by-Second Driving Data. *Proceedings of 90th Transportation Research Board (TRB) Annual Meeting, January 2011.*

[10] Jackson, E., & Aultman-Hall, L. (2010). Analysis of Real-World Lead Vehicle Operation for Modal Emissions and Traffic Simulation Models. *Transportation Research Record: Journal of the Transportation Research Boar*. pp 44-53

Biographies

FANG CLARA FANG is an Associate Professor of Civil Engineering at the University of Hartford. Fang holds a Ph.D. degree in transportation engineering from Pennsylvania State University, two Master degrees in civil engineering from the University of British Columbia, Canada and the City University of Hong Kong, respectively, and a Bachelor degree in civil engineering from Sichuan University, China. Dr. Fang's research interests include transportation system modelling and simulation, traffic operations, signal control, optimization and computational intelligence applications in transportation. Dr. Fang may be reached by phone at (860)768-4845 or by email at fang@hartford.edu.

FEI XUE is an Assistant Professor of mathematics at University of Hartford. He earned his B.S. degree (Applied Mathematics, 2001) from South China University of Technology, and Ph.D. (Mathematics, 2006) from the West Virginia University. Dr. Xue is currently teaching at the University of Hartford. His interests are in asymptotic analysis of differential and difference systems, time scales, and application of mathematics. Dr. Xue may be reached at Department of Mathematics, University of Hartford, West Hartford, CT 06117; Phone (860)768-5916; Fax: (860)768-5244; Email xue@hartford.edu.

INSTRUCTIONS FOR AUTHORS: MANUSCRIPT REQUIREMENTS

The INTERNATIONAL JOURNAL OF MODERN ENGINEERING is an online/print publication, designed for Engineering, Engineering Technology, and Industrial Technology professionals. All submissions to this journal, submission of manuscripts, peer-reviews of submitted documents, requested editing changes, notification of acceptance or rejection, and final publication of accepted manuscripts will be handled electronically. The only exception is the submission of separate high-quality image files that are too large to send electronically.

All manuscript submissions must be prepared in Microsoft Word (.doc or .docx) and contain all figures, images and/or pictures embedded where you want them and appropriately captioned. Also, for all accepted manuscripts, each figure, image or picture that was imported into your Word document must be saved individually as a **300dpi or higher JPEG (.jpg)** file and submitted separately; your manuscript and figure numbers must be used in the title of the file (e.g., **M12-S-18 Figure 4**); that means one additional file for each image imported into your manuscript. These 300dpi images do NOT need to be embedded in your manuscript. For tables or graphs created directly in Word, you do not need to submit them as separate files.

Included below is a summary of the formatting instructions. You should, however, review the sample Word document of our website for details on how to correctly format your manuscript. The editorial staff reserves the right to edit and reformat any submitted document in order to meet publication standards of the journal.

The references included in the References section of your manuscript must follow APA-formatting guidelines. In order to help you, the sample Word document also includes numerous examples of how to format a variety of scenarios. Keep in mind that an incorrectly formatted manuscript will be returned to you, a delay that may cause it (if accepted) to be moved to a subsequent issue of the journal.

1. **Word Document Page Setup**: Two columns with ¼" spacing between columns; Top of page = ¾"; Bottom of page = 1" (from the top of the footer to bottom of page); Left margin = ¾"; Right margin = ¾".

2. **Paper Title**: Centered at the top of the first page with a 22-point Times New Roman (Bold), Small-Caps font.

3. **Page Breaks**: Do not use page breaks.

4. **Body Fonts**: Use 10-point Times New Roman (TNR) for body text throughout (1/8" paragraph indention); 9-point TNR for author names/affiliations under the paper title; 16-point TNR for major section titles; 14-point TNR for minor section titles; 9-point TNR BOLD for caption titles for tables and figures; other font sizes as noted in the sample document.

5. **In-text Referencing**: List and number each reference when referring to them in the body of your document (e.g., [1]). The first entry must be [1] followed by [2], [3], etc., continuing in numerical order to the final entry in your References section. Again, see the sample Word document for specifics. Do not use the End-Page Reference utility in Microsoft Word. You must manually place references in the body of the text.

6. **Tables and Figures**: Center all tables and figures. Captions for tables must be above the table, while captions for figures are below; all captions are left-justified.

7. **Page Limit**: Manuscripts should not be more than 15 pages (single-spaced, 2-column format).

8. **Page Numbering**: Do not use page numbers.

9. **Publication Charges:** Manuscripts accepted for publication are subject to mandatory publication charges.

10. **Copyright Agreement:** Review the **copyright transfer agreement**.

11. **Submissions:** All manuscripts and associated files must be submitted electronically; the only exception would be if you wish to submit a CD with the individual files for your high-quality images, as noted above.

    MANUSCRIPTS should be submitted to Dr. Philip D. Weinsier, manuscript editor, at philipw@bgsu.edu along with a copy to editor@ijme.us.

    FILES containing your high-quality images should ONLY be submitted to philipw@bgsu.edu.

THE LEADING INTERNATIONAL JOURNAL OF ENGINEERING TECHNOLOGY

www.tiij.org

www.iajc.org

THE TECHNOLOGY INTERFACE INTERNATIONAL JOURNAL

ABOUT TIIJ:

- TIIJ is an official journal of the International Association of Journal and Conferences (IAJC).
- TIIJ is a high-quality, independent journal steered by a distinguished board of directors and supported by an international review board representing many well-known universities, colleges, and corporations in the U.S. and abroad.
- TIIJ generally publishes research related to applied mathematics, science, and engineering technology.

OTHER IJAC JOURNALS:

- The International Journal of Modern Engineering (IJME)
  For more information visit www.ijme.us
- The International Journal of Engineering Research and Innovation (IJERI)
  For more information visit www.ijeri.org

TIIJ SUBMISSIONS:

- Manuscripts should be sent electronically to the manuscript editor, Dr. Philip Weinsier, at philipw@bgsu.edu.

  For submission guidelines visit www.tiij.org/submission.htm

TO JOIN THE REVIEW BOARD:

- Contact the chair of the International Review Board, Dr. Philip Weinsier, at philipw@bgsu.edu.

  For more information visit www.tiij.org/editorial.htm

INDEXING ORGANIZATIONS:

- TIIJ is now indexed by EBSCO, one of the world's largest and most prestigious indexing organizations. The journal is also under review by Thomson Reuters ISI and DOAJ.

Contact us:

Philip D. Weinsier, Ed.D.

Editor-in-Chief
Bowling Green State University-Firelands
One University Drive
Huron, OH 44839
Office: (419) 372-0628
Email: philipw@bgsu.edu

www.ijme.us

www.ijeri.org

IJME NOW SEEKS SPONSORS

IJME IS THE OFFICAL AND FLAGSHIP JOURNAL OF THE INTERNATIONAL ASSOCATION OF JOURNALS AND CONFERENCE (IAJC)

www.iajc.org

The International Journal of Modern Engineering (IJME) is a highly-selective, peer-reviewed journal covering topics that appeal to a broad readership of various branches of engineering and related technologies. IJME is steered by the IAJC distinguished board of directors and is supported by an international review board consisting of prominent individuals representing many well-known universities, colleges, and corporations in the United States and abroad.

IJME Contact Information

General questions or inquiries about sponsorship of the journal should be directed to:

Mark Rajai, Ph.D.
Editor-in-Chief
Office: (818) 677-2167
Email: editor@ijme.us
Department of Manufacturing Systems Engineering & Management
California State University-Northridge
18111 Nordhoff St.
Northridge, CA 91330